



THESIS WORK FOR DUAL MASTER'S DEGREE

KIT M.Sc. in Mechanical Engineering

ITBA Mag. in Energy and Environment

Design of a MoNiKa-Turbine and Condenser Model in
Modelica/Dymola and Comparison with previous Simulink
Models and Experimental Results

Mirco Maier

Mechanical Engineering - KIT

Tutor

Hans-Joachim Wiemer (KIT/ITES)

Co-Tutor

Dr. Ing. Sebastián D'Hers (ITBA)

Examiners

Prof. Dr.-Ing. Robert Stieglitz (KIT/ INR)

Bunos Aires
06/03/2023

Design of a MoNiKa-Turbine and Condenser Model in Modelica/Dymola and Comparison with previous Simulink Models and Experimental Results

Dual Master in Mechanical Engineering - Energy and Environment

Master Thesis of

Mirco Maier

At the Department of Mechanical Engineering,
Institute for Applied Thermofluidics - IATF

Advisors: Prof. Dr.-Ing. Robert Stieglitz
Hans-Joachim Wiemer
Dr. Ing. Sebastián D'Hers
Dr. rer. nat. Ferdinand Schmidt

Duration: September 2022 – March 2023

I truthfully affirm to have written the thesis independently, to have indicated all used aids completely and accurately, and to have marked everything taken from the works of others unchanged or with modifications, as well as to have observed the KIT Statutes for Safeguarding Good Scientific Practice in the currently valid version.

Ich versichere wahrheitsgemäß, die Arbeit selbstständig verfasst, alle benutzten Hilfsmittel vollständig und genau angegeben und alles kenntlich gemacht zu haben, was aus Arbeiten anderer unverändert oder mit Abänderungen entnommen wurde sowie die Satzung des KIT zur Sicherung guter wissenschaftlicher Praxis in der jeweils gültigen Fassung beachtet zu haben.

Buenos Aires, 06.03.2023

Mirco Maier

Abstract

To research optimization possibilities in supercritical ORC processes for geothermal power production the *Modular low-Temperature Circuit Karlsruhe* (MoNiKa) was built at Campus North of the Karlsruhe Institute of Technology. Several research tasks have been conducted over this installation focusing on individual components. The present master thesis describes the development of a coupled MoNiKa turbine-condenser model using the *Modelica* modeling language with the *Dymola* development environment. For thermodynamic components the commercial library *TIL* was used. To calculate the properties of the working fluid a *Dymola-REFPROP* interface was utilized.

For the turbine model an empirical efficiency correlation of the MoNiKa turbine was developed from experimental data and implemented. The determination of the turbine inlet pressure is based on Stodola's cone law which has been adjusted to the MoNiKa turbine in previous studies [28]. To reduce computational time the input data has been pre-processed by applying filters. For the condenser model grid convergence studies were carried out to ensure precision and convergence.

The simulation results of the developed models were compared to the results of previous Simulink models for turbine [9] and condenser [11]. The model was then validated using experimental data from several MoNiKa test runs from 08-10 November 2021 representing a range of different operating conditions. The quantitative and qualitative agreement of the simulated turbine shaft power with the experimental data could be improved compared to the previous models.

The developed coupled turbine-condenser model is capable of providing close approximations of turbine shaft power and condenser outlet variables over a wide operating range of the MoNiKa plant. In addition, the computation time could be kept within reasonable limits to enable further extensions of the model to complete the MoNiKa cycle. The influence of individual input parameters on the output variables could be determined by means of a sensitivity study to guide further improvements in the measuring equipment.

Contents

Symbols and Abbreviations	vii
List of Figures	ix
List of Figures	xi
1. Introduction	1
1.1. Motivation	1
1.2. Objective and Approach	2
2. Basic Principles	3
2.1. Geothermal Energy	3
2.2. Organic Rankine Cycle	4
2.3. MoNiKa	6
2.3.1. Instrumentation	7
2.3.2. MoNiKa Turbine	9
2.3.2.1. Energy Balance of Turbine	9
2.3.2.2. Isentropic Efficiency of Turbine	10
2.3.2.3. Stodola’s Cone Law	10
2.3.3. MoNiKa Condenser	11
2.4. Heat Transfer	12
2.4.1. Tube-side Heat Transfer	13
2.4.2. Heat Conduction in Tube Wall	15
2.4.3. Air-side Heat Transfer	16
2.5. Pressure Loss	18
2.5.1. Pressure Loss in Tubes	18
2.5.2. Pressure Loss for Condensation	19
2.5.3. Air-side Pressure Loss	20
2.6. Dynamic Simulation	20
2.6.1. Modelica, Dymola	20
2.6.2. TIL	21
2.6.2.1. General Principles of TIL	22
2.6.2.2. Balance Equations in TIL	23
2.6.2.3. Turbine Model in TIL	24
2.6.2.4. Condenser Model in TIL	25
2.6.2.5. Exemplary Model with Components from TIL	25
2.6.3. REFPROP	27
3. Model Development	29
3.1. Introduction of the Experimental Data from Test Runs	29
3.1.1. Calculation of Inlet Enthalpy for Turbine and Condenser	30
3.2. Methods for the Quantification of the Agreement of Results	33

3.3.	Development of the Turbine Model	34
3.3.1.	Implementation of the Turbine Model and Comparison with the Simulink Turbine Model by Julia Filipe	34
3.3.2.	Development of a new Correlation for the Turbine Efficiency	37
3.4.	Development of the Condenser Model	40
3.4.1.	Grid Sensitivity Study	40
3.4.2.	Methods to Reduce Computation Time	43
3.4.2.1.	Resampling of Measurement Data	43
3.4.2.2.	Influence of Pressure Drop Model on the Outlet Enthalpy	46
3.4.3.	Comparison with the Simulink Condenser Model by Mariano Fossati and Introduction of a Correction Factor	48
3.5.	Development of the Coupled Turbine-Condenser Model	52
4.	Verification and Validation of the Models using Experimental Data	55
4.1.	Verification and Validation of the Turbine Model	55
4.1.1.	Verification of the Turbine Model with Data from Day1	55
4.1.2.	Validation of the Turbine Model with Data from Day2 and Day3	58
4.2.	Verification and Validation of the Condenser Model	61
4.3.	Validation of the Coupled Model	68
4.4.	Sensitivity Study	73
5.	Summary and Conclusion	77
	Bibliography	81
	Appendix	87
A.	Additional Information for the Condenser Model	87
B.	Matlab Codes	87
B.1.	Matlab Function for the Quantification of the Agreement of Results	87
B.2.	Matlab Codes for Filtering and Resampling of Measurement Data	89
B.3.	Matlab Function for Filtering of Turbine Shaft Power	94

Symbols and Abbreviations

Latin Symbols

SYMBOL	UNIT	MEANING
A	[m ²]	Area
c	[$\frac{m}{s}$]	Velocity
c_p	[$\frac{J}{kg \cdot K}$]	Specific Heat Capacity at constant Pressure
d	[m]	Diameter
E	[J]	Energy
g	[$\frac{m}{s^2}$]	Gravitational Acceleration
h	[$\frac{kJ}{kg}$]	Specific Enthalpy
k	[$\frac{W}{m^2 \cdot K}$]	Heat Transfer Coefficient
l	[m]	Length
L	[m]	Length
m	[kg]	Mass
n	[$\frac{1}{s}$]	Rotational Speed
p	[Pa]	Pressure
P	[W]	Power
Q	[J]	Heat
R	[$\frac{K}{W}$]	Thermal Resistance
s	[$\frac{kJ}{kg \cdot K}$]	Specific Entropy
T	[K]	Temperature
t	[s]	Time
V	[m ³]	Volume
W	[J]	Work
w	[$\frac{m}{s}$]	Velocity
x	[]	Steam / Vapor Quality
z	[m]	Height

Greek Symbols

SYMBOL	UNIT	MEANING
ρ	[$\frac{kg}{m^3}$]	Density
φ	[%]	Relative Humidity
η	[]	Efficiency
α	[$\frac{W}{m^2 \cdot K}$]	Heat Transfer Coefficient
λ	[$\frac{W}{K}$]	Thermal Conductivity
ν	[$\frac{m^2}{s}$]	Kinematic Viscosity
μ	[$\frac{kg}{m \cdot s}$]	Dynamic Viscosity
Ψ	[]	Void Ratio
ξ	[]	Pressure Loss Coefficient

δ	[%]	Variation
ε	□	Deviation

Abbreviations

ABBREVIATION	MEANING
Amb	Ambient
BPV	Bypass Valve
CV	Control Valve
Dymola	Dynamic Modeling Laboratory
GWP	Global Warming Potential
IEA	International Energy Agency
KIT	Karlsruher Institut für Technologie
MoNiKa	Modularer Niedertemperaturkreislauf Karlsruhe (Modular low-temperature circuit Karlsruhe)
NIST	National Institute of Standards and Technology
NZE	Net Zero Emission
ODP	Ozone Depletion Potential
ORC	Organic Rankine Cycle
REFPROP	Reference Fluid Properties
STEPS	Stated Policies Scenario
VLE-Fluid	Vapour Liquid Equilibrium Fluid

Subscripts

SUBSCRIPT	MEANING
0	Design Conditions
1	Condenser Outlet
2	Feed Pump Outlet
3	Heat Exchanger Outlet
3'	Branch of Bypass Valve
3''	Turbine Inlet
4	Turbine Outlet
4'	Condenser Inlet
abs	Absolute
C	Condenser
char	Characteristic (Length)
Cond	Conduction
Conv	Convection
f	Fluid
g	Gas / Vapor Phase
Gear	Gearbox
Gen	Generator
i	Inner / Inside
is	Isentropic Change of State
l	Liquid
rel	Relative
T	Turbine
th	Thermal
tot	Total

List of Figures

2.1.	Geothermal power plant with a binary cycle	4
2.2.	T-s-Diagram of ORC	5
2.3.	Instrumentation plan of MoNiKa	7
2.4.	Three-Dimensional Representation of the MoNiKa Condenser	11
2.5.	Schematic Structure of the MoNiKa Condenser	12
2.6.	Schematic structure of the heat exchangers in top view	12
2.7.	Schematic representation of the geometric parameters of the heat exchanger	17
2.8.	Structure of VLE-Fluid Cell and Wall Cell in TIL	22
2.9.	Structure of Moist Air Cells in TIL	23
2.10.	Structure of Parallel Flow Heat Exchanger Model in TIL	26
2.11.	Cell connection of Parallel Flow Heat Exchanger Models in TIL	26
2.12.	Exemplary Dymola model with components from TIL	27
3.1.	Enthalpy Calculation for Condenser Inlet for Day0	31
3.2.	Block Diagram of Plant for Calculation of Inlet Enthalpies	32
3.3.	T-s-Diagram for the turbine process	36
3.4.	Comparison of Turbine Efficiencies for different Nitrogen Contents	37
3.5.	Comparison of Turbine Shaft Powers for Day1	39
3.6.	Condenser outlet Enthalpy on different Grids	41
3.7.	Grid Convergence Index	42
3.8.	Example of Filtered and Unfiltered Input Data	44
3.9.	Example of Unfiltered, Filtered and Resampled Input Data	44
3.10.	Validation of Resampling Method	45
3.11.	Comparison of Results for Different Pressure Drop Models	47
3.12.	Evolution of the Condenser Outlet Enthalpies for Day0	51
3.13.	Evolution of the Condenser Outlet Temperatures for Day0	51
3.14.	Modeling of Pressure Drop between Turbine and Condenser	53
4.1.	Results of Turbine Model for Day1	57
4.2.	Filtered Results of Turbine Model for Day1	57
4.3.	Results of Turbine Model for Day2	59
4.4.	Filtered Results of Turbine Model for Day2	59
4.5.	Results of Turbine Model for Day3	60
4.6.	Filtered Results of Turbine Model for Day3	60
4.7.	Condenser Outlet Enthalpy for Day 1	63
4.8.	Condenser Outlet Temperature for Day 1	63
4.9.	Condenser Outlet Enthalpy for Day 2	64
4.10.	Condenser Outlet Temperature for Day 2	64
4.11.	Condenser Outlet Enthalpy for Day 3	65
4.12.	Condenser Outlet Temperature for Day 3	65
4.13.	Evolution of Ambient Temperature by different Sources	66
4.14.	Condenser Outlet Temperature for Day 3 for alternative Ambient Temperature	67

4.15. Turbine Power of Coupled System for Day 1	70
4.16. Temperatures of Coupled System for Day 1	70
4.17. Turbine Power of Coupled System for Day 2	71
4.18. Temperatures of Coupled System for Day 2	71
4.19. Turbine Power of Coupled System for Day 3	72
4.20. Temperatures of Coupled System for Day 3	72
4.21. Sensitivity Study for Coupled System	74

List of Tables

2.1.	Design parameters of the MoNiKa plant	7
2.2.	Relevant sensors in MoNiKa and their measurement accuracy	8
2.3.	Design Parameters of the MoNiKa Turbine	9
2.4.	Geometry parameters of the heat exchanger	17
3.1.	Overview and designation of the relevant MoNiKa test runs	30
3.2.	Fluid Property Calculation in previous Theses	36
3.3.	Models for Development of new Correlation for Turbine Efficiency	38
3.4.	Model for Condenser Grid Sensitivity Study	40
3.5.	Models for Evaluation of Data Preparation	46
3.6.	Models used to compare the Effect of different Pressure Loss Correlations .	47
3.7.	Dymola Condenser Model for Day0	49
3.8.	Deviations between Condenser Models and Experimental Data	49
4.1.	Models for Verification and Validation of Turbine Model	55
4.2.	Deviations between Turbine Models and Experimental Data	58
4.3.	Models for Verification and Validation of Condenser Model	61
4.4.	Deviations between Condenser Model and Experimental Data	62
4.5.	Models for Verification and Validation of Coupled System	68
4.6.	Deviations between Coupled System and Experimental Data	69
4.7.	Selected Stationary Operating Point for Sensitivity Analysis	73
A.1.	Implemented Geometry Parameters of Condenser	87

1. Introduction

1.1. Motivation

At the time of writing this thesis, Europe and the world are in the midst of an energy (and climate) crisis that requires a long overdue rethinking of energy production and security of supply.

The spot market price of gas has reached unprecedented levels, Europe's commodity dependence on foreign exporters has been painfully exposed, and the goals agreed upon in the Paris Climate Agreement seem a long way off.

According to the International Energy Agency's (IEA) World Energy Outlook 2022 [19], as of 2021, more than 750 million people worldwide are still without access to electricity. Most of them are located in sub-Saharan Africa. The report further predicts that as a result of the current energy crisis, this number could rise again for the first time in a decade, as some 75 million people who recently gained access to electricity may soon be unable to pay for it.

In 2021, the global primary energy consumption was about 595 EJ (165,000 TWh) with only 12.75% of that coming from renewable sources [3]. According to the STEPS-Scenario¹, by 2050, this will increase to 740 EJ [19]. The NZE-Szenario² assumes a different trajectory and projects a decrease to 532 EJ by 2050 [19]. However, both scenarios assume a sharp increase in electricity demand from 28EJ in 2021 to 50EJ according to STEPS and 73EJ according to NZE by 2050.

In order to achieve the goals of the Net-Zero-Emissions scenario, namely to limit global warming to the 1.5 degree target set in the Paris Climate Agreement while providing access to electricity for all by 2030, it is envisaged that electricity production from geothermal energy (as of 2020: 94 TWh) will increase to 330 TWh by 2030 and to 821 TWh by 2050 [18].

Geothermal energy can contribute to providing clean, base-load energy in large parts of the world. To do so, it is necessary to research, improve, and ultimately implement facilities for the use of geothermal low-enthalpy reservoirs. The *Modular low-Temperature Circuit*

¹STEPS: abbreviation for *Stated Policies Scenario*: shows a future trajectory based on today's policy settings

²NZE: abbreviation for *Net-Zero-Emissions*: Scenario that maps out a way to achieve a 1.5 °C stabilization in the rise of global average temperatures, alongside with a universal access to modern energy by 2030.

Karlsruhe (MoNiKa) at Campus Nord of the Karlsruhe Institute of Technology, is a test facility designed to research geothermal energy production with thermal water temperatures of 150°C. Such temperatures can be reached at economically feasible site depths in many places in the world. The current research at MoNiKa can therefore contribute to a more environmentally friendly energy supply that is less dependent on foreign energy imports.

1.2. Objective and Approach

The present master thesis is intended to contribute to optimize MoNiKa for varying operating conditions and to provide a model for the simulation of its coupled turbine-condenser unit. The long-term goal is to develop a digital twin of the MoNiKa plant, which then could enable an artificial intelligence to find optimized operating points for measured environmental conditions. This is a task that human machine operators are not able to perform due to the large number of parameters involved and their complex interconnection. Such optimizations hold great economic and ecological potential for future applications and are therefore of great interest in current research questions.

In the run-up to this master's thesis, extensive investigations into the behavior of the MoNiKa turbine [28] and condenser [11] in partial-load operation were undertaken. Based on these findings, a coupled turbine-condenser model is now to be developed using the *Modelica* modeling language with the *Dymola* development environment. For thermodynamic components the commercial library *TIL* is used which provides basic models that can be parameterized and complemented. To calculate the fluid properties of the working fluid (which is a propane-nitrogen mixture) a *Dymola-REFPROP* interface is used.

In a first step, a turbine model must be developed. The correct implementation in *Dymola* should be verified with an already existing *Simulink* turbine model by Julia Filipe [9]. Then the model must be validated with measurement data from various MoNiKa test runs.

Next, a model for the MoNiKa Condenser must be implemented. For this purpose, a condenser model from the commercial *TIL* library is parameterized according to the geometric conditions of the MoNiKa condenser. Afterwards, the adjusted model must be validated with measurement data from various MoNiKa test runs. Furthermore, the results of an already existing *Simulink* condenser model by Mariano Fossati [11] are available for an additional comparison.

Finally, after both models have been verified and validated separately, a coupled turbine-condenser model is to be developed, which again has to be validated with measurement data from three MoNiKa test runs, each with an operational runtime of about 4 hours. When coupling both models, the connecting tubes must also be taken into account, due to its pressure losses.

Furthermore, a sensitivity study is to be carried out in order to estimate the influence of individual parameters on the simulation results and thus to determine critical measured values.

The result of the work should be a validated, coupled turbine-condenser model, which enables improved predictions compared to the existing models for changing operating conditions. In addition, the computation time must be kept within reasonable limits to enable further extensions of the model to complete the MoNiKa cycle.

2. Basic Principles

In the following chapter, the basic principles relevant for understanding the thesis are presented. In addition to the introduction of the MoNiKa facility, the important heat and pressure drop correlations and the software used are introduced.

2.1. Geothermal Energy

Geothermal energy is a renewable energy source produced by the radioactive decay of elements in the earth's interior [37]. About 70% of the heat flow exiting the earth's surface comes from the radioactive decay of natural isotopes in the earth's crust. The isotopes decaying in this process are primarily uranium (^{235}U and ^{238}U), thorium (^{232}Th), and potassium (^{40}K). Another 30% comes from the thermal energy stored in Earth's core and mantle [54][21].

In continental crust of Central Europe the temperature gradient is on average $30 \frac{\text{K}}{\text{km}}$, but positive and negative deviations are possible. Significantly higher and therefore more attractive gradients can be found at plate edges (e.g. Iceland, Larderello in Italy with approx. $200 \frac{\text{K}}{\text{km}}$) or in rift regions (e.g. in the Rhine-Graben with up to $100 \frac{\text{K}}{\text{km}}$) [54][21].

In geothermal energy, a distinction is made between shallow and deep geothermal energy, with the thresholds being drawn at a depth of about 400 m and 20 °C. In deep geothermal energy, a further distinction is made between high-enthalpy reservoirs (i.e. reservoirs with increased geothermal temperature gradients, mostly along plate boundaries or areas with increased volcanic activity) and low-enthalpy reservoirs. The threshold here is usually drawn at a reservoir temperature of 200 °C [54].

Most of the geothermal energy used today for electricity production comes from high-enthalpy reservoirs, which have high temperatures even at low drilling depths. In these plants, the thermal fluid is used directly to drive a turbine and generate electricity in an open dry steam or flash system.

To date, geothermal power generation from low-enthalpy reservoirs has been less common. Since at temperatures below 200°C from an economic point of view the thermal water can no longer be used directly in the steam process, a closed binary system is required. In such, the heat is transferred from the thermal water via a heat-exchanger to an ORC or Kalina cycle, where the actual electricity production takes place. The cooled thermal water is then re-injected into the reservoir [54] [63]. The schematic structure of such a binary cycle is shown in Figure 2.1.

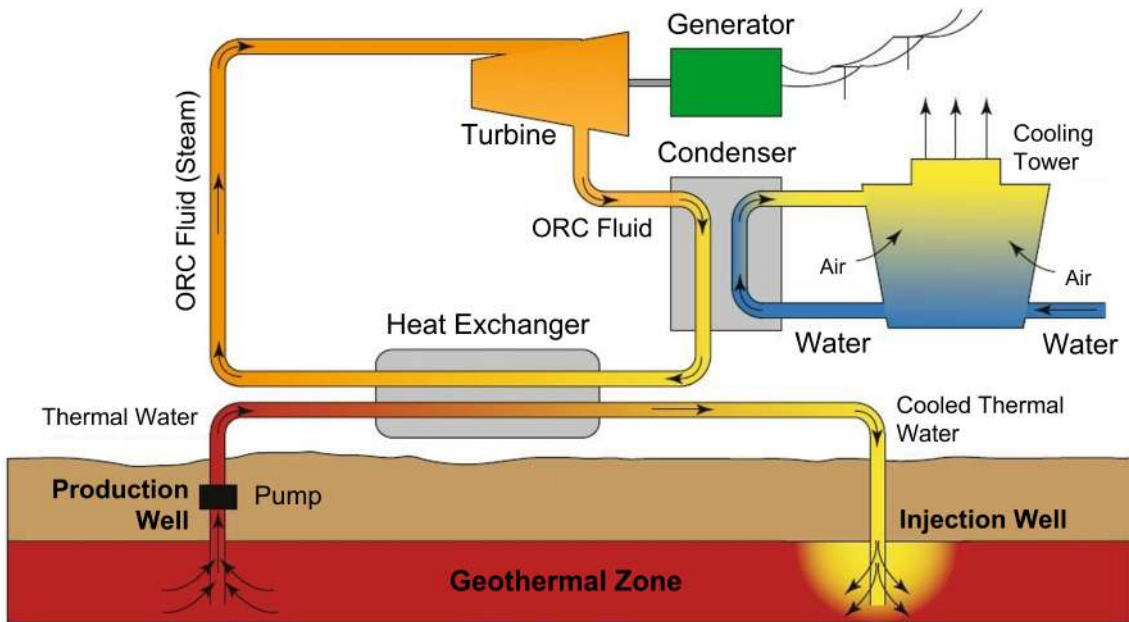


Figure 2.1.: Schematic representation of a geothermal power plant with a binary cycle. (image translated to English from [54])

In Germany, no high enthalpy reservoirs are available. In the economically feasible drilling depths of up to 5000m, temperatures of 100°C - 170°C prevail, which means that only binary systems are feasible [63].

In order to increase the economic efficiency of the plants, a heat extraction in addition to the electricity production can take place, which is fed into the local or district heating network.

A geothermal energy source is independent of season and weather¹, available almost everywhere and base load capable. The capacity factor of modern geothermal plants can reach up to 95% [17]. In addition, no storage is necessary since geothermal heat as a primary energy is naturally available and stored in the earth's interior. Thus, a demand-oriented, raw material-independent use is possible [21].

To investigate the optimization possibilities for binary geothermal plants, the MoNiKa test facility at KIT was designed and built as a modular power plant with a thermal output of 1000 kW. The facility will be explained in detail in Chapter 2.3.

2.2. Organic Rankine Cycle

Low-temperature geothermal heat with temperature levels of 100-200°C is usually no longer used directly in a steam process. As described in the previous chapter, a binary cycle is then necessary in which the heat extracted from the thermal water is transferred to a secondary cycle.

The Clausius-Rankine cycle used in coal and nuclear power plants is unsuitable for such temperature levels, since efficient conversion requires high temperatures and pressures [21]. Therefore, in low-temperature processes, instead of water, an organic working fluid with lower boiling temperature and pressure is used in the secondary cycle. Such a process is called an Organic Rankine Cycle, abbreviated as *ORC* in the following.

¹The geothermal heat source itself is independent of any seasonal influences. However, the net power of the plant is dependent on the ambient temperature due to its influence on the condensation temperature.

As the name suggests, the working principle of the cycle is the same as that of the Clausius-Rankine cycle. Its changes of state, as shown in figure 2.2 are ideally:

- ① → ② : Isentropic compression under supply of work in pump
- ② → ③ : Isobaric heat addition in heat exchanger
- ③ → ④ : Isentropic expansion under release of work in turbine
- ④ → ① : Isobaric heat rejection in condenser

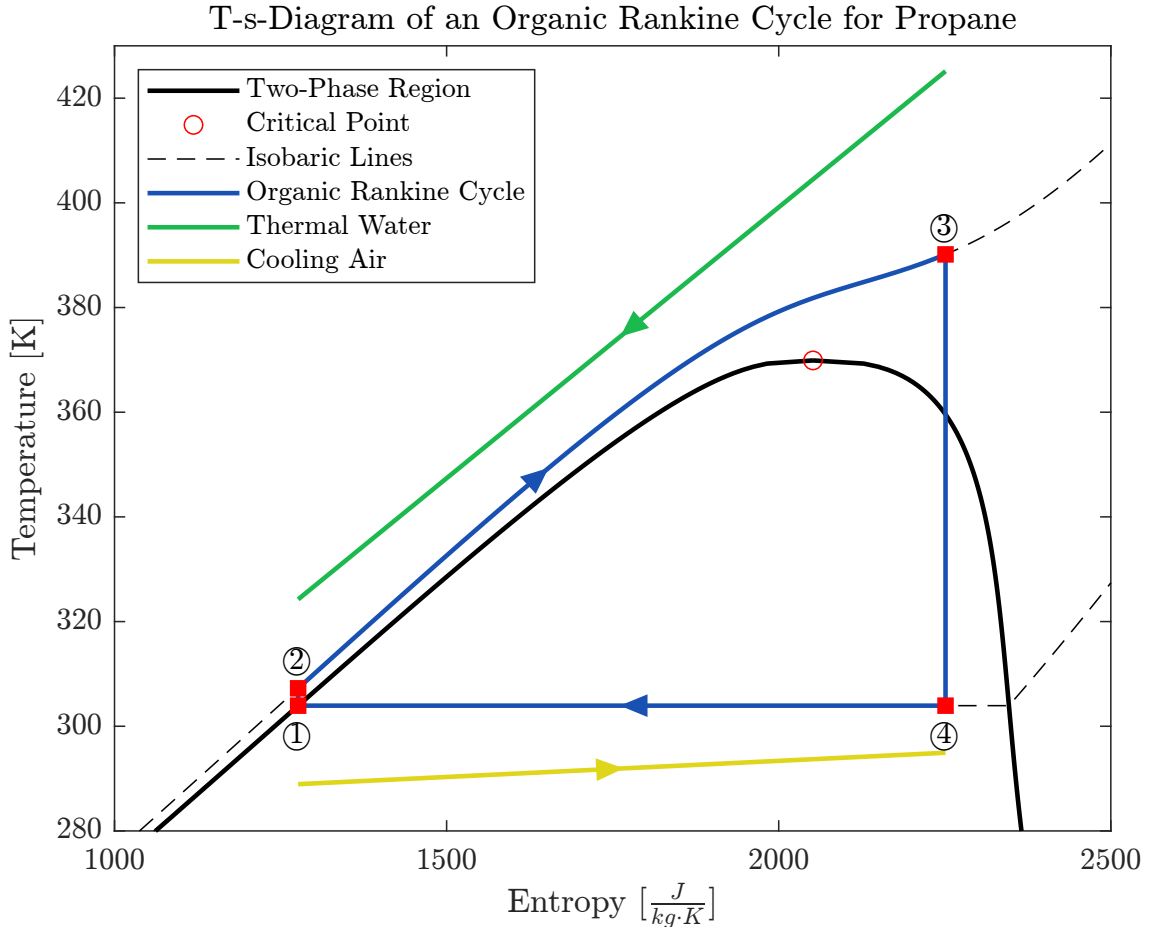


Figure 2.2.: T-s-Diagram of a supercritical Organic Rankine Cycle using propane as working fluid.

A variety of possible working fluids are available for ORC operation. An initial selection can be made according to the properties of the available heat source. In the temperature range below 180°C, which is interesting for geothermal applications, various refrigerants are used as working fluids. At higher temperatures up to 250°C, hydrocarbons show favorable properties [62]. As Vetter [63] describes in his dissertation, the slope of the dew-line is another selection criterion whereby isentropic fluids (fluids for whose dew-line holds: $\frac{dS}{dT} \approx 0$) are to be preferred. Also to be considered are specific volume, corrosivity, toxicity, and thermal conductivity. In addition, fluids with low Global-Warming-Potential (GWP) and low Ozone-Depletion-Potential (ODP) should be preferred [21].

The thermal efficiency of the ORC is defined as follows:

$$\eta_{th} = \frac{P_{Turb} - P_{Pump}}{\dot{Q}_{in}} = \frac{(h_3 - h_4) - (h_2 - h_1)}{h_3 - h_2}. \quad (2.1)$$

The thermal efficiency describes what proportion of the heat supplied is available as usable energy. However, it does not take into account the efficiency of the heat transfer itself. It

is possible that a process with a higher thermal efficiency delivers less useful power if less heat can be extracted from the thermal water. Hence, thermal efficiency alone is not a suitable indicator for evaluating the cycle.

Therefore, when using ORCs for geothermal power generation, the quality of the heat supply is of great importance. This depends on the temperature characteristics of the working fluid and the thermal water in the heat exchanger. Maximum heat extraction of the thermal water at a given heat exchanger grade is achieved when both temperature lines are as parallel as possible. These lines are shown as the green line and the blue line from state point 2 to state point 3 in Figure 2.2.

As a means of quantifying the efficiency of the heat transfer, the exergetic efficiency of the heat exchanger as explained in Vetter [63] can be used:

$$\eta_{ex} = \frac{\dot{m}_{ORC} [(h_4 - h_3) - T_{amb}(s_4 - s_3)]}{\dot{m}_{th} [(h_{th,in} - h_{th,out}) - T_{amb}(s_{th,in} - s_{th,out})]} \quad (2.2)$$

In the above equation the subscript *th* refers to the thermal water from which the heat is extracted. The indices *in* and *out* refer to the incoming and outgoing flow of the heat exchanger. T_{amb} is the ambient Temperature in Kelvin.

Vetter [63] examined super- and sub-critical ORCs of various working fluids with regard to the net power achieved and the thermal efficiency. As Vetter showed, there is no direct correlation between thermal efficiency and specific net power. Vetter further recognized that supercritical ORCs generally showed a better adjustment of the temperature curves than subcritical ORCs. Thus, a significantly higher exergetic efficiencies was achieved in the heat exchanger. Overall, this resulted in a higher net power output of the plant, despite the lower thermal efficiency of the supercritical ORCs. Working fluids whose critical temperature is in the range of 0.8 - 0.9 times the temperature (in Kelvin) of the heat source have proven to be particularly advantageous.

2.3. MoNiKa

The MoNiKa (Modular low-Temperature Circuit Karlsruhe) plant was built at the Campus North of the Karlsruhe Institute of Technology (KIT) to investigate optimization possibilities of ORCs in geothermal power production.

The thermodynamic design of the system was carried out by Christian Vetter as part of his doctorate (see [63]). The design parameters of the facility are listed in Table 2.1. As geothermal drilling is capital intensive and can account for up to 70% [54] of total capital expenditure of a deep geothermal power plant, the 1000 kW thermal heating capacity is provided by a oil fired boiler.

As Vetter describes in his dissertation, the supercritical ORCs he investigated achieved an up to 44% increased net power output compared to sub-critical cycles due to better heat transfer and thus greater heat extraction of the thermal water [63]. The thermodynamic cycle in MoNiKa was therefore designed as a supercritical process. Vetter investigated a total of 12 different working fluids with regard to the net power achieved. However, the fluids with the highest net power output had an increased Global Warming Potential (GWP) which is why propane was ultimately chosen as the working fluid. Propane shows a relatively low GWP of 3, an Ozone Depletion Potential (ODP) of 0 and further has a short atmospheric lifetime [20].

Table 2.1.: Design parameters of the MoNiKa plant

SYMBOL	PARAMETER	VALUE
$P_{thermal}$	Thermal power at full load	1000 kW
$T_{thermal}$	Temperature of thermal water	150 °C
T_3	Temperature of ORC fluid at heat exchanger outlet ¹	117 °C
T_4	Condensation temperature ²	30 °C
\dot{m}	Mass flow of ORC fluid	2.9 $\frac{kg}{s}$

¹ Due to problems in the heat exchanger, only a maximum temperature of 112°C is reached in the real plant.

² The condensation temperature naturally depends strongly on the ambient temperature and therefore varies.

2.3.1. Instrumentation

The schematic structure of MoNiKa with the most important components and the measuring devices relevant for the thesis are shown in Figure 2.3. Table 2.2 contains detailed information on the sensors and their measurement deviation. The notation introduced in the diagram for the state points ① to ④' is from now on always used in this way.

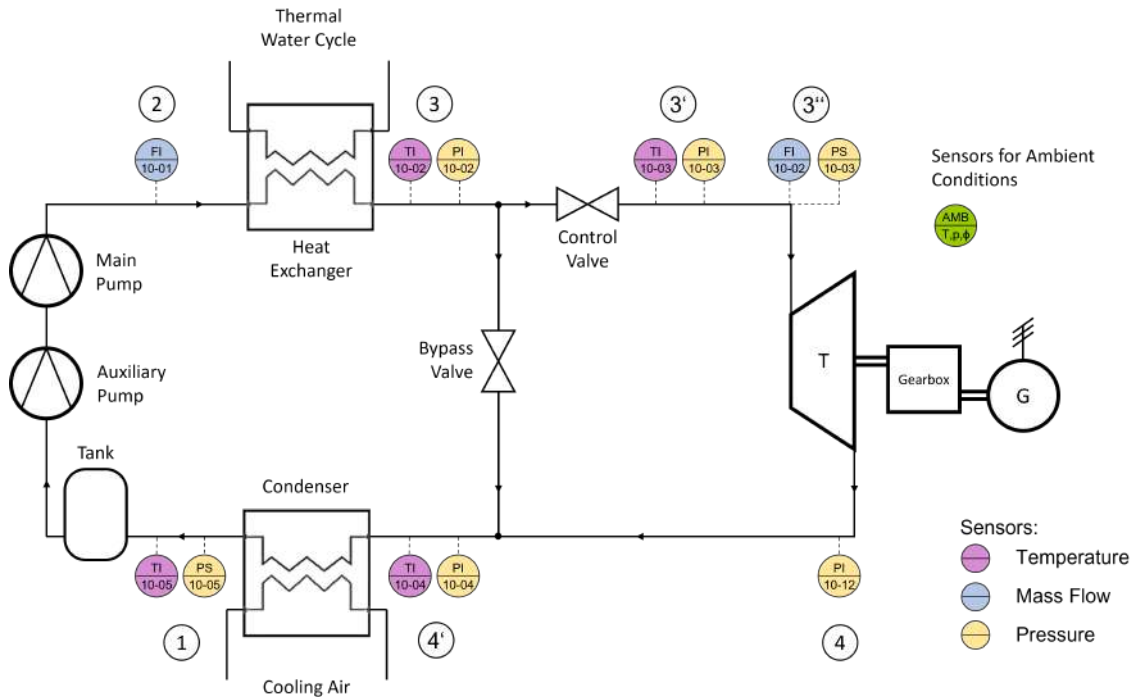


Figure 2.3.: Instrumentation plan of MoNiKa containing the most important components and all sensors that were used for this thesis.

The mass flow in the ORC is controlled by the rotational speed of the main piston pump. An upstream centrifugal pump serves as an auxiliary pump to increase the pressure level of the liquefied propane to such an extent that no cavitation occurs in the main pump. The heat exchanger is designed as a tube-bundle. However, it reaches a significantly lower heat transfer than intended in the design, so that the working fluid cannot be heated to the intended temperature. Therefore, instead of the planned 117°C at the heat exchanger outlet, only 112°C can be reached and this only at an decreased mass flow rate. During operation, both mass flow and turbine inlet temperature therefore do not reach the design parameters and hence, the facility is exclusively operated at partial load.

Table 2.2.: Relevant sensors in MoNiKa and their measurement accuracy

SENSOR CODE	STATE VARI-ABLE	MODEL / TYPE	MEASUR. RANGE	ACCURACY	MAX. ABS. ERROR ¹
PI 10-02	Press.	Vegabar 81	0 - 100 bar	±0.2%	0.11 bar
PI 10-03	Press.	Vegabar 81	0 - 100 bar	±0.2%	0.11 bar
PS 10-03	Press.	Vegabar 81	0 - 100 bar	±0.2%	0.11 bar
PI 10-12	Press.	Vegabar 82	-1 - 100 bar	±0.1%	0.011 bar
PI 10-04	Press.	Vegabar 82	-1 - 100 bar	±0.1%	0.011 bar
PS 10-05	Press.	Vegabar 81	0 - 100 bar	±0.2%	0.022 bar
TI 10-02	Temp.	WIKA TR34-B-P4 PT100 A 4	-50 - 250 °C	±(0.15±0.0020· T °C)	0.384 °C
TI 10-03	Temp.	WIKA TR34-B-P4 PT100 A 4	-50 - 250 °C	±(0.15±0.0020· T °C)	0.384 °C
FI 10-02 ²	Temp.	Endress+Hauser Proline Promass 83F	-50 - 200 °C	±(0.5±0.005· T °C)	1.085 °C
TI 10-04	Temp.	WIKA TR34-B-P4 PT100 A 4	-50 - 250 °C	±(0.15±0.0020· T °C)	0.21 °C
TI 10-05	Temp.	WIKA TR34-B-P4 PT100 A 4	-50 - 250 °C	±(0.15±0.0020· T °C)	0.21 °C
FI 10-01	Mass Flow	Endress+Hauser Proline Promass 83F	0-70000 $\frac{kg}{h}$	±0.1 %	0.0029 $\frac{kg}{s}$
Amb	Temp. Hum.	E+E Elektronik EE33 T4	-40 - 120 °C 0 - 100%	±0.09% ³ ±(1.3 + 0.003 · φ)%	
Amb	Press.	WIKA S-20	0 - 1.6 bar	±0.25%	

¹ The maximum measurement deviation to be expected relates to the operating conditions at full load as presented in Table 2.1.

² Sensor FI 10-02 is a mass flow meter that also measures temperature. During the test runs, however, the mass flow measurement failed so that only the temperature data could be used.

³ The specified relative deviation refers to an ambient temperature of 0°C. For other temperatures, the measurement deviation can be higher and must be read from a diagram in the manufacturer's user manual.

2.3.2. MoNiKa Turbine

The installed propane expander is a four-stage impulse turbine, manufactured by M+M Turbinen-Technik GmbH. The design parameters of the turbine are given in Table 2.3. According to the user manual, the steam quality in the turbine must not fall below 90% to avoid blade damage from drop impact [30]. However, due to the deviations from the design point of the plant, the maximum moisture content is often exceeded. The experience gained with the system shows that the turbine can be operated safely up to a moisture content of 20%.

Table 2.3.: Design parameters of the turbine according to the manufacturers data sheet [30]

SYMBOL	PARAMETER	VALUE
$p_{3''}$	Pressure at turbine inlet	5.5 MPa
p_4	Pressure at turbine outlet	1.1 MPa
$T_{3''}$	Temperature at turbine inlet	117 °C
\dot{m}	Massflow through turbine at full load	2.9 $\frac{kg}{s}$
n	Revolutions per minute	9960 $\frac{1}{min}$
P_T	Rated capacity	91 kW

The turbine shaft is flanged to a 4-pole three-phase synchronous generator via a gearbox. The gearbox has a gear ratio of 1:6.64 and a efficiency of $\eta_{Gear} = 99.18\%$ [30][28]. The generator has an efficiency of $\eta_{Gen} = 94.60\%$ [28]. With this information, the shaft power of the turbine produced in the test runs can be calculated from the measurement of the generator power as follows :

$$P_T = \frac{P_{Gen}}{\eta_{Gear} \cdot \eta_{Gen}} \quad (2.3)$$

The ORC working fluid of MoNiKa is propane. Since it is a flammable gas, leakage from the ORC must be prevented for the purpose of explosion protection. The circuit is largely closed, which means that leakage can be ruled out. An exception is the exit of the turbine shaft from the housing, which is then connected to the gearbox. To prevent propane leakage, 3 sealing stages are installed. Furthermore, nitrogen is introduced as a sealing gas between the first and second seal. Between the second and third seal, the nitrogen-propane mixture is then discharged. It is assumed that no nitrogen enters the ORC during operation. However, during the start-up of the plant, when there is still no back-pressure at the turbine outlet, nitrogen enters the propane circuit.

In the previous theses it was assumed that the nitrogen content in the ORC is 0.2%. However, a more recent examination carried out by Prof. Dr. Thomas Schulenberg estimates that the actual nitrogen content during the test runs examined was 2.58 Mol% which is an equivalent of 1.65 Mass%. In the estimate the nitrogen content was determined by matching the temperature and pressure measurement data at the condenser inlet, assuming a steam quality of 1.

2.3.2.1. Energy Balance of Turbine

The first law of thermodynamics for any control space can be written in its general form as shown below [1]. For the turbine it is assumed that the heat loss through the turbine walls is negligible. In addition, it is assumed that the changes in kinetic and potential energy are negligible and that the turbine operation is stationary.

$$\underbrace{\sum \dot{Q}}_{\approx 0, \text{ neglect heat losses}} + \sum \dot{W} + \sum \dot{m} \left(\underbrace{h + \frac{c^2}{2} + gz}_{\approx h, \frac{\Delta c^2}{2} + g\Delta z \ll \Delta h} \right) = \underbrace{\frac{dE}{dt}}_{= 0, \text{ stationary state}} \quad (2.4)$$

Assuming now that no mass accumulates in the turbine ($\dot{m}_{3''} = -\dot{m}_4 = \dot{m}_T$) then the following applies to the turbine shaft power P_T :

$$P_T = \dot{W} = -\dot{m}_T (h_{3''} - h_4) \quad (2.5)$$

2.3.2.2. Isentropic Efficiency of Turbine

As can be seen in Equation 2.5, the enthalpy at the turbine inlet and outlet must be known in order to calculate the turbine power. However, for the simulation the outlet enthalpy is not known beforehand. Therefore, the isentropic turbine efficiency is used to determine it. The isentropic turbine efficiency is the ratio of the actual work output of a turbine to the theoretical work output if the turbine was operating at isentropic conditions and is defined as follows [61]:

$$\eta_{is,T} \equiv \frac{\Delta h}{\Delta h_{is}} = \frac{h_{3''} - h_4}{h_{3''} - h_{4,is}} \quad (2.6)$$

As part of Joaquín Perez's master thesis [28], an empirical correlation for the isentropic efficiency of the MoNiKa turbine was developed from the test runs of the MoNiKa plant:

$$\eta_{is,T} = 0.4412 - 0.4399 \frac{\text{s}}{\text{kg}} \cdot \dot{m}_T + 0.3229 \frac{1}{\text{MPa}} \cdot p_{3''} \quad (2.7)$$

Applicability limits for the turbine efficiency correlation:

Mass flow:	2.1	<	\dot{m}_T	<	2.6	$\left[\frac{\text{kg}}{\text{s}} \right]$
Pressure:	3.86	<	$p_{3''}$	<	4.64	$[\text{MPa}]$
Temperature:	363.5	<	$T_{3''}$	<	374	$[\text{K}]$

2.3.2.3. Stodola's Cone Law

Stodola's cone law, sometimes also referred to as *Law of the Ellipse* provides a empirical approach for calculating the steam flow through a turbine as a function of the inlet pressure $p_{3''}$, the inlet temperature $T_{3''}$ and the back pressure p_4 [55] (for further information see also [22]). It is a widely used method to estimate the partial load behavior of turbines and reads in the formulation of Strauss [56] as:

$$\frac{\dot{m}}{\dot{m}_0} = \sqrt{\frac{p_{3''}^2 - p_4^2}{p_{3'',0}^2 - p_{4,0}^2} \frac{T_{3'',0}}{T_{3''}}} \quad (2.8)$$

The index 0 refers to the design point of the turbine which was summarized in Table 2.3. Due to the high deviations of the plant from its design point, the turbine operates exclusively under partial load conditions. To improve the estimate of the inlet pressure for a given mass flow, a empirical correction of the Stodola equation was introduced on

the basis of test runs of MoNiKa. The procedure is described in Joaquín Perez's master's thesis [28] and results in:

$$\frac{\dot{m} + 1.3352 \frac{\text{kg}}{\text{s}}}{\dot{m}_0} = \sqrt{\frac{p_{3''}^2 - p_4^2}{p_{3'',0}^2 - p_{4,0}^2} \frac{T_{3'',0}}{T_{3''}}} \cdot 1.5442 \quad (2.9)$$

Applicability limits for the corrected Stodola equation:

Mass flow:	$1.88 < \dot{m}_T < 2.74$	$[\frac{\text{kg}}{\text{s}}]$
Pressure:	$3.86 < p_{3''} < 4.90$	$[\text{MPa}]$
Temperature:	$363.5 < T_{3''} < 376.5$	$[\text{K}]$

2.3.3. MoNiKa Condenser

The MoNiKa condenser as shown in Figure 2.4 and Figure 2.5 consists of 4 heat exchangers arranged in a V-shape, 3 induced draft type fans and an optional water injection. In all test runs examined in this thesis, the condenser was operated dry, i.e. without water injection, which is why this is not considered further in the following. The fluid on the ORC side is propane or a propane-nitrogen mixture and moist air is used as the cooling medium.

The heat exchangers are designed as fin-and-tube cross-flow heat exchangers. Each of them consist of 69 parallel pipe coils of which each contains 4 pipes that are connected in series. The schematic structure of a single heat exchanger is shown in Fig.2.6. In order to increase the heat transfer surface, a total of 2000 fins per heat exchanger are attached to the pipes. All pipes are made of stainless steel whereas the fins are made of an aluminum alloy.

In all of the test runs examined, the fans were always operated at full load, after which $528000 \frac{\text{m}^3}{\text{h}}$ ($146.67 \frac{\text{m}^3}{\text{s}}$) of cooling air were drawn in according to the manufacturer's process and plant description [25].

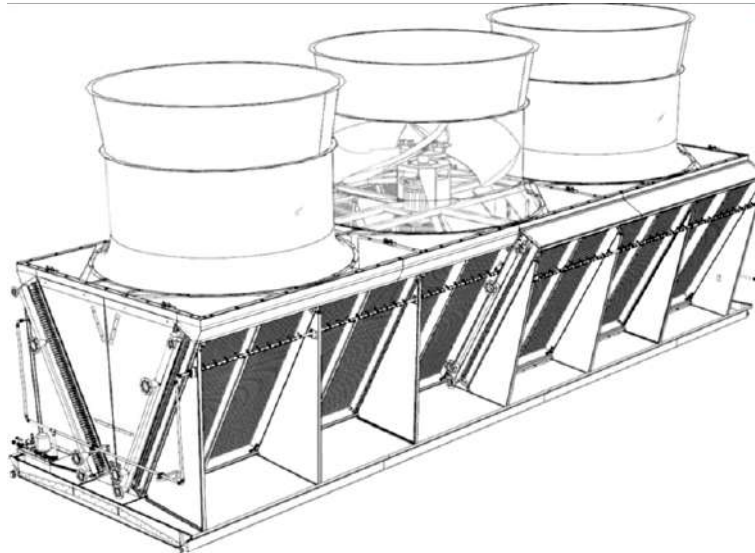


Figure 2.4.: Three-dimensional representation of the MoNiKa condenser unit from the manufacturers process and plant description [25].

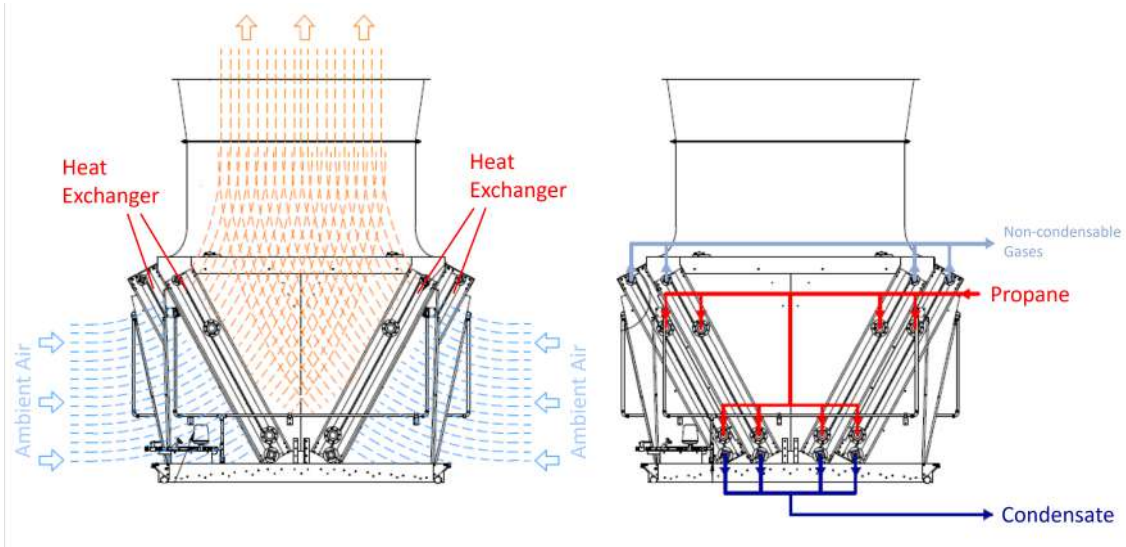


Figure 2.5.: Schematic structure of the MoNiKa condenser from the manufacturers process and plant description [25]. (Text translated to English)

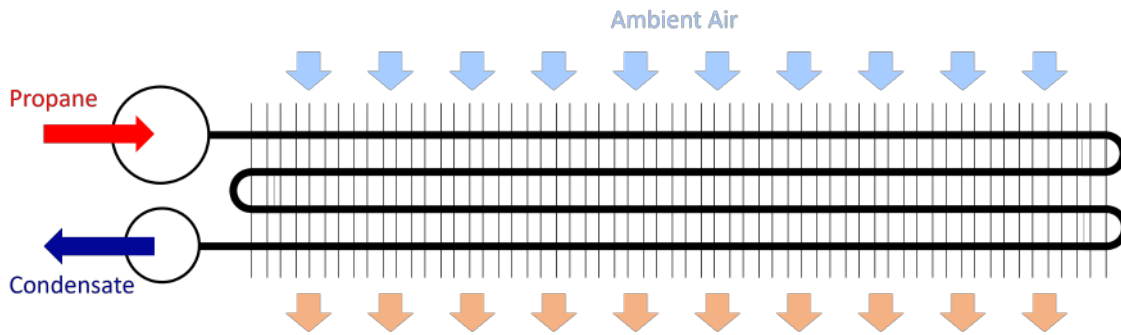


Figure 2.6.: Schematic structure of the heat exchangers in top view. Each of the 4 heat exchangers consists of 69 of the illustrated tube coils which are arranged one above the other. Two vertical tubes as shown on the left side of the figure distribute and collect the propane or the condensate to this 69 parallel coils.

2.4. Heat Transfer

To model the condenser, the heat transferred between ORC fluid and cooling air must be determined. Since the calculation methods presented here are only valid for constant or averaged material values and temperatures, it is necessary to discretize the condenser into a sufficiently large number of cells. The total heat flow transferred can then be calculated as [41]:

$$\dot{Q} = kA\Delta T_{ln} \quad (2.10)$$

where k is the overall averaged heat transfer coefficient or thermal conductivity related to the heat transfer area A . ΔT_{ln} is the mean logarithmic temperature difference between the inlet and outlet temperatures of the two fluids and is calculated as:

$$\Delta T_{ln} = \frac{\Delta T_1 - \Delta T_2}{\ln\left(\frac{\Delta T_1}{\Delta T_2}\right)} \quad (2.11)$$

For the sake of clarity, in equation 2.10 the thermal heat transfer coefficient will be substituted by the thermal resistance R . The thermal resistance is defined as [52]:

$$R = \frac{1}{kA} \quad (2.12)$$

The total heat resistance of the condenser includes the resistance of convective heat transfer from the ORC fluid to the tube walls ($R_{Conv,TubeSide}$), conductive heat transfer in radial direction in the tube walls ($R_{Cond,Wall}$), and convective heat transfer between fins and cooling air ($R_{Conv,AirSide}$). In the case of the latter, the heat transport in the fins is taken into account by applying a fin efficiency model. Furthermore, a fouling resistance $R_{Fouling}$ can be taken into account.

The total heat resistance in the case of the condenser can then be determined as follows:

$$R = R_{Conv,TubeSide} + R_{Cond,Wall} + R_{Conv,AirSide} + R_{Fouling} \quad (2.13)$$

In the context of this thesis it is assumed that the fouling resistance, caused by the unwanted accumulation of material on the surfaces, is negligible. The determination of the other resistances is explained in the following sections.

2.4.1. Tube-side Heat Transfer

For convective heat transfer the heat resistance can be calculated as [52]:

$$R_{Conv,TubeSide} = \frac{1}{\alpha_i A_i} \quad (2.14)$$

where the subscript i refers to the tube inside. The difficulty with convective heat transfer is determining the heat transfer coefficient α . It can be determined using the Nusselt number, defined as follows:

$$Nu = \frac{\alpha \cdot l_{char}}{\lambda_f} \quad (2.15)$$

where l_{char} is the characteristic length and λ_f the heat conduction coefficient of the fluid. The heat transfer coefficient can then be determined from the Nusselt number via empirical correlations. In these correlations the Nusselt number is usually expressed as a function of the Reynolds number Re and the Prandtl number Pr , which are defined as follows:

$$Re = \frac{w \cdot l_{char}}{\nu} \quad (2.16)$$

$$Pr = \frac{\rho \cdot \nu \cdot c_p}{\lambda_f} \quad (2.17)$$

with w being the flow velocity, ρ the density, ν the kinematic viscosity of the fluid and c_p the specific heat capacity at constant pressure.

For the determination of α for the convective heat transfer between the fluid and the tube wall it must be distinguished between single-phase flow and two-phase flow:

Single-Phase

For single-phase laminar flow with $Re < 2300$, a constant Nusselt number can be used according to Baehr [2]:

$$Nu = 3.6568 \quad (2.18)$$

In the range $2300 \leq Re < 100000$ the Nusselt number is calculated according to Gnielinski [15] as written below. This correlation requires the additional condition $0.5 \leq Pr \leq 2000$ and a ratio of tube length to inner diameter of $\frac{L}{d_i} > 1$.

$$Nu = \frac{\frac{\xi}{8} \cdot (Re - 1000) \cdot Pr}{1 + 12.7 \sqrt{\frac{\xi}{8}} \cdot (Pr^{2/3} - 1)} \quad (2.19)$$

with

$$\xi = \frac{1}{(0.79 \cdot \ln(Re) - 1.64)^2} \quad (2.20)$$

For higher Reynolds numbers the Nusselt correlation of Colburn is used [5] [57]:

$$Nu = 0.023 \cdot Re^{\frac{4}{5}} \cdot Pr^{\frac{1}{3}} \quad (2.21)$$

Two-Phase

During Condensation both, a liquid and a vapor phase coexist. An adequate correlation for this case has to be chosen. In 1979 Shah presented the paper *A General Correlation For Heat Transfer During Film Condensation Inside Pipes* [43] which found wide acceptance. In this approach the heat transfer coefficient for liquid single phase is multiplied by an empirical two phase factor which is a function of pressure, critical pressure and quality of the fluid. Due to it's limitations to high flow rates and moderate pressures, Shah presented an improved version in 2009 [44] and 2013[45] which extends its applicability to lower flow rates and higher pressures. The correlation as proposed in the 2013 paper is explained in the following.

The Correlation is based on the following two heat transfer correlations. The first equation is the correlation of Shah (1979) supplemented by an viscosity ratio factor:

$$\alpha_I = \alpha_{LS} \cdot \left(1 + \frac{3.8}{Z^{0.95}}\right) \left(\frac{\mu_l}{14\mu_g}\right)^{0.0058+0.557Pr} \quad (2.22)$$

The second equation is the Nusselt equation for laminar film condensation with an adjusted constant factor:

$$\alpha_{Nu} = 1.32 \cdot Re_{LS}^{-\frac{1}{3}} \cdot \left[\frac{\rho_l(\rho_l - \rho_g)gk_l^3}{\mu_l^2}\right]^{\frac{1}{3}} \quad (2.23)$$

In the above equations μ is the dynamic viscosity where the subscript l refers to the liquid and g to the vapor phase. The parameter g is the acceleration due to gravity and k is the thermal conductivity. α_{LS} is the heat transfer coefficient of the liquid phase and is calculated as:

$$\alpha_{LS} = 0.023 \cdot Re_{LS}^{0.8} \cdot Pr_l^{0.4} \cdot \frac{k_l}{d} \quad (2.24)$$

where d is the inner diameter of the tube and Re_{LS} is the Reynolds number, assuming the liquid phase is flowing alone. Z is a empirical correlating parameter introduced by Shah

(1979), defined as:

$$Z = \left(\frac{1}{x} - 1 \right)^{0.8} \cdot p_r^{0.4} \quad (2.25)$$

where x is the steam quality and p_r is the reduced pressure defined as:

$$p_r = \frac{p}{p_{crit}} \quad (2.26)$$

Using the above equations the heat transfer coefficient α can now be determined. At the calculation three heat transfer regimes are distinguished:

Regime I: turbulent

$$\alpha = \alpha_I \quad (2.27)$$

Regime II: mixed

$$\alpha = \alpha_I + \alpha_{Nu} \quad (2.28)$$

Regime III: laminar

$$\alpha = \alpha_{Nu} \quad (2.29)$$

Which regimen prevails is determined by the dimensionless vapor velocity J_g , which is defined as:

$$J_g = \frac{x \cdot G}{(g \cdot d \cdot \rho_g \cdot (\rho_l - \rho_g))^{0.5}} \quad (2.30)$$

where G is the total mass flow of liquid and vapor and x is the steam quality.

Regime I occurs for the following condition:

$$J_g \geq 0.98 \cdot (Z + 0.263)^{-0.62} \quad (2.31)$$

Regime III occurs when:

$$J_g \leq 0.95 \cdot (1.254 + 2.27 \cdot Z^{1.249})^{-1} \quad (2.32)$$

Otherwise regime II prevails.

2.4.2. Heat Conduction in Tube Wall

The radial thermal resistance in the wall of a circular tube can be calculated according to the VDI-Wärmeatlas [50] as:

$$R_{Cond,Wall} = \frac{\delta}{\lambda A_m} \quad (2.33)$$

with:

$$A_m = \frac{A_2 - A_1}{\ln(A_2/A_1)} \quad (2.34)$$

where $A_1 = 2\pi r_1 L$ is the inner lateral surface of the tube, A_2 is the outer lateral surface and $\delta = r_2 - r_1$ is the tube wall thickness. λ is the thermal conductivity of the wall material.

2.4.3. Air-side Heat Transfer

For the finned tube heat exchanger used in the MoNiKa condenser, the air-sided heat transfer coefficient can be determined with the Nusselt number correlation proposed by Haaf [49]:

$$Nu = 0.31 \cdot Pr^{\frac{1}{3}} \cdot Re^{0.625} \cdot \left(\frac{d_{ae}}{d_s}\right)^{\frac{1}{3}} \quad (2.35)$$

where d_s is the distance of the heat exchanger rows (serial tube distance). The characteristic length d_{ae} , which is also used to determine the Reynolds number, is calculated as follows:

$$d_{ae} = \frac{4V_{tot}\Psi}{A_{tot}} \quad (2.36)$$

where V_{tot} is the total finned volume, A_{tot} the total heat exchanger area of the air side and Ψ the void ratio. Those are calculated as follows:

$$A_{tot} = \left(\underbrace{2 \cdot (d_s d_p - \frac{\pi}{4} d_o^2)}_{\text{Fin Area}} \cdot n_f + \underbrace{\pi \cdot d_o \cdot L_t}_{\text{total tube outer area}} - \underbrace{\pi \cdot d_o \cdot t_f \cdot n_f}_{\text{tube outer area covered by fins}} \right) \cdot n_t \quad (2.37)$$

$$V_{tot} = h_{hx} \cdot l_{hx} \cdot d_{hx} \quad (2.38)$$

$$\Psi = 1 - \frac{t_f}{p_f} - \frac{\pi d_o^2 (p_f - t_f)}{4 d_s d_p p_f} \quad (2.39)$$

Due to the large number of geometrical parameters used in this section, these are resumed in Table 2.4 and visually represented in Figure 2.7. The average flow velocity, which is required to determine the Reynolds number, results from the flow velocity of the free external flow w_0 and the void fraction Ψ :

$$w_{mean} = \frac{w_0}{\Psi} \quad (2.40)$$

The calculated heat transfer coefficient assumes a spatially constant temperature of the fins. However, since the surface temperature decreases from the tube to the tip of the fin, a precise calculation of the heat transfer would require a discretization of the fins. Due to the resulting computational effort and increased complexity, a fin efficiency approach is used instead, where the heat transfer coefficient is corrected with the fin efficiency η_f .

The heat transfer coefficient related to the entire surface is called the apparent heat transfer coefficient α_{app} , which is calculated from the heat transfer coefficient α_{fin} (calculated with Haaf) and the fin efficiency:

$$\alpha_{app} = \alpha_{fin} \left(1 + \frac{A_{fin}}{A_{tot}} \cdot (\eta_f - 1) \right) \quad (2.41)$$

The fin efficiency resembles the ratio of the actual heat transfer coefficient and the heat transfer coefficient in case of isothermal fins. The value of the fin efficiency can be calculated with the method of Schmidt [42]:

SYMBOL	EXPLANATION
A_{tot}	total (fin-side) heat transfer area
d_{ae}	equivalent diameter (characteristic length)
d_{hx}	total depth of heat exchanger
d_o	tube outer diameter
d_p	parallel tube distance
d_s	serial tube distance
h_{hx}	total height of heat exchanger
l_{hx}	total length of heat exchanger
L_t	finned tube length
n_f	total number of fins
n_t	total number of tubes
p_f	fin pitch
t_f	fin thickness
V_{tot}	total heat exchanger volume

Table 2.4.: Geometry parameters of the heat exchanger

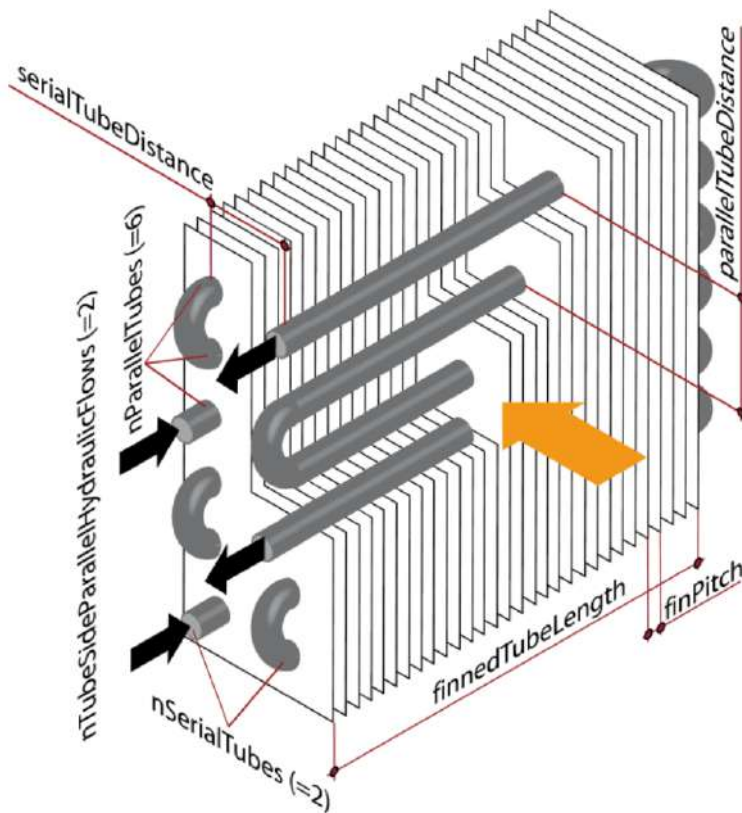


Figure 2.7.: Schematic representation of the geometric parameters of the heat exchanger. (picture from the documentation of TIL [59])

$$\eta_f = \frac{\tanh(X)}{X} \quad (2.42)$$

with

$$X = h_{eff,fin} \cdot \left(\frac{2\alpha}{\lambda_{fin} t_f} \right)^{0.5} \quad (2.43)$$

where $h_{eff,fin}$ is the effective fin height, calculated as:

$$h_{eff,fin} = \frac{d_o}{2} \left(\frac{Re_q}{r} - 1 \right) \left(1 + 0.35 \cdot \ln \left(\frac{Re_q}{r} \right) \right) \quad (2.44)$$

$\frac{Re_q}{r}$ is the diameter ratio and can be calculated as:

$$\frac{Re_q}{r} = 1.27 \cdot \frac{d_p}{d_o} \cdot \left[\left(0.25 + \left(\frac{d_s}{d_p} \right)^2 \right)^{0.5} - 0.3 \right]^{0.5} \quad (2.45)$$

The overall air-side heat resistance can then be calculated as:

$$R_{Conv,AirSide} = \frac{1}{\alpha_{app} A_{tot}} \quad (2.46)$$

2.5. Pressure Loss

The following equation from the VDI-Wärmeatlas can be used as a basis for calculating the pressure loss of any flow [33]:

$$\Delta p = \xi a \frac{\rho}{2} w^2 \quad (2.47)$$

where ξ is the pressure loss coefficient, ρ the density and w the flow bulk velocity. The form factor a is defined depending on the type of flow problem. The correlations used for the pressure loss coefficient and the definition of the form factor for the pressure losses that occur are explained in the following sections.

2.5.1. Pressure Loss in Tubes

For circular tubes, the form factor a is calculated from the length of the tube l and the inner diameter d_i [32]:

$$a = \frac{l}{d_i} \quad (2.48)$$

For the calculation of the pressure loss coefficient, a distinction is made between laminar and turbulent flow. For laminar flows ($Re \leq 2300$) the Hagen-Poiseuille relation applies [32]:

$$\xi = \frac{64}{Re} \quad (2.49)$$

For turbulent flows with $2300 < Re < 10^7$ the equation by Konakov, which applies to both single-phase liquid and single-phase vapor flows, can be used [24]:

$$\xi = \frac{1}{(1.8 \cdot \log(Re) - 1.5)^2} \quad (2.50)$$

2.5.2. Pressure Loss for Condensation

The pressure loss during condensation in horizontal tubes is calculated with the Correlation of Friedel [13] [12]. With this method, the pressure loss of the pure liquid flow Δp_l is first determined using the correlation of Konakov (Eq.2.50) or Hagen-Poiseuille (Eq.2.49) presented before. Then the total pressure drop Δp is determined by multiplying Δp_l by a two-phase multiplier Φ_{Lo}^2 which takes into account the distribution of liquid and gas phase:

$$\Delta p = \Phi_{Lo}^2 \Delta p_l \quad (2.51)$$

The two-phase multiplier Φ_{Lo}^2 is calculated as:

$$\Phi_{Lo}^2 = D + 3.43x^{0.685}(1-x)^{0.24} \left(\frac{\rho_l}{\rho_g}\right)^{0.8} \left(\frac{\eta_g}{\eta_l}\right)^{0.22} \left(1 - \frac{\eta_g}{\eta_l}\right)^{0.89} Fr_l^{-0.047} We^{-0.0334} \quad (2.52)$$

where x is the steam quality, Fr_l the Froude number of the liquid phase and We the Weber number. The definition of Froude number and Weber number are explained below. The factor D is calculated as:

$$D = (1-x)^2 + x^2 \left(\frac{\rho_l \xi_g}{\rho_g \xi_l}\right) \quad (2.53)$$

The subscripts l and g refer to the liquid and gas phase. The pressure loss factors ξ_l and ξ_g are calculated depending on the Reynolds number. For $Re < 1055$ it is calculated with the Hagen-Poiseuille relation:

$$\xi_{l,g} = \frac{64}{Re_{l,g}} \quad (2.54)$$

For $Re > 1055$ it is:

$$\xi_{l,g} = \left[0.86859 \cdot \ln \left(\frac{Re_{l,g}}{1.964 \cdot \ln(Re_{l,g}) - 3.8215} \right) \right]^{-2} \quad (2.55)$$

The Reynolds numbers have to be calculated only for the liquid and vapor content and are therefore dependent on the steam quality.

The Froude number represents a measure of the ratio of inertial forces to gravitational forces within a hydrodynamic system. The Froude number for the liquid phase can be calculated as follows [23]:

$$Fr_l = \frac{w_l^2}{gd} \quad (2.56)$$

The Weber number represents the ratio of inertial force to surface tension and is calculated as [23]:

$$We = \frac{w_l^2 d \rho_l}{\sigma_l} \quad (2.57)$$

where σ_l is the surface tension of the fluid.

2.5.3. Air-side Pressure Loss

The pressure loss coefficient on the air-side of the fin and tube heat exchanger is calculated with a correlation of Haaf [49] that is already implemented in TIL:

$$\xi_{air} = 10.5 \cdot Re^{\frac{1}{3}} \left(\frac{d_{ae}}{d_s} \right)^{0.6} \quad (2.58)$$

The form factor a of Equation 2.47 is calculated using the serial tube distance d_s and the equivalent diameter d_{ae} that was introduced in Chapter 2.4.3 in Equation 2.36:

$$a = \frac{d_s}{d_{ae}} \quad (2.59)$$

2.6. Dynamic Simulation

For the dynamic simulation the modeling language *Modelica* with the simulation environment *Dymola* is used. In addition, thermodynamic models from the commercial component library *TIL* are utilized. Further, for the fluid property calculation during the simulation the database *REFPROP* of the National Institute of Standards and Technology is used. The programs mentioned are explained in the following.

2.6.1. Modelica, Dymola

Modelica

Modelica is an open-source, object-oriented modeling language for system-level modeling that was first introduced in the late 1990s by the Modelica Association [35]. Multiple physical domains are supported, among which are mechanical, electrical, thermal, and fluid systems, which enables the modeling of complex, reusable and easy to modify multi-domain systems.

Models are describes by differential, algebraic or discrete equations [63]. A special feature in Modelica is that equations don't need to be solved manually for particular variables. This enables the use of equations in its textbook form. Modelica later solves these equations for the unknown variables. This enables an easy reuse of sub-models for different purposes and therefore facilitates the handling of complex systems.

The modeling approach in Modelica is based on the procedure that is used when building a real system where complex new system can be assembled from existing components. Existing models of the most frequently used components are included in the Modelica Standard Library [35]. Furthermore, free and commercial libraries are available for various areas of application, such as the commercial TIL-library (see section 2.6.2) for thermodynamic components. If no components for a special function are available, own components can be developed or existing ones modified.

To simulate a Modelica model an simulation environment is required that converts the code into a form suitable for simulation [35]. In this thesis the tool Dymola is used for this purpose that reads the model and translates it into a set of mathematical equations.

Dymola

Dymola (**D**ynamic **M**odeling **L**aboratory) is an commercial modeling and simulation environment for developing models in the Modelica language [4]. It comes with a graphical model editor that allows the definition of Modelica models by positioning existing models of individual system components in the editor window. The individual component models can then be connected by drawing connections in form of lines which specify interactions between the components [35].

This allows the navigation of large and complex models. The corresponding Modelica code is automatically generated by the program. Alternatively, a model can be created by manually entering text in the text-editor window [35].

Dymola can convert large models into C code. A special transformation algorithm converts the individual equations of the model components in Modelica into a system of equations. At the same time, the equations are converted into an explicit form, sorted and, if possible, variables are substituted [14]. This system of equations can now be solved using conventional methods. By default the DASSL algorithm is set as an solver to integrate the system. Besides a simulation engine Dymola also provides an result viewer.

DASSL

As mentioned before, DASSL (Differential-Algebraic System Solver) is the default solver in Dymola. It is an implicit, higher order, multi-step solver with a step-size control for the numerical solution of implicit systems of differential/algebraic equations of the form $F(t, y, y') = 0$ [36]. It was developed in the 1980s and is explained in detail in Petzold82 [36].

The solver applies backward differentiation (BDF), which is an implicit method for numerical integration [34]. The time step size is variably adjusted by the solver so that the desired accuracy of the results is achieved [63]. As all in Dymola available integration algorithms DASSL approximates the solution by a polynomial of order k . It then automatically adjusts the polynomial order during the simulation between $1 \leq k \leq 5$ [7].

Further, DASSL is an *dense output algorithm* which is explained in the Dymola User Manual Vol 1 [7] as:

The step size of such integrators is not influenced by the communication grid. The step size is only chosen according to the required tolerances and the estimated local error. Such algorithms integrate past the desired communication points and determine the values of the state variables x at the communication points by interpolation, which involves no evaluation of the differential equation. Dense output implies that the algorithm can handle state events efficiently and also produce evenly spaced output.

2.6.2. TIL

In addition to elements from the Modelica standard library, the commercial TIL component library in version 3.12.1 is used to model the MoNiKa cycle. Besides component models the TIL suit also includes TIL-Media, which is an interface via which external substance data from the REFPROP program of the National Institute of Standards and Technology

(NIST) can be accessed. By this means TIL-Media enables the calculation of thermo-physical properties of incompressible liquids, ideal gases as well as real fluids containing a vapor liquid equilibrium (VLE-fluids). Furthermore, it allows the property calculation of fluid mixtures [59].

2.6.2.1. General Principles of TIL

System Information Manager

In every model that contains components of the TIL library, a *System Information Manager* (SIM) model is required. In this model the working fluids are defined. For each additional component in the model, it must then be selected which of the SIM fluids is to be used. Figure 2.12 at the end of the chapter shows the use of the introduced models and components based on a MoNiKa example model.

Cells

Components of the TIL library have a modular structure. Cells are the smallest unit for the construction of models. The cells use a finite-volume-based approach where each volume has one temperature and pressure. For components of this thesis, *VLE-Fluid Cells*, *Wall Cells* and *Moist-Air Cells* were used, which are briefly explained below.

VLE-Fluid Cells as depicted in Figure 2.8 on the left, map a flow of a compressible two-phase, vapor or liquid fluid flow and covers substances and mixtures. The Cell model contains a replaceable pressure drop model (green cycle in the figure). This model provides different correlations for the calculation of the pressure drop, regarding the geometry information and the substance properties. If no suitable pressure drop model is available in TIL, an own model can be created which the cell then accesses. Furthermore, the cell contains a heat transfer model (red cycle) where the convective heat transfer of the VLE-Fluid flow is calculated. The model provides a heat transfer coefficient α . Likewise to the pressure drop model, predefined correlations are provided and user-defined correlations can be implemented. Further, the cell contains a *VLE-Fluid-Object* (green circle) to calculate the thermo-physical substance properties of the compressible two-phase, vapor or liquid fluid based on pressure and enthalpy. Moreover, each VLE-Fluid Cell contains two VLE-Fluid Ports that are connected to the ports of the neighboring cell or element to specify the interactions (pressure, mass flow, enthalpy flow and mass fraction of steam) between the two neighboring elements. The VLE-Fluid Cell further contains a heat port which enables the consideration of a heat flow rate from or to the outside. In addition each cell contains the balance equations for mass, energy and momentum as explained in Chapter 2.6.2.2.

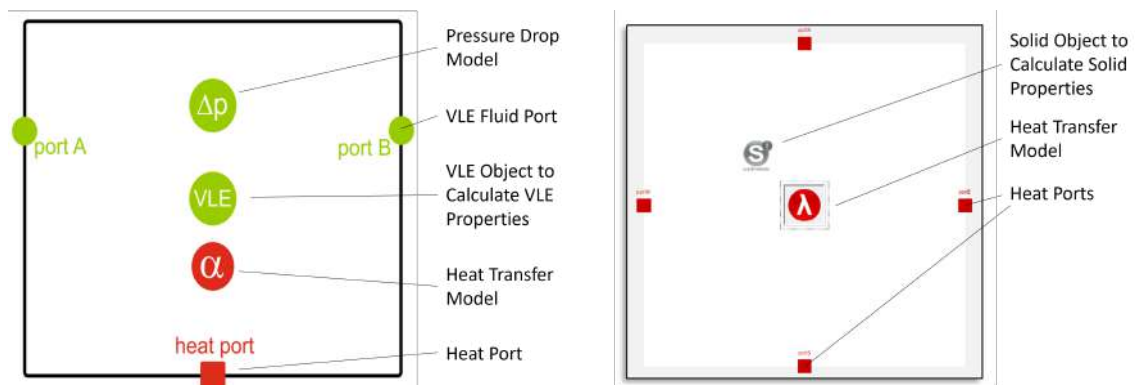


Figure 2.8.: Structure of VLE-Fluid Cells (left) and Wall Cells (right) in TIL. (pictures from the TIL documentation [59])

Wall Cells as depicted in Figure 2.8 on the right, use the properties of a solid medium (grey circle in figure) and geometry data, given from the outside, in order to calculate

the thermal capacity of the cell. The model contains four heat ports and uses a transient energy balance, considering the heat capacity of the material. A heat conductance to the ports is calculated using either a fixed heat resistance or a geometry and material based heat resistance model (red cycle in figure).

Moist-Air Cells can be considered as a combination of Gas-Cell and Wall Cell. It maps an ideal moist air flow, as well as the thermal capacity of a solid mass. The structure of the cell is depicted in Figure 2.9. The Moist-Air Cell enhances the gas cell model by considering condensation and evaporation of water, using a dynamic mass and energy balance of a water film. Furthermore, ice formation can be considered. As does the VLE-Fluid Cell, the Moist-Air Cell contains a replaceable heat transfer and pressure drop model as well as the balance equations explained in the next section. Further, the effect of non-isothermal fins are considered by a replaceable fin efficiency model.

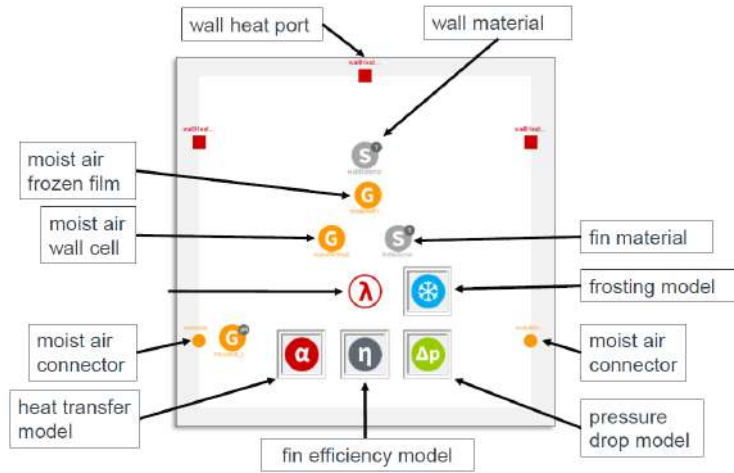


Figure 2.9.: Structure of Moist Air Cells in TIL. (pictures from the TIL documentation [59])

2.6.2.2. Balance Equations in TIL

The component models used in TIL include the conservation equations for mass, energy and momentum in the following notation [39][63]:

Energy balance:

$$\frac{dh}{dt} = \frac{1}{M} \left(\sum_i (\dot{m}_i (h_i - h)) + \dot{Q} + \dot{W}_t + V \frac{dp}{dt} \right) \quad (2.60)$$

Momentum balance:

$$\frac{d\dot{m} V}{dt A} = \frac{\dot{m}_{in}^2}{A\rho_{hom}} - \frac{\dot{m}_{out}^2}{A\rho_{hom}} + (p_{in} - p_{out})A - \Delta p_R A - \rho_{hom} g V \sin \varphi \quad (2.61)$$

Mass balance:

$$\frac{dM}{dt} = \sum_i \dot{m}_i = \rho_{hom} \frac{dV}{dt} + V \frac{d\rho_{hom}}{dt} \quad (2.62)$$

where the change in density over time in Equation 2.62 is calculated depending on pressure and enthalpy in the constant control volume V with:

$$\frac{d\rho}{dt} = \left(\frac{\partial \rho}{\partial p} \right)_h \frac{dp}{dt} + \left(\frac{\partial \rho}{\partial h} \right)_p \frac{dh}{dt} \quad (2.63)$$

The partial derivatives of this equation are calculated in TIL using the respective material data model.

In the above equations the three-dimensional flow is considered as one-dimensional and thus only the given, dominating flow direction is considered. Furthermore, the flow is considered to be a homogeneous single-phase flow, hence the subscript *hom*. The numerator *i* in the summation sign includes all incoming and outgoing material and energy flows of the control volume *V*. The energy balance 2.60, which is based on the first law of thermodynamics for open systems, neglects the kinetic and potential energy and also assumes constant fluid properties in the control volume. In the energy balance h_i denotes the enthalpy of the mass flow transported across the system boundaries and h denotes the enthalpy inside the control volume. \dot{Q} is the heat flow transferred across the system boundaries and \dot{W}_t is the work done by the system on its surroundings. In the momentum balance 2.61 A designates the flow area of the control system sides and ρ_{hom} the homogeneous density of the fluid.

Neglecting fast dynamic processes such as the propagation of sound waves, the time derivative in the momentum balance becomes zero, resulting in a stationary momentum balance.

The hydrostatic influences $\rho_{hom}gV \sin \varphi$ are not taken into account in the momentum balance neither in the turbine nor in the condenser model due to the small differences in height.

Pressure State Element

The pressure derivative $\frac{dp}{dt}$ appears in the energy balance 2.60 as well as in Equation 2.63 for the density derivative for the mass balance. This leads to a coupled non-linear system that is difficult to solve.

To reduce the dimension of the coupled energy and mass balance TIL introduces a numerical approach called *Pressure State Approximation*. Instead of calculating $\frac{dp}{dt}$ for each element/cell the pressure derivative is calculated as a global variable in the so called *Pressure State Element*, leading to the decoupling of the equations and hence avoids a non-linear system. This approach increases the time constants of the model and therefore improves simulation performance [59].

In a physical system the pressure change propagates with the speed of sound, which can lead to oscillations or standing waves. By using the Pressure State Approximation pressure changes are propagated instantaneously since the derivative for all elements of this pressure level is the same. Therefore, this approach leads to errors when the effect of oscillations and standing waves is of importance.

For the modeling with TIL a Pressure State Element for each pressure level must be used (e.g. pressure level 1: between heat exchanger and turbine; pressure level 2: between turbine and condenser). It is important to note that the derivative of the pressure is not constant over time, and the pressure itself is not constant along the flow direction, hence each cell still has its own pressure but the term $\frac{dp}{dt}$ is the same in all energy and mass balances for each pressure level.

2.6.2.3. Turbine Model in TIL

In the TIL library the turbine model *EffExpander* is available. This is a zero-dimensional component model in which the expansion of the steam is calculated as a function of the intake volume ΔV , the rotational speed n and the constant isentropic efficiency η_{is} . The turbine shaft power P_T then results from the energy balance of the turbine:

$$P_T = \dot{m} \cdot (h_{Out,is} - h_{In}) \cdot \eta_{is} = \dot{m} \cdot (h_{4,is} - h_{3'}) \cdot \eta_{is} \quad (2.64)$$

With a given turbine back pressure and mass flow, the density at the turbine inlet ρ_3 is obtained using the following equation:

$$\dot{m} = \rho_3 \cdot n \cdot \Delta V \quad (2.65)$$

Afterwards the remaining fluid properties (e.g. inlet pressure) can be calculated using equations of state since now two properties (ρ and h) are known at the turbine inlet. In the real MoNiKa plant, however, the relationship between mass flow, pressure levels and inlet temperature is better described by the corrected Stodola Equation 2.9 as explained in Chapter 2.3.2.3. Equation 2.65 must therefore be replaced with the empirically corrected Stodola Equation 2.9. In addition, the isentropic turbine efficiency is not constant in real operation, especially during partial load, which is why the empirically determined correlation for the isentropic turbine efficiency (Equation 2.7) must also be incorporated in the model.

2.6.2.4. Condenser Model in TIL

The TIL library provides a variety of heat exchanger models for different geometries and medium combinations. To model the MoNiKa Condenser the *FinAndTube - MoistAir VLE-Fluid - ParallelFlowHX* model is used. As the name already suggests, this is a fin and tube heat exchanger that uses a VLE-Fluid on the ORC side and Moist Air on the air side.

The MoNiKa heat exchangers can be modeled as a cross-flow or parallel-flow design. The more tubes the heat exchanger has connected in series in the direction of the cooling air flow, the more the parallel-flow characteristic predominates since then the temperature difference between each of the serial tubes is greater than the difference between the beginning and end of a single tube. For more than 3 serial tubes an implementation as parallel flow heat exchanger is recommended by the TIL support. For the heat exchangers in the MoNiKa condenser, with 4 serial tubes and 69 parallel tube coils the condenser model will therefore be implemented as a parallel-flow design.

The TIL condenser model is constructed from VLE-Fluid Cells and Moist-Air Cells. As mentioned before, the Wall Cells are already included in the Moist-Air Cell model. The structure of the model is shown schematically in Figure 2.10. For VLE-Fluid Cells and Moist-Air Cells in the condenser a heat transfer and pressure drop model can be selected. The fin efficiency model is contained in the Moist-Air cells. The model further contains parameters for the geometry which has to be given by the user. The condenser is discretized one-dimensionally in n cells in flow direction, leading to n VLE-Fluid cells and Moist-Air cells (and therefore also Wall Cells). An adequate number of cells must be determined by the user. The connection of the cells is shown in Figure 2.11.

2.6.2.5. Exemplary Model with Components from TIL

Figure 2.12 shows an example of how the components of the TIL library presented in the previous chapters are used and connected.

The most important components used are:

- 1: System Information Manager
- 2: Pressure State Element
- 3: Turbine Model
- 4: Hydraulic Resistance Model
- 5: Condenser Model
- 6: Connections
- 7: Model containing input data for a specific Simulation

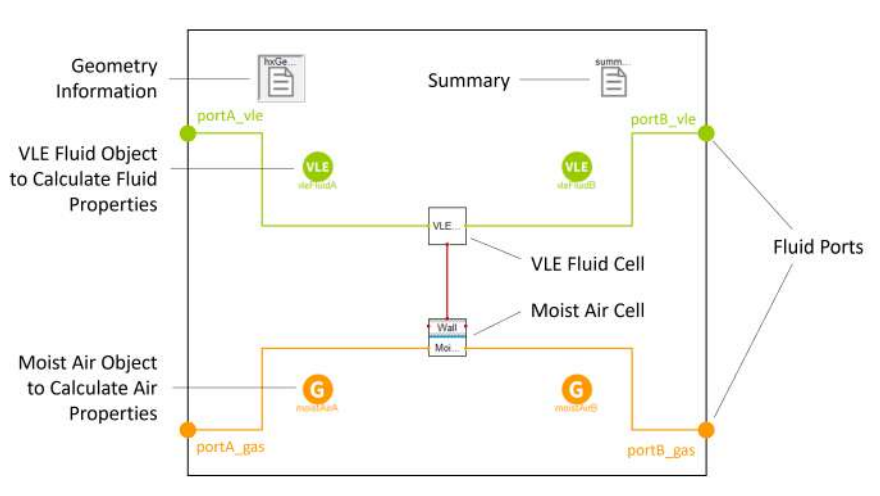


Figure 2.10.: Structure of the TIL parallel flow heat exchanger model for Moist-Air and VLE-Fluid. (picture from the TIL documentation [59])

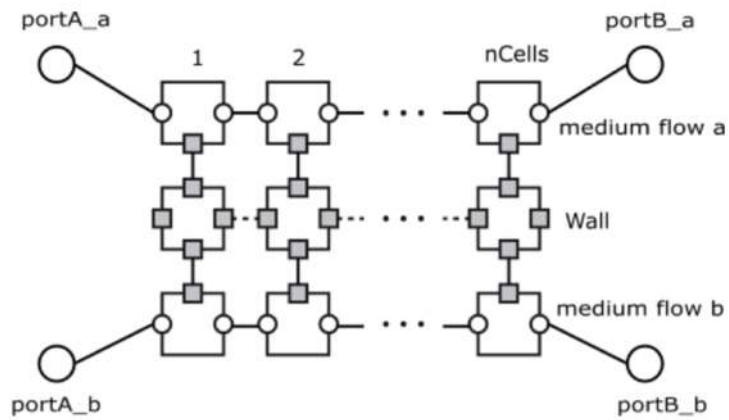


Figure 2.11.: Cell connection of parallel flow heat exchanger models in TIL. (picture from the TIL documentation [59])

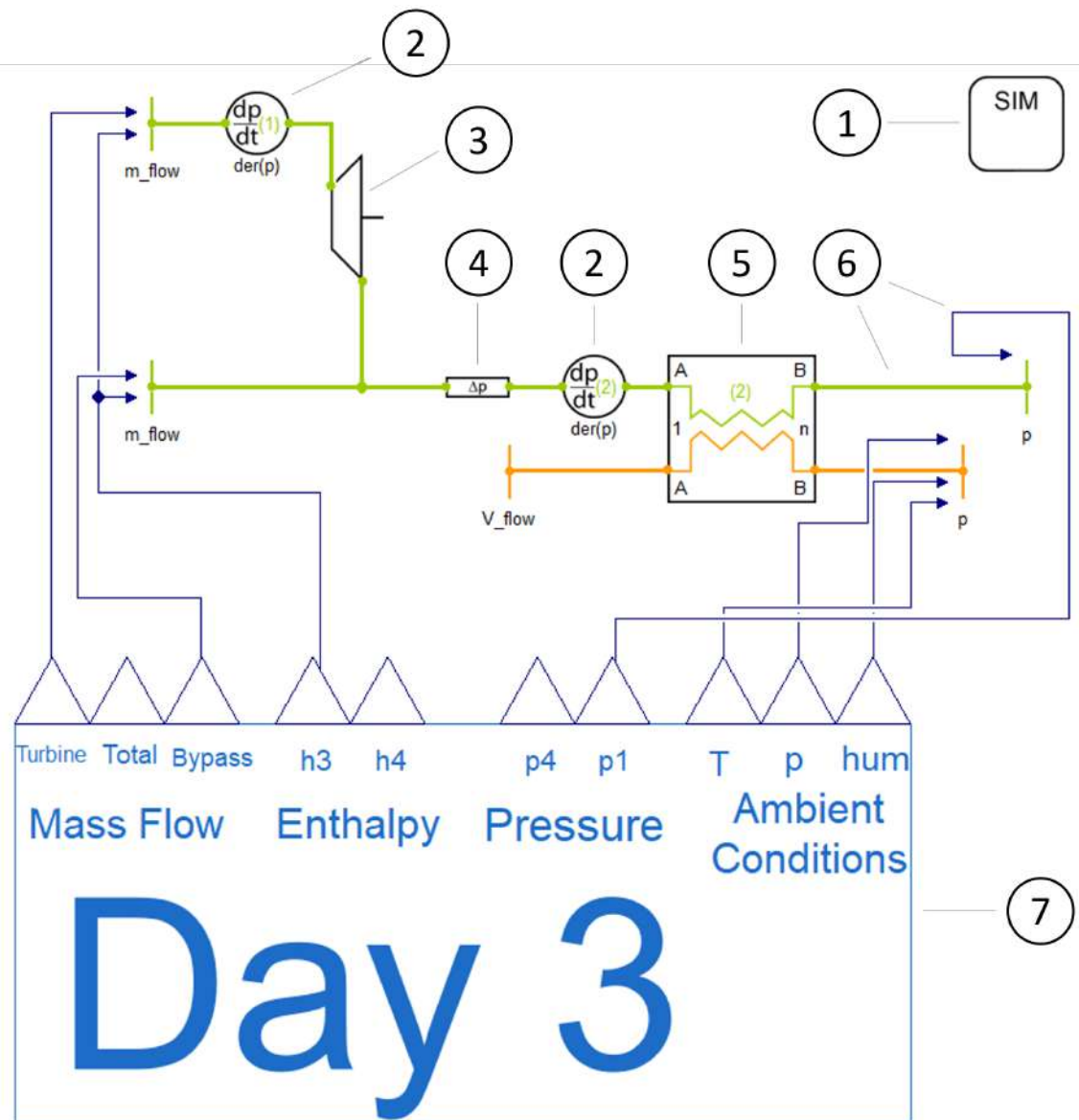


Figure 2.12.: Exemplary Dymola model with components from TIL using the example of the model *S_d3_N1_65* as explained in Chapter 3.5. The most important components are marked with numbers.

2.6.3. REFPROP

REFPROP is a program, developed by the National Institute of Standards and Technology (NIST), that calculates thermodynamic and transport properties of industrially important fluids and their mixtures [27]. The acronym stands for **R**eference fluid **P**roperties. Detailed information about the pure fluid and mixture models in REFPROP are available at [27].

It is important to note that some mixtures have components with a wide range of volatilities (i.e. large differences in boiling points), as indicated by a critical temperature ratio greater than 2, which can lead to numerical problems in some property calculations [27]. Propane has a critical temperature of 369.85K [10] and Nitrogen of 126.19K [47] which leads to the mentioned problems. During the elaboration of the thesis, it became apparent that for the propane-nitrogen mixture, especially for fluid states around the critical point, the REFPROP material model does not always converge which can lead to simulation crashes.

3. Model Development

The modeling process that led to the final Dymola model is explained in this chapter. Furthermore, the experimental comparison data from various MoNiKa test runs and the methods used for the quantification of the agreement of the results are presented.

3.1. Introduction of the Experimental Data from Test Runs

The measurement data from four MoNiKa test runs are relevant for this thesis. The designation of the test runs as Day0, Day1, Day2 and Day3 is oriented on the previous theses. Table 3.1 gives an overview of the MoNiKa test runs with the control parameters that were varied during operation.

The start time of recording of the measurement data was 5:49:00 for Day0, 12:00:00, for Day1 and Day2, and 13:11:00 for Day3. These start times were selected in the previous theses [11][28] and were adopted. For Day1-3 the actual start-up of the system begins earlier. Therefore the data of Day1-3 do not include the start-up of the plant, but begin shortly before the start of turbine operation. The mentioned start times are the first time step of the Dymola models for the respective day.

At the time of the test run of Day0, no turbine was installed in the MoNiKa plant. The expansion of the propane therefore took place through a throttle valve. Consequently, the test run from Day0 is a pure propane cycle, while for Day1-Day3 a propane-nitrogen mixture as the working fluid must be assumed due to nitrogen infiltration in the turbine shaft seal. As explained in Chapter 2.3.2, the used nitrogen content is based on calculations by Prof. Dr. Thomas Schulenberg and estimated at 1.65 mass%.

For all test runs the condenser fans were operated at full load and no water injection on the heat exchanger fins took place.

The most important comparison variable of the turbine model is the turbine shaft power P_T , which can be determined from the measured generator power according to Equation 2.3. For the condenser model, the enthalpy at its outlet h_1 serves as the main comparison variable. Alternatively, the temperature at the outlet T_1 could be used, but this is less advantageous since most of the state change in the condenser takes place in the two-phase region. The condenser outlet enthalpy for the test runs can be determined from the measured temperature and pressure data using a Matlab-REFPROP interface.

Both the turbine model and the condenser model require a stream variable as an input. In the case of the turbine, this can be the enthalpy or temperature at the turbine inlet.

DATE OF TEST RUN	DESCRIPTION OF TEST RUN	DESIGNATION IN THESIS
07 Feb.2020	24h condenser test run with 100%, 70% and 50% of design mass flow in stationary operation. Pure propane ORC since no nitrogen-sealed turbine was installed at this time.	Day0
08 Nov.2021	Turbine and condenser test run for stationary operation in 7 different operating points. Adjustment of ORC mass flow, mass flow of thermal water and control valve position to reach operating points. The operating time was about 4 hours.	Day1
09 Nov.2021	Turbine and condenser test run with gradual opening of the control valve and variation of ORC mass flow at constant mass flow for thermal water. The operating time was about 4 hours.	Day2
10 Nov.2021	Turbine and condenser test run with gradual increase of ORC mass flow from $2.1 \frac{kg}{s}$ to $2.8 \frac{kg}{s}$ in steps of $0.1 \frac{kg}{s}$. No variation of control valve (fully opened) or mass flow of thermal water. However, in this test run control problems in the boiler occurred leading to fluctuations of turbine inlet temperature and enthalpy. The average thermal water temperature in the boiler for this day was $151.6^{\circ}C$ with a standard deviation of 1.49%. The operating time was about 4 hours.	Day3

Table 3.1.: Overview and designation of the relevant MoNiKa test runs

In the case of the condenser, whose incoming flow is in the two-phase region, enthalpy or vapor quality can be used. To enable a more structured and automated procedure, it was decided in both cases to use the enthalpy as an input variable. The calculation of the enthalpies from the measurement data for temperature and pressure was carried out in Matlab. The results were then imported into Dymola.

The fluid property calculation, especially in the vicinity of the critical point and for mixtures, is not unproblematic, which is why the procedure for calculating the inlet enthalpies of the turbine and condenser model is explained in the following section.

3.1.1. Calculation of Inlet Enthalpy for Turbine and Condenser

Day0

At the time of Day0, no turbine was installed in the MoNiKa system. The supercritical propane was expanded via a throttle valve which is assumed to be isenthalpic in the following. Since the fluid is expanded into the two-phase region, it is not possible to calculate the enthalpy $h_{4'}$ directly from the measured pressure and temperature data at the condenser inlet. Instead, the enthalpy at the heat exchanger outlet h_3 is determined. Assuming isenthalpic throttling, negligible changes in kinetic and potential energies and negligible heat losses in the pipes [11], the energy balance yields: $h_{4'} = h_3$. The enthalpy at the heat exchanger outlet h_3 is then determined as a function of the measured temperature T_3 and the measured pressure p_3 for pure propane.

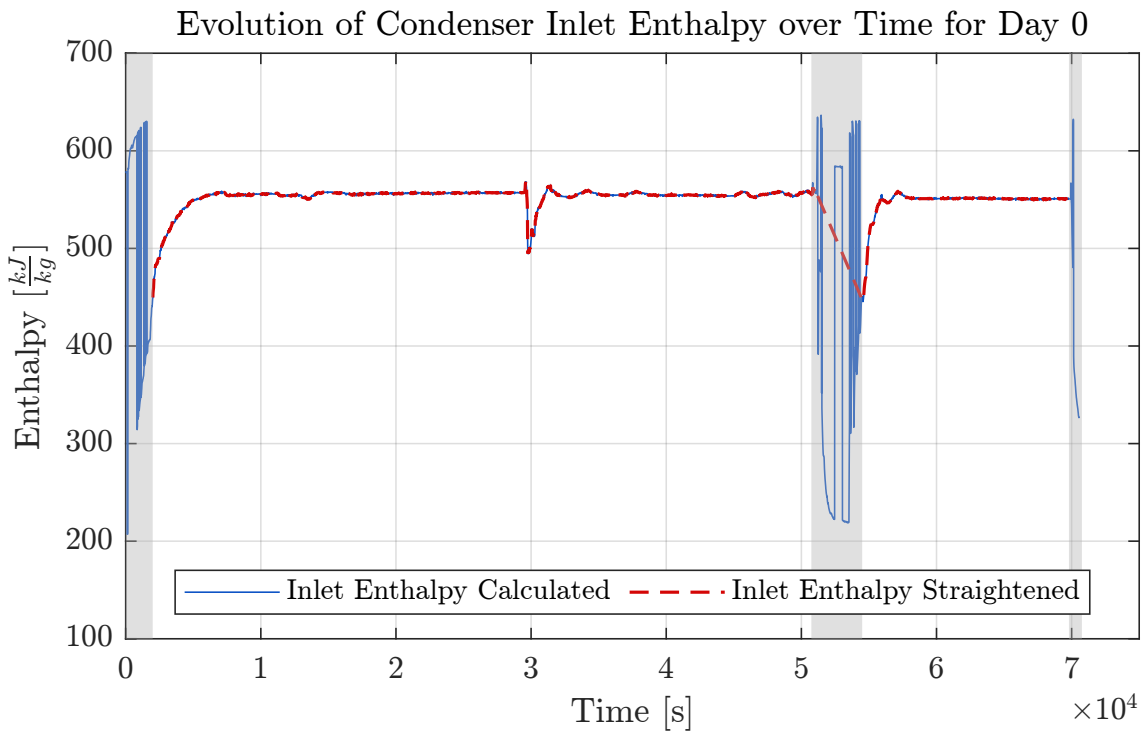


Figure 3.1.: Enthalpy calculation for condenser inlet for Day0. The blue line represents the results of the enthalpy calculation from pressure and temperature at the heat exchanger outlet. The red line shows the modified enthalpy that was finally used as input for the Dymola models.

The result is shown in Figure 3.1 as a blue line. As can be seen immediately, there are three time ranges in which the enthalpy calculation led to problems. These areas have been highlighted in gray.

In the first time range marked in gray ($0s < t < 2000s$), the system is started up, in the last range ($t > 70000s$) the system is shut down. In the second range ($50740s < t < 54500$), the mass flow is reduced from 70% to 50% of the maximum mass flow. For all three ranges the fluid variables at the heat exchanger outlet fall below critical conditions and therefore pass through the two-phase region. In this area, no clear enthalpy determination from the pressure and temperature measurements is possible, which is why the calculated value jumps between the enthalpy of liquid and gaseous propane. As soon as a supercritical state is reached, the problem disappears.

At $t \approx 30000s$ the mass flow is reduced as planned from 100% to 70% of the maximum mass flow. There are no problems with the calculation here. However, for the second mass flow transition ($50740s < t < 54500$) a control problem arose so that the mass flow and thus the pressure and temperature at the heat exchanger outlet fluctuated over a long period of time. As a result, the fluid states are alternately in the supercritical and two-phase region.

Due to the above difficulties, the directly calculated enthalpy cannot be used for the simulation without further processing, since the heavily fluctuating enthalpy values will lead to the simulation crashing. However, in order to enable an uninterrupted simulation over the entire duration of Day0, the start-up and shut-down time range was cut off and the enthalpy in the time range of the second mass flow transition was linearly interpolated from the boundary values of this area. The condenser inlet enthalpy used as input to the simulation model is shown as a red dashed line in Figure 3.1.

Day1-3

For an easier understanding of the procedure, the MoNiKa system plan between the heat exchanger and condenser with the designation of the fluid states is shown in Figure 3.2. As can be seen in the enthalpy calculation for Day0, this is difficult whenever the fluid states are close to the boundaries of the two-phase region. When calculating the fluids properties using fluid mixtures, the additional difficulty arises that the calculation of properties with REFPROP often does not converge for fluid states close to the critical point. For this reason, the enthalpy calculation is carried out based on the measurement data at the heat exchanger outlet (state 3) instead of the turbine inlet (state 3''). On this basis, the input enthalpies for the turbine and condenser can be determined as follows:

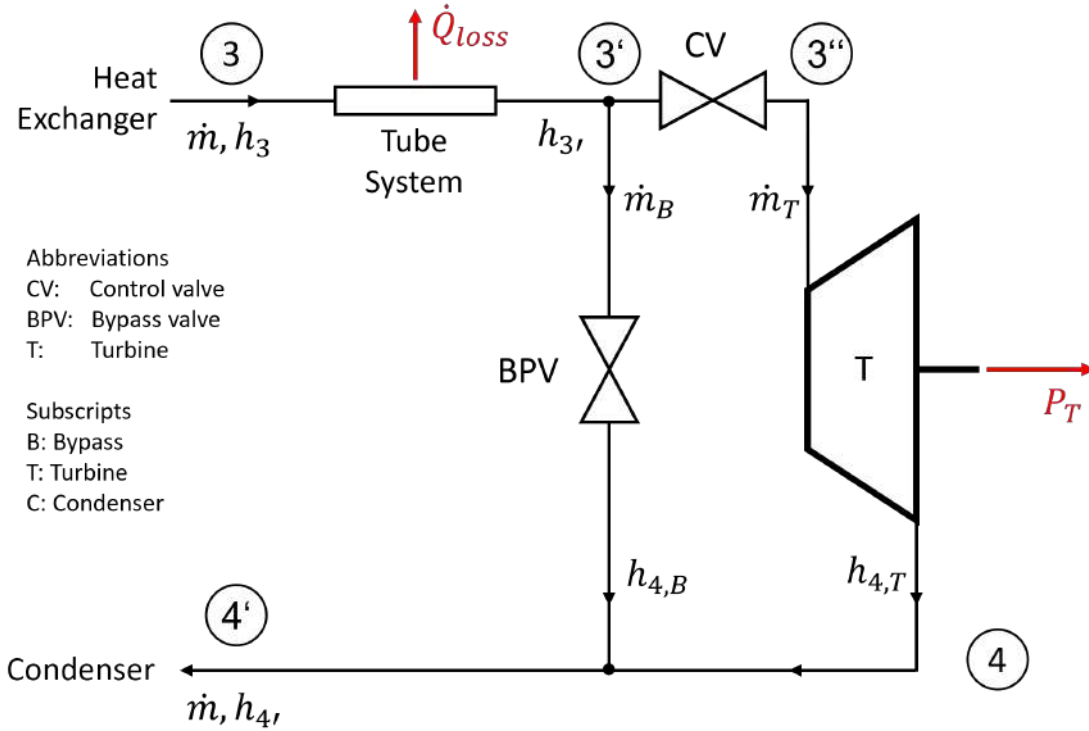


Figure 3.2.: Block diagram to illustrate the calculation of the input enthalpy for turbine and condenser

If one applies the first law of thermodynamics to the tube system, which connects the heat exchanger (state 3) with the bypass junction (state 3'), and neglects the kinetic and potential energies, and further assumes stationary behavior, one obtains the enthalpy at node 3' as:

$$h_{3'} = h_3 - \frac{\dot{Q}_{loss}}{\dot{m}} \quad (3.1)$$

It is assumed that the entire heat loss takes place in the relatively long pipes between the heat exchanger and the junction for the bypass. The heat loss occurring in the pipes was estimated by Joaquín Perez [28] to be $\approx 330W$ and is relatively constant during the test runs. It is then assumed for simplification that no further heat loss takes place after node 3'. Since the change of state in the control valve is assumed to be isenthalpic and no further heat loss is taken into account, the inlet enthalpy of the turbine corresponds to:

$$h_{3''} = h_{3'} \quad (3.2)$$

Using Equation 3.1, it then follows for the inlet enthalpy of the turbine:

$$h_{3''} = h_3 - \frac{\dot{Q}_{loss}}{\dot{m}} \quad (3.3)$$

To determine the inlet enthalpy of the condenser, the first law of thermodynamics can be applied to a control volume of the entire system shown in Figure 3.2 (state 3 to state 4'):

$$-\dot{Q}_{loss} - P_T + \dot{m} \cdot h_3 - \dot{m} \cdot h_{4'} = 0 \quad (3.4)$$

In the above equation, the changes in kinetic and potential energies have been neglected and steady-state behavior has been assumed. In addition, it was assumed that only the working flow of the turbine shaft power and the heat flow of the heat losses in the pipe system between 3 and 3' are transferred across the system boundaries. After rearranging the equation, the inlet enthalpy of the condenser is:

$$h_{4'} = h_3 - \frac{\dot{Q}_{loss}}{\dot{m}} - \frac{P_T}{\dot{m}} \quad (3.5)$$

With the equations presented, it is now possible to determine the input enthalpies for condenser and turbine from the measured values for pressure and temperature at the heat exchanger outlet. Here it must be noted that the calculation, unlike for Day0, is not carried out with pure propane but with a propane-nitrogen mixture.

3.2. Methods for the Quantification of the Agreement of Results

In this thesis, a quantification of the agreement of simulation results with experimental data will be carried out by executing the following procedure:

1. First, the experimental data and simulation results are interpolated to a uniform time vector. The new time vector is determined from the start and end times (t_1 and t_n) of the time period to be compared and has a time step size $\Delta t = 1s$. This corresponds to the sampling rate of the measuring devices. Choosing a time vector with smaller time steps therefore does not lead to an improvement in accuracy. The number of time steps n is then determined as:

$$n = \frac{t_n - t_1}{\Delta t} \quad (3.6)$$

2. The absolute deviation of the results is then calculated for each time step i in the following way:

$$\varepsilon_{abs,i} = \psi_{Sim.,i} - \psi_{Exp.,i} \quad \text{for } i = 1, \dots, n \quad (3.7)$$

In addition, the relative deviation is calculated for each time step as well:

$$\varepsilon_{rel,i} = \frac{\psi_{Sim.,i} - \psi_{Exp.,i}}{\psi_{Exp.,i}} \quad \text{for } i = 1, \dots, n \quad (3.8)$$

where ψ is any variable.

3. Finally, the mean of the absolute and relative deviation is calculated. The sign of the deviations is considered to be always positive using the absolute value function:

$$\bar{\varepsilon}_{abs} = \frac{1}{n} \sum_{i=1}^n |\varepsilon_{abs,i}| \quad (3.9)$$

$$\bar{\varepsilon}_{rel} = \frac{1}{n} \sum_{i=1}^n |\varepsilon_{rel,i}| \quad (3.10)$$

The introduced metrics enable an evaluation of the agreement of the simulation results. $\bar{\varepsilon}_{rel}$ and $\bar{\varepsilon}_{abs}$ can be used as a metric to evaluate the agreement of results for an entire day while $\varepsilon_{rel,i}$ and $\varepsilon_{abs,i}$ give a more detailed evolution of the agreement over time. The code of the Matlab-Function used for the calculation is attached in the Appendix B.1.

3.3. Development of the Turbine Model

3.3.1. Implementation of the Turbine Model and Comparison with the Simulink Turbine Model by Julia Filipe

The TIL *EffExpander* component as introduced in Chapter 2.6.2.3 serves as the basis for the turbine model. The correlation for the isentropic turbine efficiency (Equation 2.7) and the modified Stodola correlation (Equation 2.9) by Joaquín Perez [28] were additionally implemented in the model.

The MoNiKa turbine model in Simulink that was developed by Julia Filipe [9] as part of her thesis serves as a comparison model. This was created on the basis of the MoNiKa test runs from Day1-3. At that time, a nitrogen content of 0.2 mass% was assumed.

To verify the correct implementation of the turbine model in Dymola, a simulation was carried out using the same inputs as Julia Filipe and the same propane-nitrogen mixture with 0.2% nitrogen. Both models should then deliver equal results except for numerical rounding differences.

However, the model could not be verified this way because two key observations were made:

Observation 1: Firstly, the temperature at the inlet of the turbine of the two models did not agree. This is remarkable because the inlet pressure calculated via the Stodola approach was the same and the enthalpy at the inlet was given as input. Since two state variables match, all other state variables should also match if the substance is the same. Since the input temperature is determined from the pressure and the enthalpy, it was initially assumed that there was an error in the substance data calculation, which takes place for both models via REFPROP. However, this hypothesis could be ruled out by a more detailed investigation. The most probable remaining conclusion is that the fluids used in the Dymola and Simulink model were not the same.

Observation 2: Secondly, the calculated turbine shaft powers of the two models did not agree, whereby the Simulink model of Julia Filipe represented the experimental data better. The deviation was significant and reached up to 10% of the turbine shaft power. This is also remarkable since the correlations used were identical. Therefore the calculated turbine efficiencies of both models agreed and the calculation of the turbine shaft power in the Dymola model was already implemented by TIL and can therefore be considered verified.

With the same inlet enthalpy, same efficiency, same inlet pressure and same outlet pressure, the shaft powers of the two models should match. If they do not (and this is the case here), there is an error in the implementation of one of the models or the fluids used were not the same.

Since a possible explanation for both observations is a deviating fluid mixture, the simulation was executed again with different nitrogen contents. This showed that observation 1 could be eliminated for pure propane and that the input temperatures of both models then correspond. However, the deviation of the shaft powers described in observation 2 could not be improved for any of the tested nitrogen contents (0%, 0.2%, 0.4%, 0.6%, 0.8%). Furthermore, both quantitative and qualitative deviations occurred for the shaft power.

A detailed analysis of Julia Filipe's Simulink model, suggested that the fluid properties were not calculated consistently and instead were sometimes calculated with pure propane and sometimes with a 0.2% nitrogen content in the propane. For a better understanding of the state points talked about, an exemplary turbine process is shown in Figure 3.3. The analyzed Simulink and Matlab codes from Julia Filipe suggest that in the Simulink model the state variables were calculated as summarized in Table 3.2. As can be seen from the table, almost all required state variables were calculated with pure propane. Only the enthalpy at the turbine outlet for the isentropic process was determined with the fluid mixture.

With the help of Table 3.2, the deviating turbine shaft powers explained in observation 2 can now also be explained: Since the enthalpy of state point 4_{is} was calculated with the fluid mixture and the enthalpy of $3''$ with pure propane, there is a difference in the enthalpy drop compared to the calculation with a consistent substance. Since the turbine power is determined from this enthalpy drop and the efficiency, the shaft powers of both models deviate significantly with a relative deviation that can be in the range of up to 10%.

Nevertheless, the Simulink model represents the experimental data better, since the fluid properties for the efficiency correlation worked out by Joaquín Perez were calculated in the same way (see Table 3.2).

Figure 3.4 shows the turbine efficiency calculated in Matlab for pure propane and the propane-nitrogen mixture on the example of Day2. In addition, the efficiency as calculated with the procedure of the previous theses is plotted. As can be seen, the described procedure with the inconsistent material data calculation results in an efficiency curve that neither corresponds to that of pure propane nor to that of the mixture, nor does it lie between the two. Instead, the curve is clearly shifted.

With the aim of achieving reasonable approximations of the turbine power in the Dymola model to be developed, two possible approaches result from these findings:

1st option:

To use the turbine efficiency correlation in its current form, the material data calculation in the Dymola model would have to take place in the same way as in the previous theses.

In TIL, however, the fluid to be used is defined separately in the *System Information Manager* (SIM). For each component (e.g. the turbine) it is then selected which of the defined fluids is to be used. Changing the fluid between turbine inlet and outlet is not foreseen in the available component models and it is unclear whether this can be implemented in TIL.

Another reason that speaks against this option is the problem that for state point 4_{is} the entropy calculation was carried out with pure propane and the enthalpy calculation with the fluid mixture. Since it is one and the same state point, the use of different substances

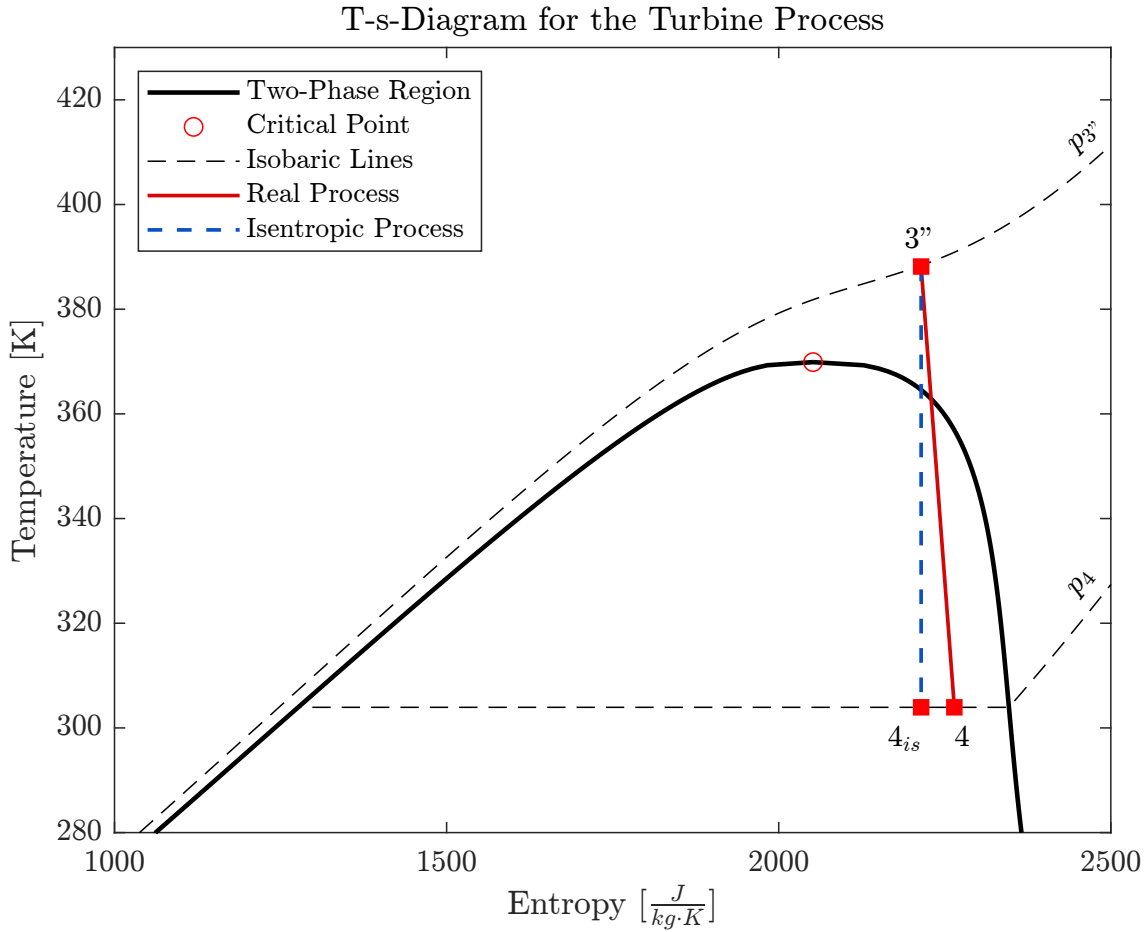


Figure 3.3.: T-s-Diagram for the change of state during the turbine process. The two-phase region was drawn for pure propane

CALCULATED PROPERTY	USED PROPERTIES	USED FLUID
The used inlet enthalpy $h_{3''}$ of the turbine is calculated on the basis of the outlet enthalpy of the heat exchanger h_3	$h_3 = f(T_3, p_3)$	Pure Propane
Temperature at turbine inlet $T_{3''}$	$T_{3''} = f(p_{3''}, h_{3''})$	Pure Propane
Entropy at turbine inlet $s_{3''}$	$s_{3''} = f(p_{3''}, h_{3''})$	Pure Propane
Entropy at turbine outlet for isentropic change of state $s_{4, is}$	$s_{4, is} = s_{3''} = f(p_{3''}, h_{3''})$	Pure Propane
Enthalpy at turbine outlet for isentropic change of state $h_{4, is}$	$h_{4, is} = f(s_{4, is}, p_4)$	Propane with 0.2% Nitrogen

Table 3.2.: Fluid property calculation in previous theses.

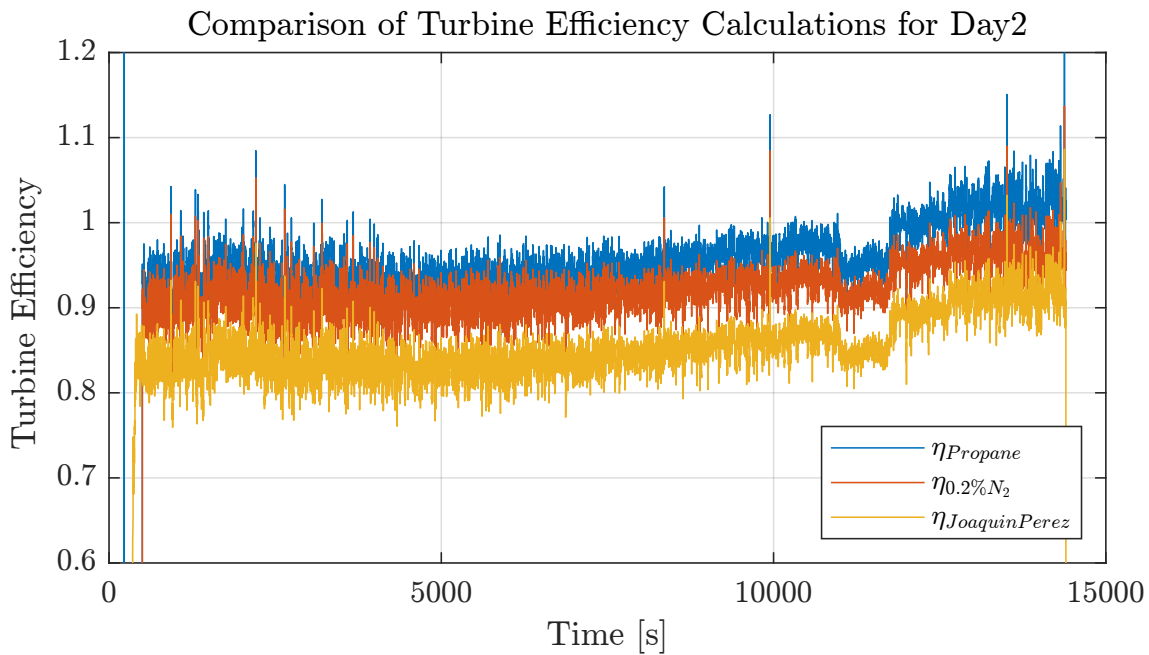


Figure 3.4.: Comparison of the calculated turbine efficiency for pure propane, a propane nitrogen mixture with 0.2% N_2 content and the current correlation as presented in the thesis of Joaquín Perez [28].

seems problematic here and it is unclear to what extent this will affect the quality of results in the later model when applied to a wide range of operating conditions.

2nd option:

The second possibility is to develop a new correlation for the turbine efficiency which is based on a consistent material data calculation. This procedure is physically more accurate. In addition, updated knowledge about the nitrogen content is now available and it is estimated that the nitrogen content at the time of the test runs was around 1.65 mass%. As can be seen in Figure 3.4 from the shift in the calculated efficiency line for pure propane (blue) and the mixture (orange), the nitrogen content has an influence on the calculated turbine efficiency, even if the calculation is carried out with consistent fluids.

Therefore, it was decided to develop a new efficiency correlation with consistent material data calculation and the latest knowledge about the nitrogen content. The procedure for developing the new correlation is presented in the following section.

Note: The fact that nitrogen is introduced as a sealing gas at the outlet of the turbine shaft is not a possible explanation for the procedure in the previous theses. In this case, the propane-nitrogen mixture produced at the turbine outlet would re-enter the turbine after passing through the ORC again. Therefore, a mixture would have to be assumed also at the turbine inlet. The nitrogen content was assumed to be constant during operation in both the current and previous final theses.

3.3.2. Development of a new Correlation for the Turbine Efficiency

Due to the findings presented in the previous section, a new correlation for the turbine efficiency is developed by carrying out the following steps:

First, a new turbine model was implemented in Dymola to calculate the turbine efficiency. Since Dymola offers the convenience of automatically rearranging equation systems based on the unknown variables, the existing turbine model can be used with some modifications to calculate the isentropic turbine efficiency without having to change the basic structure of the model. For this purpose, the shaft power of the turbine is defined as an additional

input and the efficiency correlation is removed. At the same time, the previously introduced Stodola equation is removed from the model and instead the pressure at the turbine inlet is directly specified as input. This eliminates the uncertainty of the inlet pressure calculation by the Stodola equation and thus leads to a more precise determination of the turbine efficiency.

The unknown variable then remains the turbine efficiency, which is calculated by Dymola for each time step. The for this purpose developed model *T_d1_N1_65_EfficiencyCalculation-FromShaftPower* is summarized in Table 3.3. The measurement data of the test run from Day1 serve as input. The output of the model is then the evolution of the turbine efficiency over time for Day1. The calculated efficiency using the data from Day1 has to be validated in later steps using the measurement data from Day2 and Day3.

MODEL	1. T_d1_N1_65_EfficiencyCalculationFromShaftPower 2. T_d1_N1_65_Overdetermined
INPUTS	1. \dot{m}_T ; p_4 ; $p_{3''}$; $h_{3''}$; P_T ; 2. \dot{m}_T ; p_4 ; $p_{3''}$; $h_{3''}$;
RELEVANT OUTPUTS	1. $\eta_{T,is}$ 2. P_T
CORRELATIONS	1. - 2. Turbine Efficiency Correlation
NOTE	1. The boundary conditions of the model are overdetermined because the mass flow and the pressures at the inlet and outlet are specified. In the later models, the input pressure is then determined using the Stodola equation and the output power by incorporating the new efficiency correlation. 2. First, the turbine model is implemented without the Stodola equation and with the inlet pressure as input. In later steps, the Stodola equation is supplemented to check whether the shaft power is then still well approximated.

Table 3.3.: Developed Dymola models for the development of a new correlation for the isentropic turbine efficiency for Day1.

In a next step a new correlation for the turbine efficiency has to be fitted. The efficiency curve calculated in the previous step is therefore imported into Matlab, where a linear multivariable regression is carried out. The selected linear regression model has the approach:

$$\eta_{is,T} = C_1 + C_2 \cdot \dot{m}_T + C_3 \cdot p_{3''} \quad (3.11)$$

In the above approach the turbine efficiency is expressed as a function of the turbine mass flow, the inlet pressure and a constant term. The estimation of the turbine efficiency in partial load operation is a complex task and depends on a large number of influencing factors (compare Traupel [61]). The selected approach was used in the master thesis of Joaquín Perez [28] under the supervision of Prof. Dr. Thomas Schulenberg and will be retained for the new correlation.

Performing the linear regression of the calculated efficiency with the pressure and mass flow measured for Day1, we obtain the new empirical correlation for the turbine efficiency:

$$\eta_{is,T} = 0.63927 - 0.35172 \frac{\text{s}}{\text{kg}} \cdot \dot{m}_T + 0.21246 \frac{1}{\text{MPa}} \cdot p_{3''} \quad (3.12)$$

The Regression has a R-squared value of 0.892 which seem sufficiently close to 1 and a Root Mean Error of 0.0156. The coefficients C_1 , C_2 and C_3 have changed significantly compared to the previous correlation ($C_1 : 0.4412 \rightarrow 0.63927$; $C_2 : -0.4399 \rightarrow -0.35172$; $C_3 : 0.3229 \rightarrow 0.21246$). It therefore remains to be checked whether the new correlation also provides good agreement for Day2 and Day3 or whether further adjustment is necessary.

Next, the new efficiency correlation is implemented in the Dymola turbine model. The model is named *T_d1_N1_65_Overdetermined* and is also summarized in Table 3.3.

In order to verify the correct implementation of the new efficiency correlation, it is first implemented in the turbine model without the Stodola equation. Consequently, the measured inlet pressure is directly used as input. The model then provides the turbine shaft power as an output which is compared with the experimental data.

A comparison of the turbine shaft power of the Dymola model with the experimental data is shown in Figure 3.5. As can be seen, the experimental data are well represented over the entire duration of Day1. The mean absolute deviation of the turbine power is $\bar{\varepsilon}_{abs} = 1.38 \text{ kW}$, the mean relative deviation is $\bar{\varepsilon}_{rel} = 1.51\%$. Due to the strongly fluctuating course of the experimental data, better agreement cannot be expected.

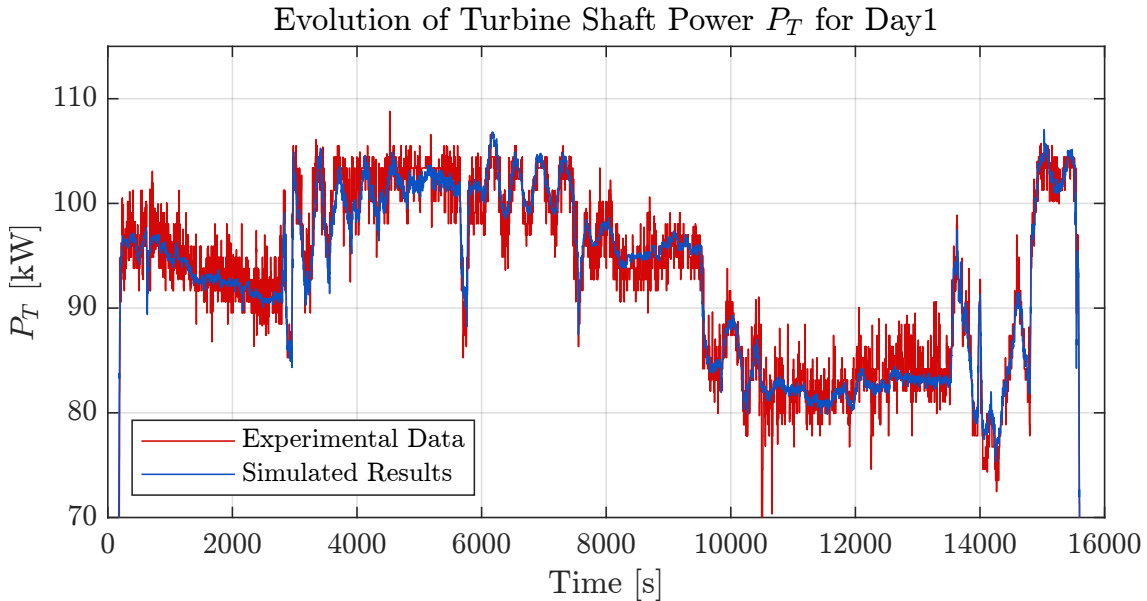


Figure 3.5.: Comparison of the turbine shaft power calculated in the Dymola turbine model using the new efficiency correlation (blue) and the experimental Data (red) for Day1. The model does not yet incorporate the Stodola equation and thus the measured inlet pressure is directly used as input.

The correct implementation of the new correlation can thus be regarded as verified. The validity of the correlation for Day1 can also be confirmed. However, since the correlation was fitted to the measurement data from Day1, the model must be validated with the measurement data of Day2 and Day3. In addition, a further validation of the model is required when the Stodola equation is added. These steps are carried out and explained in detail in Chapter 4.1.

3.4. Development of the Condenser Model

The basis for the condenser model is the TIL model *FinAndTube - MoistAirVLEFluid - ParallelFlowHX* as explained in Chapter 2.6.2.4. The geometry parameters of the MoNiKa condenser were implemented in the condenser model. These are summarized in Table A.1 in the Appendix A.

The correlation of Shah (see Chapter 2.4.1) serves as a heat transfer model between ORC fluid and tube walls. For the heat conduction in the tubes the formula introduced in chapter 2.4.2 is used and for the convective heat transfer on the air side the correlation according to Haaf (see Chapter 2.4.3) is implemented. As a fin efficiency model the correlation according to Schmidt is implemented as explained in Chapter 2.4.3.

Friedel's correlation (see Chapter 2.5.2) was initially implemented as the pressure loss model on the ORC side, although several correlations were tested. For the pressure loss on the air side, the Haaf correlation presented in Chapter 2.5.3 is used.

All four heat exchangers used in MoNiKa are combined in one model. Since the condenser model does not take hydrostatic effects into account, the four heat exchangers can be realised as a single heat exchanger with four times the height and four times the number of parallel flows.

Since the condenser model from the TIL library was used and only geometry parameters and predefined heat transfer and pressure drop models are passed, the correct implementation of the model can be considered verified.

The condenser model is first implemented based on the data from Day0 and compared to the results of Mariano Fossati's [11] Simulink condenser model. The model is then validated using the experimental data from Day1-3.

The condenser model is discretized in flow direction in a number of VLE-Fluid-Cells that has to be given by the user. To determine an adequate number of cells a grid sensitivity study is carried out which is explained in the following.

3.4.1. Grid Sensitivity Study

The condenser is discretized in a number of finite volume elements which is defined by the user. As in any numerical study it is a necessity to establish grid convergence to verify that the solution is insensitive to the grid resolution. Therefore, three simulations using different grids (coarse - 5 cells, medium - 10 cells, fine - 20 cells) with a constant refinement ration $r = 2$ have been executed. The variable used to evaluate the grid convergence is the enthalpy at the condenser outlet. The implemented model is summarized in Table 3.4.

MODEL	C_d0_GridStudy
INPUTS	$\dot{m}; p_1; h_A; p_{amb}; T_{amb}; \varphi; \dot{V}_{air};$
RELEVANT OUTPUTS	$h_1; T_1;$
CORRELATIONS	Heat Transfer: Shah & Haaf & Schmidt Pressure Loss: Friedel & Haaf
NOTE	For the grid study discretizations with 5, 10 and 20 cells are tested.

Table 3.4.: Developed Dymola model for the condenser grid sensitivity study.

The results of the simulations are shown in Fig.3.6. The simulation was started at $t=5000s$ because during the start up the fluid input variables are in the two-phase region and hence,

the inlet enthalpy cannot be clearly determined. The area marked in gray is the second mass flow transition in which, as already explained, the supercritical state could not be reached due to control problems and the inlet enthalpy can therefore not be determined. This area is not taken into account for the evaluation.

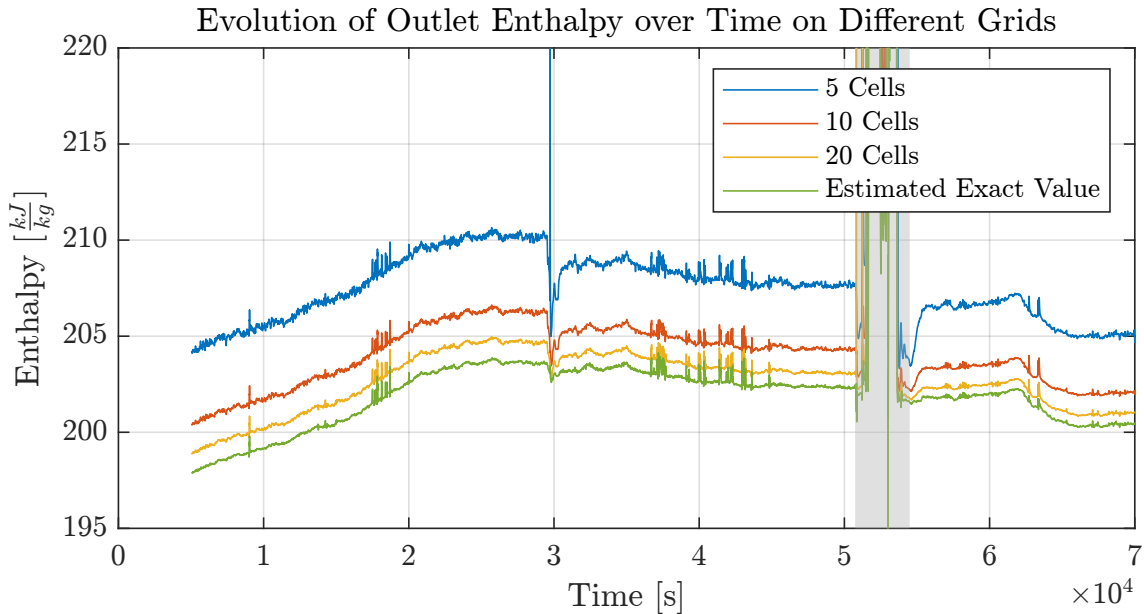


Figure 3.6.: Condenser discharge enthalpy over time for different grid resolutions.

To estimate the exact solution, i.e. for an infinite number of cells, a Richardson Extrapolation and the calculation of the Grid Convergence Index have been performed as explained in the following paragraph.

Richardson Extrapolation and Grid Convergence Index

The Richardson Extrapolation introduced by Lewis Fry Richardson in 1911 [38] offers a way of estimating the discretization error for monotonically converging grids and a constant refinement factor r . This allows the exact output variables to be estimated by extrapolating the results of the grids of different resolutions. This means that without additional simulation effort a statement can be made about the magnitude of the discretization error and the converged solution can be estimated using the available results. The extrapolation can be performed according to Ferziger [8]:

$$\phi_{exact} \approx \phi_h + \varepsilon_h^D. \quad (3.13)$$

The index h indicates the grid cell size, so ϕ_h is any simulation variable of the finest grid, while ϕ_{rh} and ϕ_{r^2h} represent the corresponding variable on the grid coarsened by the factor r or r^2 respectively. The discretization error of the finest grid ε_h^D can be approximated according to Ferziger as follows:

$$\varepsilon_h^D \approx \frac{\phi_h - \phi_{rh}}{r^p - 1}. \quad (3.14)$$

Roache [40] recommends an extrapolation from 3 grids, since then the order of convergence p can be calculated as follows:

$$p = \frac{\ln\left(\frac{\phi_{rh} - \phi_{r^2h}}{\phi_h - \phi_{rh}}\right)}{\ln(r)}. \quad (3.15)$$

The estimated converged solution (green) is also plotted in Figure 3.6. Based on the Richardson Extrapolation, the Grid Convergence Index GCI can be formulated according to Roache [40]:

$$GCI = F_s \frac{|e|}{r^p - 1}. \quad (3.16)$$

where $|e|$ is the relative error between two consecutively refined grids. In case of the finest grid it can be calculated as:

$$e = \frac{\phi_h - \phi_{rh}}{\phi_h} \quad (3.17)$$

F_s is a safety factor for a more conservative estimate, which according to Roache can be assumed to be 1.25 when using 3 grids. The GCI can be used to determine how accurately the variables were calculated on a grid. The GCI obtained does not represent an error limit, but rather an error range that could be exceeded in reality, but which allows the user to make a reliable estimate in practical use.

The calculated GCI for the medium grid (10 cells) and the fine grid (20 cells) are plotted for every time step in Figure 3.7. The estimated discretization error is below 1.8% for the medium grid and below 0.8% for the fine grid.

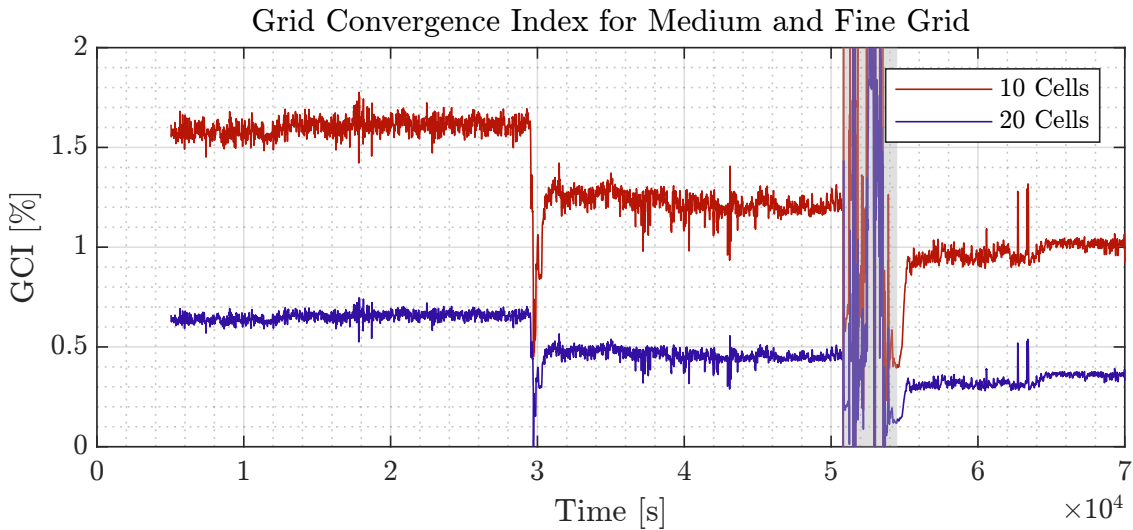


Figure 3.7.: Grid convergence index for medium an fine grid

Last, it is also necessary to check that the grid convergence is examined within the asymptotic range of convergence [31]. Otherwise, the solution is not asymptotically approaching a converged answer and thus the solution is not grid independent. When using three grids, this can be checked with the following relationship:

$$\frac{GCI_{rh,r^2h}}{r^p \cdot GCI_{h,rh}} \approx 1 \quad (3.18)$$

where GCI_{rh,r^2h} is the GCI for the medium grid and $GCI_{h,rh}$ the GCI for the fine grid. The results range from 0.9917 to 0.9979 which is close to one and thus indicates that the solutions are well within the asymptotic range of convergence.

Conclusion:

In this thesis, a discretization error of $\leq 1\%$ was aimed for and therefore a discretization of 20 cells is implemented in all subsequent condenser models.

3.4.2. Methods to Reduce Computation Time

In order to ensure a precise calculation of the output variables, the condenser model is implemented with a discretization of 20 cells in flow direction. However, test have shown that the computing time of the condenser model on the computer used for this thesis can surpass 24h even for lower discretizations when using a propane nitrogen mixture instead of pure propane. This makes simulations for Day1-3, where the mixture has to be used, unpractical to work with. Methods to reduce the computing time must be found, especially when considering a later extension of the model in order to close the MoNiKa cycle. The measures that have been taken in this thesis are explained in the following sections.

3.4.2.1. Resampling of Measurement Data

The sampling frequency of the provided input data for the 24 hour condenser test run of Day0 was 0.1 Hz resulting in one measurement value every 10 seconds. For the turbine test runs of Day1-3 the sampling frequency was 1 Hz which results in one measurement value per second. Some of the measurement data include outliers and measurement noise. These high-frequency fluctuations are not of interest for the simulations. In order to shorten the computing time, the input signals are first filtered and then interpolated to a coarser time vector. This enables the solver to choose larger time steps. The procedure is briefly explained in the following:

1. Filtering of Measurement Data:

In a first step all input signals are filtered using a 2nd order Butterworth low-pass filter. The cutoff frequency has to be determined for each sensor individually.

Care must be taken to set the filter parameters in such a way that undesired fluctuations are reduced, but at the same time the qualitative progression of the curves is not unacceptably distorted.

An example of the filtering is given in Figure 3.8. As can be seen in the figure, both the outliers and the high-frequency fluctuations can be significantly reduced by filtering. In the example shown, a cutoff frequency of 0.001 Hz was used. The sampling frequency for the data is 0.1 Hz and consequently the Nyquist rate is 0.05 Hz. For further information of the filter used see [29]. The smoother curves then allow the solver to chose a bigger time step which results in a reduction of computation time. The Matlab code used to filter the input data, is attached in Appendix B.2.

2. Resampling to a new non-uniform spaced Time Vector:

Since it is not possible to filter the measurement fluctuations for every fluid variable without distorting the qualitative course (e.g. when abruptly changing the mass flow), resampling to a non-uniformly spaced time vector is also carried out. Fluctuations in stationary operating phases that are still present after filtering can be reduced further by interpolating to a suitable time vector with coarse time steps. At the same time, the time vector can contain smaller time steps in transient operating phases, so that the characteristic of the curves is retained.

For this purpose, a Matlab-Function was written which requires as input a desired total number of time steps, interval boundaries and a weighting of the time step density in the corresponding interval. It then returns a new, non-uniform spaced time vector that takes these conditions into account. To do this, the user must define intervals based on the

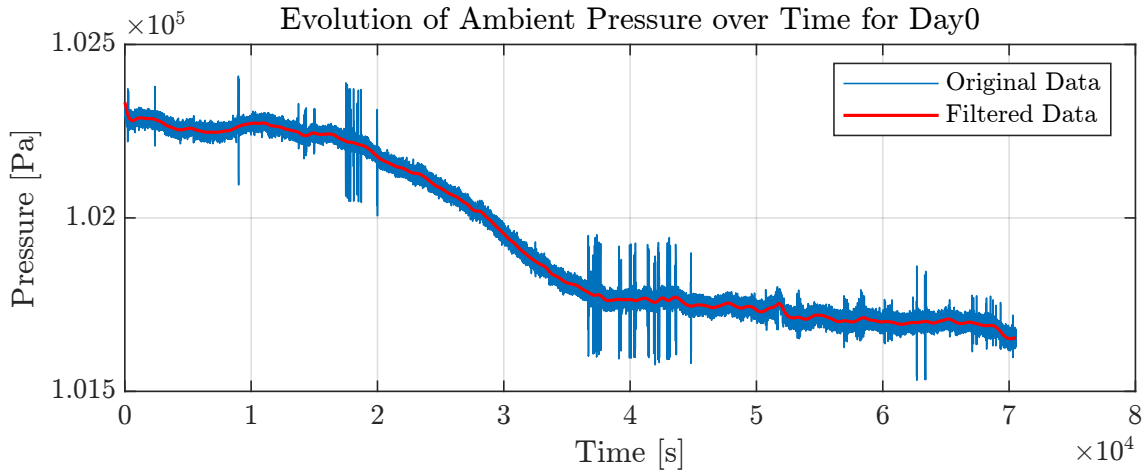


Figure 3.8.: Example of the filtered and unfiltered input data for the ambient pressure signal for Day0.

input data and specify how compressed the time steps should be in the respective interval. Afterwards it must be checked for all input data if the resampled curves still sufficiently fits the original data and if necessary interval boundaries, refinement or total number of steps have to be adjusted in an iterative process. The Matlab code used to filter and resample the input data, as well as the Matlab-Function for creating the new non-uniformly spaced time vector are attached in Appendix B.2.

The resampling is shown in Figure 3.9 using the example of the condenser inlet enthalpy that was already shown in Chapter 3.1.1. As can be seen in the figure, a total of 9 intervals with different time step widths were introduced. As explained before, interval 1, 6 and 9 are in the two-phase region where the inlet enthalpy cannot be calculated unambiguously. These intervals therefore have only a minimal resolution. Interval 3, 5 and 8 are stationary operating points which requires only a low resolution. However, interval 2, 4 and 7 are transient operating states where a much higher density of time steps is required which in the figure results in the high density of green points in this region.

The resampling to a new time vector also makes it possible to reduce the size of the input tables in Dymola from many thousands to a few hundred entries, which enables smoother work with the software.

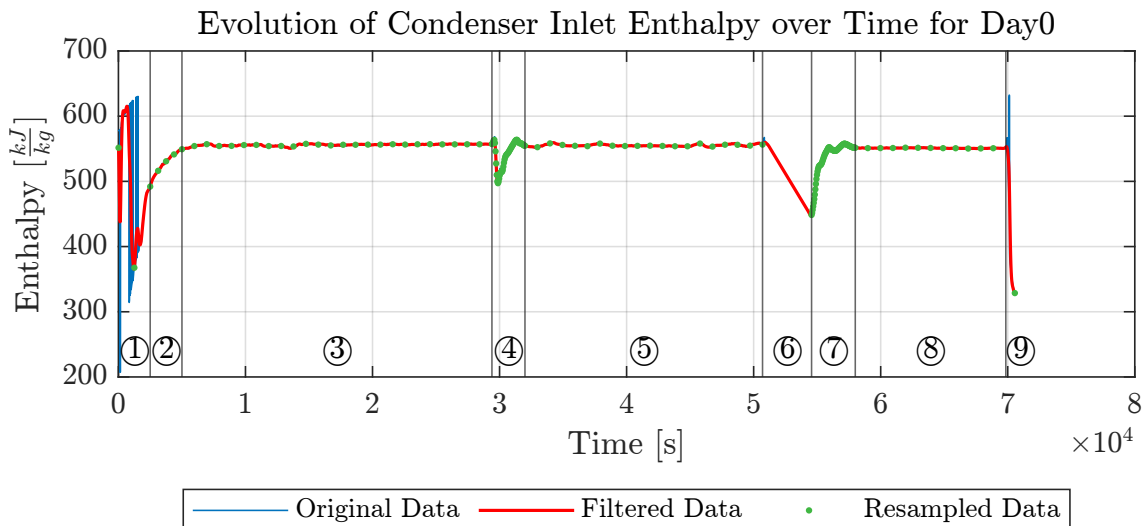


Figure 3.9.: Example of unfiltered, filtered and resampled condenser inlet enthalpy for Day0. In the example the resampling was carried out by interpolation to a new time vector containing 200 time steps.

3. Validation of the Procedure:

In order to evaluate whether the procedure leads to a reduction in computation time and to what extent the results are influenced, a series of simulations was carried out. The condenser model for Day0 was simulated three times, first with original input data (7056 time steps), then with input data which were resampled to a time vector with 400 steps and finally with input data which were resampled to a time vector with 200 steps.

The results for outlet enthalpy and inlet pressure of the condenser are shown in Figure 3.10. Both simulations with resampled data show good agreement with the simulation using the original data. As before, the area of the second mass flow transition was colored gray in the graphic and should not be taken into account. It can be clearly seen that the curves for the outlet enthalpy are much smoother in the case of the resampled data and do not contain any high-frequency fluctuations as in the case of the simulation with the original data. The latter shows clear fluctuations in the results of the outlet enthalpy especially in the range of $35000s < t < 45000s$. This effect is most likely due to the elimination of outliers in the ambient temperature measurements. The influence of individual parameters on the output variables is considered separately in Chapter 4.4.

For the calculated condenser discharge enthalpy h_1 the mean relative deviation between the model with the original data input and the model where the input data was resampled to 400 time steps is $\bar{\epsilon}_{rel} = 0.0214\%$. For the model with resampled input data to 200 time steps the deviation is only slightly higher with $\bar{\epsilon}_{rel} = 0.0258\%$.

Comparison of Results for Resampled Inputs for Day 0

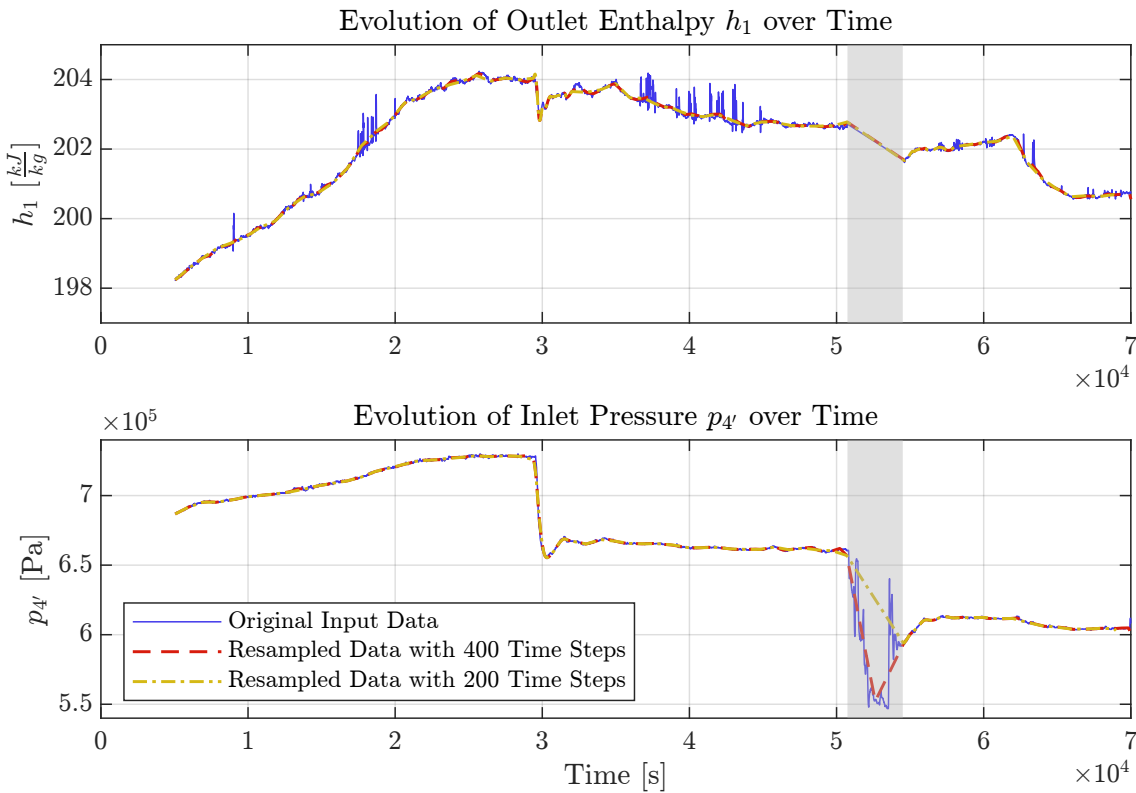


Figure 3.10.: Validation of resampling method: Comparison of the results for the original input data, the input data reduced to 400 time steps and the input data reduced to 200 time steps. The area of the second mass flow transition is marked in gray.

A comparison of the computation time as listed in Table 3.5 shows a clear reduction from 215 minutes in the case of the original input data to 37 minutes or 26 minutes in the case of the resampled data to 400 or 200 time steps respectively. As can also be seen from the

table, the maximum simulation step size could be increased by two orders of magnitude through resampling.

RESAMPLING	Original Data 7056 steps	Resampled Data 400 steps	Resampled Data 200 steps
COMPUTATION TIME	1.29e+04 s (215 min)	2.22e+03 s (37 min)	1.58e+03 s (26 min)
MINIMUM INTEGRATION STEPSIZE	8.36e-06 s	3.42e-05 s	1.23e-04 s
MAXIMUM INTEGRATION STEPSIZE	4.99 s	454 s	828 s

Table 3.5.: Simulations for evaluation of data preparation. All three simulations used the condenser model with a discretization of 20 cells and the correlations and inputs as they were resumed in Table 3.4.

Note:

A lower number of time steps to which the data is resampled does not necessarily lead to a lower simulation time since the DASSL solver chooses an adequate time step to match the specified tolerances. However, a smaller number of time steps leads to reduced fluctuations due to the loss of information in the range between two consecutive time steps. This enables the solver to choose larger time steps and hence reduces the calculation time. In stationary operation this can be advantageous in terms of computing time without leading to unacceptable errors. During changing operating conditions, however, care must be taken that the number of remaining time steps in the range does not become too small.

3.4.2.2. Influence of Pressure Drop Model on the Outlet Enthalpy

The calculation time increases significantly when changing the working fluid from pure propane to a propane-nitrogen mixture. The condenser model for Day0 (using pure propane as working fluid) with resampled input data to 400 time steps needs 37 minutes to calculate a 24h test run. In comparison the same model using the propane-nitrogen mixture needs several days to calculate the results of the 4h test run of Day3. A direct comparison of the simulations for different days is difficult and must be treated with caution. In the test runs from Day1-3, more operating points are approached, which leads to more transient operating states and thus prompts the solver to select small time steps more frequently. Nevertheless, the comparison makes clear that the computing time increases by orders of magnitude when changing the working substance from a pure fluid to a fluid mixture.

Therefore, further methods have to be found to reduce the computation time. It turned out that especially Friedel's pressure loss correlation as it was introduced in Chapter 2.5.2 has a high impact on the calculation time when fluid mixtures are used. To investigate whether this pressure loss model is necessary, four simulations were carried out for the pure propane model of Day0, each using a different pressure loss model. The pressure loss model according to Friedel, the model according to Konakov, a model with a constant pressure loss coefficient and a zero-pressure-drop model were compared in terms of calculation time and agreement of results. All models are based on the condenser model already presented, which was summarized in Table 3.4, and only differ in its pressure loss model on the ORC side. The models and the required computation time are resumed in Table 3.6.

The simulation results for outlet enthalpy and inlet pressure are shown in Figure 3.11. As can be seen from the graph for the outlet enthalpy, the pressure loss model used had little

MODEL NAME	COMPUTATION TIME	PRESSURE DROP MODEL
C_d0_200_Friedel	1.58e+03 s (26 min)	Friedel
C_d0_200_Konakov	1.55e+03 s (25 min)	Konakov (with smoothed transition to Hagen-Poiseuille for laminar flow)
C_d0_200_Zeta	1.38e+03 s (23 min)	Constant Pressure Loss Coefficient $\xi = 20$
C_d0_200_Zero	1.32e+03 s (22 min)	$\Delta p = 0$

Table 3.6.: Dymola models used to compare the effects of different pressure loss correlations in terms of calculation time and agreement of results. All models are based on the condenser model with a discretization of 20 cells, which was summarized in Table 3.4. The models only differ in its respective pressure loss correlation on the ORC side.

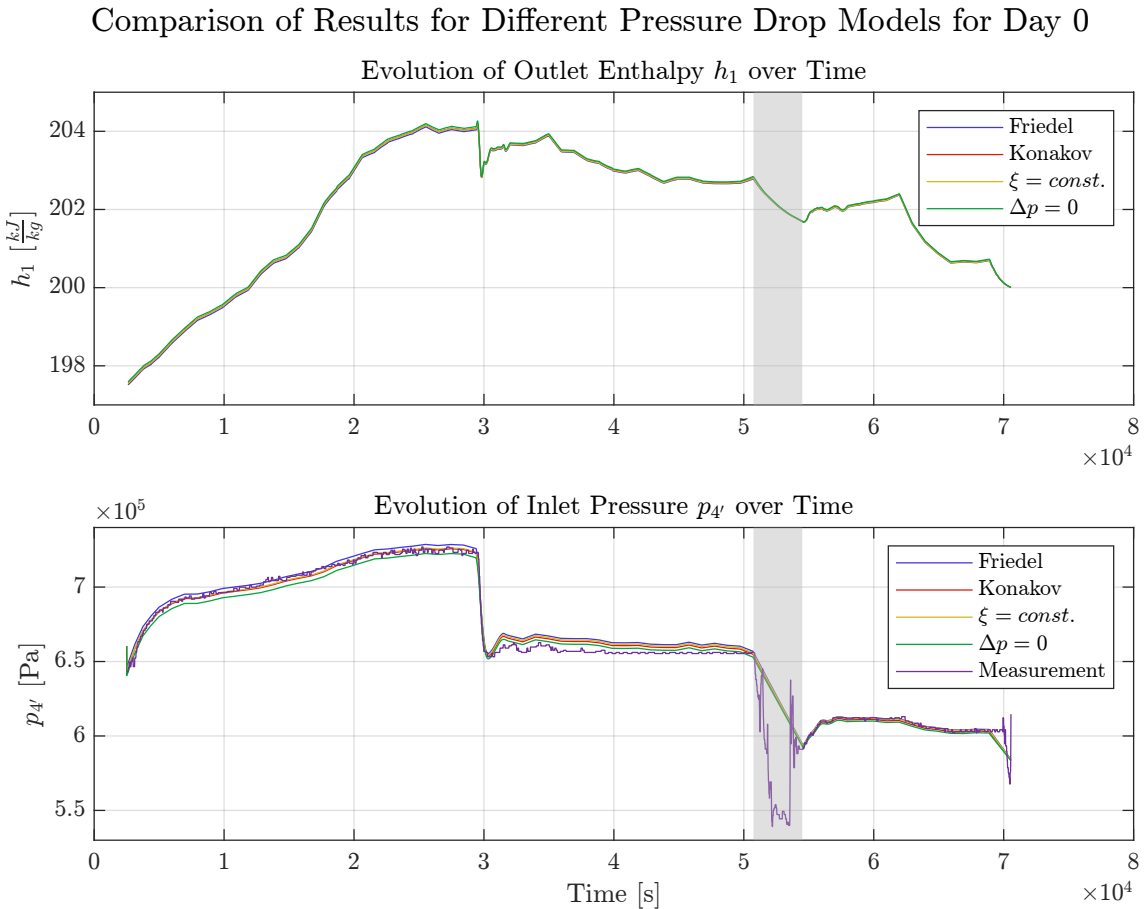


Figure 3.11.: Study on the influence of the pressure drop model: Comparison of the results for the pressure drop models according to Friedel, Konakov, $\xi = \text{const.}$ and $\Delta p = 0$. The area of the second transition where the results should not be taken into account is colored gray. All models used a discretization of 20 cells for the condenser and the resampled data on 200 time steps.

influence on the outlet enthalpy. The simulation with the zero pressure drop model results in the highest outlet enthalpy over the entire duration of the simulation, the model with the Friedel correlation in the lowest. However, the average relative deviation of the two curves is only 0.029%. The maximum relative deviation is also very low at 0.053%. The effect of the examined pressure loss models on the calculated outlet enthalpy was therefore negligible for Day0.

The second subplot shows the evolution of the calculated inlet pressure over time for the pressure loss model. The graph also contains the measured inlet pressure (purple). For $30000\text{s} < t < 50000\text{s}$ measurement problems for the inlet pressure occurred. In this range, the measured inlet pressure (purple) is below the measured outlet pressure¹ (green). This does not make physical sense, since a flow reversal would then have to occur. In addition, the measured value shows no development in large parts of this range but alternates between only two numerical values. This area is therefore not considered for the evaluation.

An evaluation of the mean relative deviations of all simulation results with the measured inlet pressure for range 1 ($5000\text{s} < t < 29000\text{s}$) and range 3 ($55000\text{s} < t < 69000\text{s}$) shows that the pressure drop in both ranges is best determined by the model with constant pressure loss coefficient ($\xi = 20$). Here the mean relative deviation was 0.17% in the first range and 0.10% in the third range.

Due to the small influence on the outlet enthalpy and no improvement in the pressure approximation, the use of complex and computationally intensive correlations such as Friedel in the MoNiKa condenser model does not seem reasonable.

Conclusion:

For the condenser model, the calculated outlet enthalpy is insensitive to the tested pressure loss models. However, the pressure drop model has a significant impact on the computation time when using a fluid mixture instead of pure propane. Since the pressure drop between turbine outlet and condenser inlet is significantly higher than the pressure drop occurring in the condenser, it was therefore decided to use a zero pressure drop model in the condenser model. For the coupled turbine-condenser model the total pressure drop occurring between turbine outlet and condenser outlet will then be approximated by using a separate hydraulic resistance.

3.4.3. Comparison with the Simulink Condenser Model by Mariano Fossati and Introduction of a Correction Factor

In this chapter, the condenser model presented is compared with the Simulink condenser model developed by Mariano Fossati [11] as part of his master thesis. Only stationary results were available from the Simulink model for each of the three regions. The Dymola condenser model is implemented as explained in the previous chapters and is resumed in Table 3.7. The results for the condenser outlet enthalpy and outlet temperature of the two models are plotted in Figures 3.12 and 3.13, respectively, along with the measurement data.

As can be seen in the graphs, the condenser output variables of both models are below the measured values. An overestimation of the heat transfer in the models is not surprising since a number of empirical correlations were used. In addition, the models are based on an idealized consideration of the condenser. In the real condenser, gravitational effects also play a role, which can lead to a higher liquid content of the ORC fluid in its lower sections. In the simulation models, on the other hand, a perfectly homogeneous flow on

¹The measured outlet pressure in the graph corresponds to the calculated inlet pressure of the zero-pressure-drop model (green)

MODEL	C_d0_200_ZeroPD
INPUTS	$\dot{m}; p_1; h_4'; p_{amb}; T_{amb}; \varphi; \dot{V}_{air};$
RELEVANT OUTPUTS	$h_1; T_1;$
CORRELATIONS	Heat Transfer: Shah & Haaf & Schmidt Pressure Loss: Zero-Pressure-Drop & Haaf
NOTE	The condenser is discretized with 20 cells. The input data was resampled to a time vector with 200 time steps as explained in Chapter 3.4.2.1.

Table 3.7.: Developed Dymola condenser model with input data for Day0.

the ORC side is assumed. In addition, the models assumes a perfectly homogeneous flow through the cooling fins on the air side.

However, it is remarkable that the results of the Simulink model are much closer to the experimental data, although most of the implemented correlations are identical in both models. The deviations of both models compared to the experimental data are quantified in Table 3.8. As can be seen there, the absolute deviations for the Simulink model are about half the deviations of the Dymola model, but still significant.

		DYMOLA			SIMULINK		
		REGION 1	REGION 2	REGION 3	REGION 1	REGION 2	REGION 3
t_1	[s]	2600	31000	55000	2600	31000	55000
t_n	[s]	29000	50000	69000	29000	50000	69000
$\bar{\epsilon}_{abs}$	[kJ/kg]	31.29	23.60	17.39	15.37	13.86	9.98
$\bar{\epsilon}_{rel}$	[%]	13.45	10.41	7.94	6.60	6.11	4.56
$\epsilon_{abs,max}$	[kJ/kg]	32.11	24.33	18.03			
	[s]	6999	31490	68280			
$\epsilon_{rel,max}$	[%]	13.90	10.67	8.24			
	[s]	6999	31490	68280			

Table 3.8.: Deviations of the condenser outlet enthalpy between the Dymola or Simulink condenser model and the experimental data for Day0. t_1 refers to the beginning and t_n to the end of the comparison period. For the maximum values of the deviations, the time of occurrence is also specified.

A detailed comparison of the models showed that the Simulink model used a full load cooling airflow of $44 \frac{m^3}{s}$ per fan. In the Dymola model, on the other hand, a volume flow of $528000 \frac{m^3}{h}$ for the entire system ($= 48.89 \frac{m^3}{s}$ per fan) was assumed, which refers to the manufacturers process and plant description [25]. The deviation in the volume flow for the cooling air between the models is therefore about 10%. The effects of this deviation were examined more closely as part of a sensitivity analysis that is presented in Chapter 4.4, but can not explain the extent of the deviations.

Another difference between the two models is that the Simulink model, in addition to the input parameters of the Dymola model, also requires the outlet temperature of the cooling air as an input. In the Simulink model, inlet and outlet air temperature together with the propane temperature are then used to calculate the arithmetic mean temperature difference. Afterwards, the arithmetic mean temperature difference is used together with

the overall heat transfer coefficient to determine the heat flow. Because of this procedure, the overall heat transfer in the Simulink model is largely predetermined. Therefore, a better approximation of the experimental data by the Simulink model is to be expected. However, the outlet temperature of the cooling air is generally not known beforehand, making this approach unsuitable for general predictions.

As can be seen from Table 3.8, for the Dymola model the maximum relative deviations for all 3 regions are only slightly higher than its mean relative deviations. The maximum relative deviation for region 1 is 0.45 percentage points higher than the mean relative deviation. For region 2 and day 3, the differences are even smaller, at 0.26 and 0.3 percentage points, respectively. Since the relative deviation of the results within each region is relatively constant, the approach is followed using a constant correction factor to achieve a better approximation of the results.

The use of a correction factor is already implemented in the TIL heat transfer correlations and only needs to be specified as a parameter. The final heat transfer coefficient is then determined by multiplying the calculated heat transfer coefficient of the respective empirical correlations by this factor. The results are presented in Chapter 4.2.

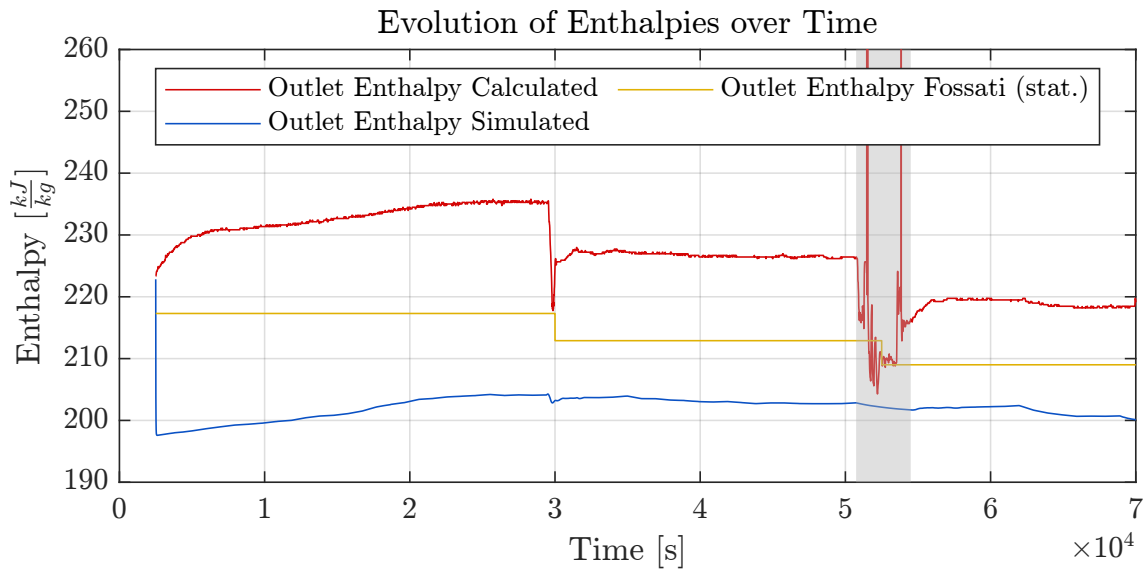


Figure 3.12.: Evolution of the condenser outlet enthalpies as calculated from measurement data (red), according to the Dymola condenser model (blue) and according to the Simulink condenser model (yellow).

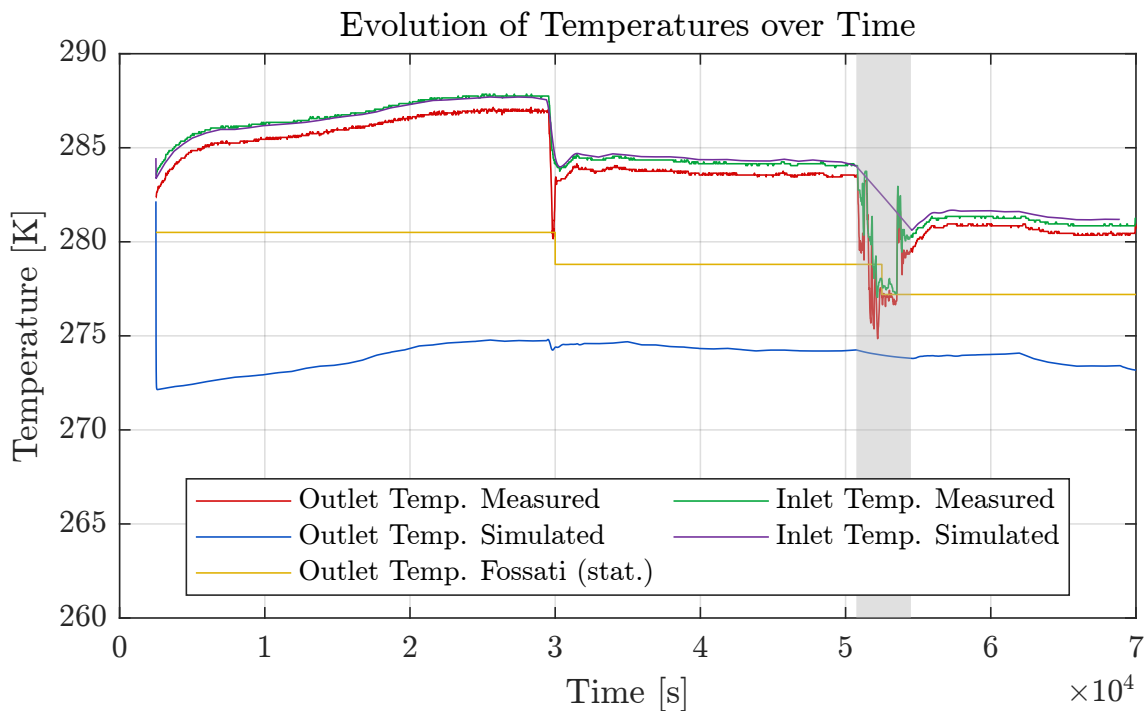


Figure 3.13.: Evolution of the condenser outlet temperatures for the experimental data (red), according to the Dymola condenser model (blue) and according to the Simulink condenser model (yellow).

3.5. Development of the Coupled Turbine-Condenser Model

The coupled overall model essentially consists of the turbine model and the condenser model. However, since a non-negligible pressure loss in the pipe system between the turbine and the condenser occurs, this must be modeled as well. Since the turbine outlet temperature is around 30°C and thus, the temperature gradient to the ambient air is relatively small, no heat transfer is taken into account for these pipes.

Based on the findings of Chapter 3.4.2.2, no pressure loss on the ORC side is taken into account in the condenser model. The pipe model must therefore approximate the measured pressure loss in the pipes and the condenser, i.e. between the turbine outlet and the condenser outlet.

To not significantly increase the computing time, the pipes are not discretized with finite volumes. Instead, the occurring pressure loss is modeled using a hydraulic resistor with a constant pressure loss coefficient. The calculation of the pressure loss is then based on Equation 2.47 as introduced in Chapter 2.5.

This simplified pipe model receives as input the mass flow \dot{m} , the outlet enthalpy of the turbine h_4 and the measured pressure at the condenser outlet p_1 . The pressure at the outlet of the turbine p_4 is then determined as the output of the model.

A suitable value for the pressure loss coefficient for Day1 was determined empirically. This value was then validated using the data for Day2 and Day3.

The results are shown in Figure 3.14. For a constant pressure loss coefficient $\xi = 50$ (with a hydraulic diameter of $d=150\text{mm}$), the pressure for all three days is well approximated. The mean relative deviation between measured (red) and calculated (blue) turbine outlet pressure over the entire range of simulation is 0.177% for Day1, 0.186% for Day2 and 0.289% for Day3. The measured condenser outlet pressure (green) that served as an input of the model is also shown in the figure.

A graphical representation of the coupled Dymola model containing the turbine model, condenser model, hydraulic resistance and input data for Day3 was already given in Chapter 2.6.2.5 in Figure 2.12. The validation of the coupled model using the experimental data for turbine power and condenser outlet enthalpy from Day1-3 is carried out in Chapter 4.3.

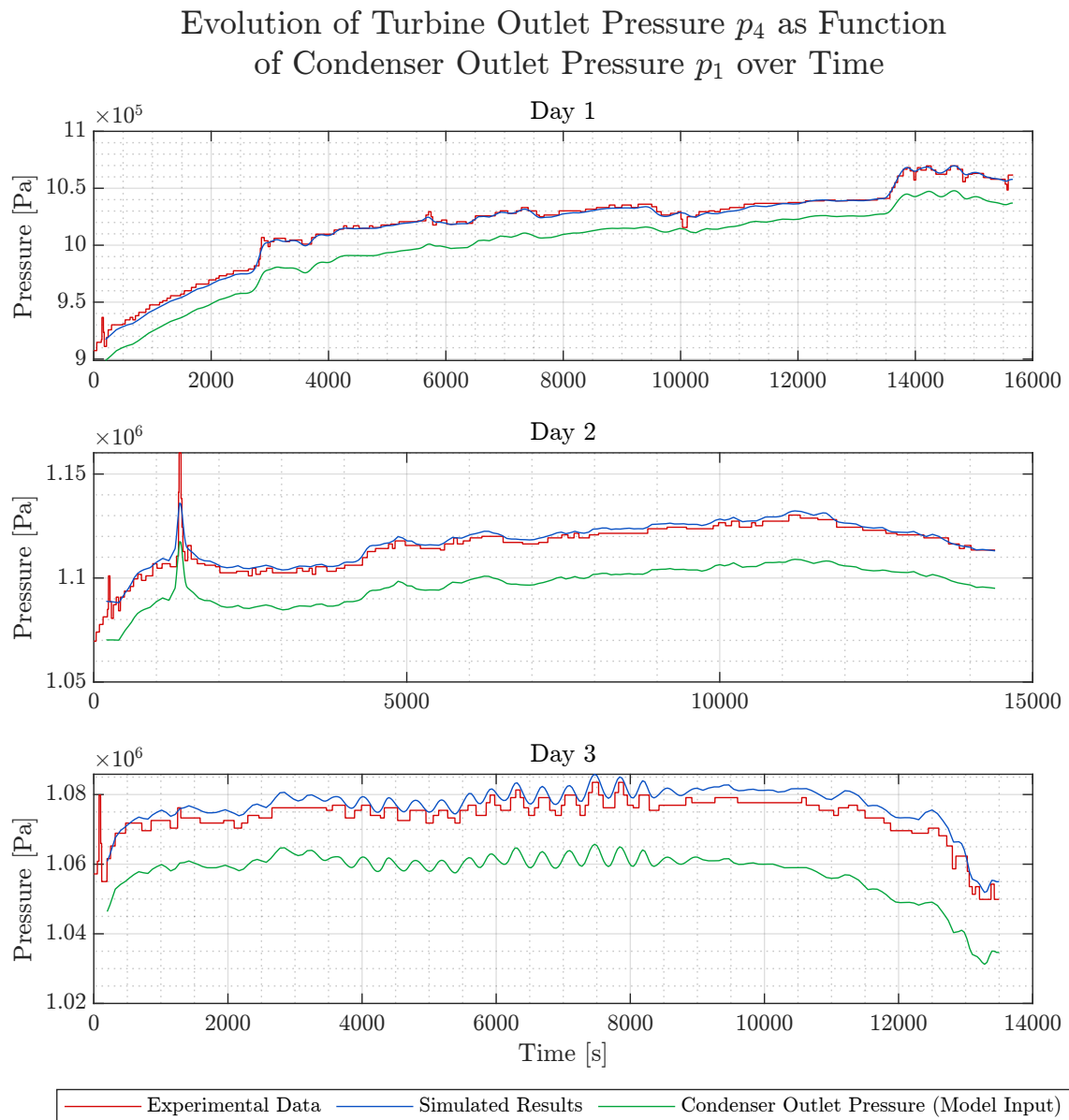


Figure 3.14.: Modeling of the pressure drop between turbine and condenser with constant pressure loss coefficient $\xi = 50$ for Day1-3.

4. Verification and Validation of the Models using Experimental Data

4.1. Verification and Validation of the Turbine Model

The turbine model presented in Chapter 3.3 is now verified using the experimental data from Day1 and validated with the data from Day2 and Day3. Table 4.1 gives an overview of the Dymola models used for this purpose. All models contain the newly developed turbine efficiency correlation (Equation 3.12), the modified Stodola correlation (Equation 2.9) and use a propane nitrogen mixture with 1.65% nitrogen content. All three Dymola models listed in the table contain the identical turbine model and differ only in the specified input data. All input data for the turbine models are unfiltered. Filtering and resampling, as explained in Chapter 3.4.2.1, was first introduced for the condenser and coupled models.

MODEL	Day1: T_d1_Nc_1.65 Day2: T_d2_Nc_1.65 Day3: T_d3_Nc_1.65
INPUTS	$\dot{m}_T; p_4; h_{3''};$
RELEVANT OUTPUTS	P_T
CORRELATIONS	Turbine Efficiency Correlation & Stodola Equation
NOTE	The Dymola models listed above contain the same turbine model and differ only in the input data.

Table 4.1.: Models for Verification and Validation of Turbine Model

4.1.1. Verification of the Turbine Model with Data from Day1

Since the inlet pressure is a variable in the efficiency correlation it remains to be checked whether the correlation still delivers good approximations for the turbine shaft power when the inlet pressure is not given as an input but instead is calculated with the Stodola equation.

The turbine model was executed with the input data from Day1. The results are shown in Figure 4.1. The first subplot shows the measured turbine shaft power (red), the shaft

power according to the Dymola model (blue) and the results of Julia Filipe's [9] Simulink model (yellow) for comparison. The Simulink model was run in stationary operation for all operating points of Day1 and simulated transiently for selected operating conditions with a duration of 600s each. For the Simulink model both stationary and transient results are plotted in the graph.

Since the experimental data for the turbine shaft power fluctuates strongly and the Dymola simulation also shows strong fluctuations due to the fluctuating mass flow input, the curves were filtered with a 2nd order Butterworth low-pass filter and shown in Figure 4.2 for better comparability. The sampling frequency of the data was 1 Hz, the cutoff frequency used for filtering was 0.01 Hz. The Matlab-Function used for the filtering is attached in Appendix B.3. For further information of the filter used see [29].

As can be seen in Figure 4.1, the output power (first subplot) shows good agreement with the measurement data whenever the Stodola equation gives a good estimate for the turbine inlet pressure (second subplot).

This is not the case for the entire duration of the simulation. Deviations in the pressure approximation seem to occur when the bypass valve (subplot 3) is opened or closed at high system pressures. It is assumed that the provided data for the turbine mass flow (which is an input parameter for the Stodola Equation) is error-prone for these conditions. Due to a defect of the mass flow sensor FI10-02 the turbine mass flow could not be measured during operation but instead had to be estimated. This was done by estimating the bypass mass flow from the opening position of the bypass valve and then subtracting this value from the total mass flow. However, a analysis of this procedure suggests that it was not taken into account that with the same degree of opening of the bypass valve for a higher system pressure, a larger mass flow flows through the bypass than for a lower system pressure. This might be a possible explanation for the occurring deviations.

The observation mentioned represents a potential for improvement of the model. In order to implement this, however, the characteristics of the valves and the exact pressure loss up to the branch of the bypass must be known. Due to time constraints, this was not possible in the current thesis.

Despite all, in general the shaft power agrees well with the experimental data whenever the input pressure is well approximated. The average absolute deviation of the turbine power is 3.07kW^1 and the average relative deviation is 3.50%. The agreement with the experimental data for Day1 is similar to that for the Simulink model by Julia Filipe. Here the average absolute deviation was 3.97kW and the average relative deviation was 4.41%. Both models also deliver similar results for the maximum deviations. These are summarized in Table 4.2 which is inserted at the end of the next section.

The results of this section do not yet show whether the turbine model is also applicable for a general case. Since the data from Day1 was used to fit the efficiency correlation, a good approximation of the results for this data set was to be expected. Therefore, so far it was only possible to verify whether the correlations were correctly implemented in the model. In the next step, the model is validated with the experimental data from Day2 and Day3.

¹All deviations were calculated from the filtered turbine shaft powers as shown in Figure 4.2.

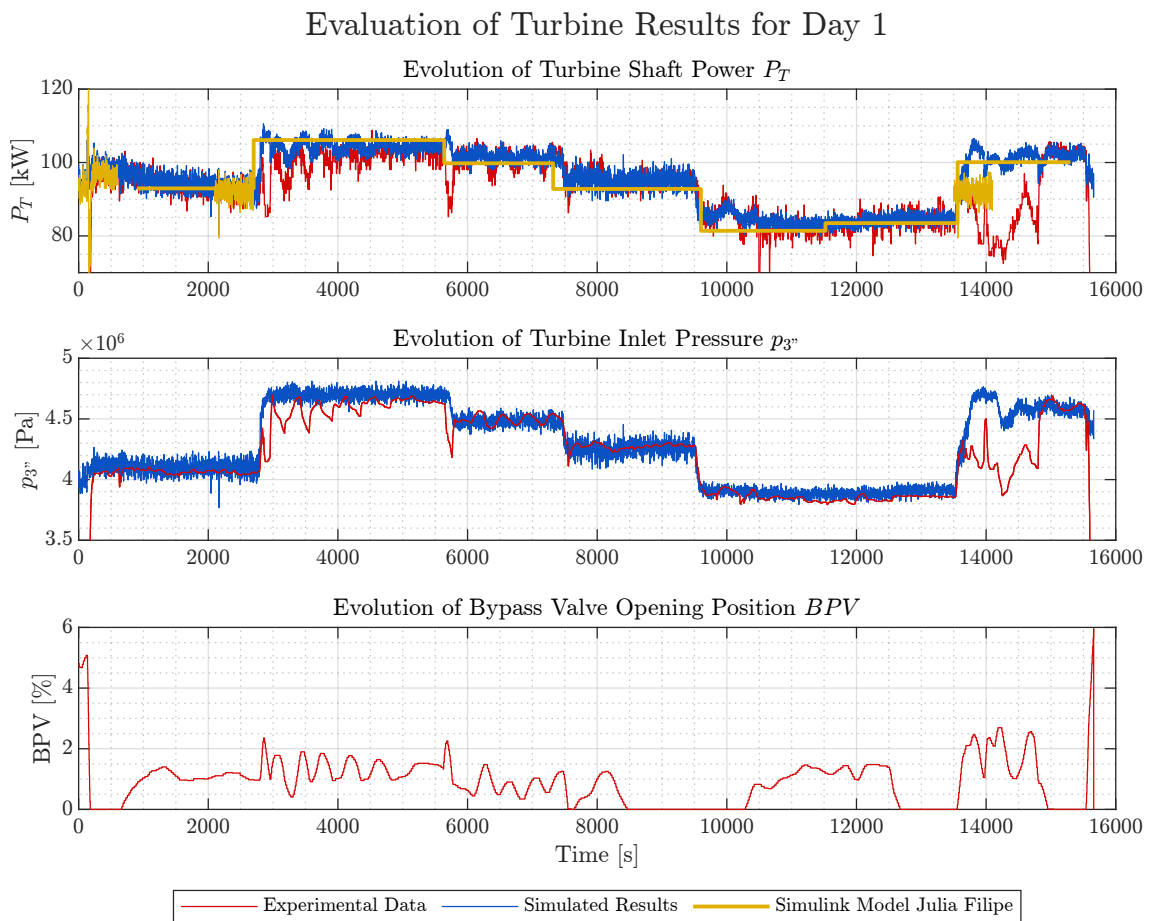


Figure 4.1.: Results of turbine model for Day1. For the turbine shaft power of the Simulink comparison model by Julia Filipe (yellow) both the stationary results and all available transient results are plotted. All plotted data is unfiltered.

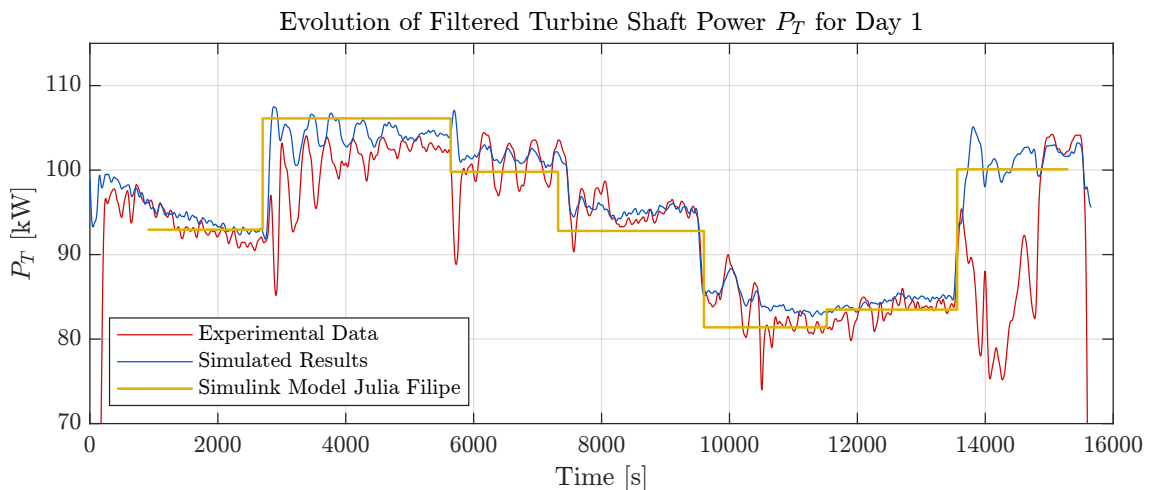


Figure 4.2.: Results of the filtered turbine shaft power for Day1.

4.1.2. Validation of the Turbine Model with Data from Day2 and Day3

As mentioned before, it has to be checked whether the developed turbine model also delivers reasonable approximations for the turbine power for Day2 and Day3. The results are presented in Figure 4.3 - Figure 4.6 and quantified in Table 4.2.

For Day3, the problem presented in the previous section occurs again, that when the bypass valve is opened for high system pressures, the pressure approximation via the Stodola equation loses precision. In these areas, the turbine shaft power then deviates from the experimental data.

Overall, the turbine shaft power is well represented over both days. With a mean absolute deviation of 1.16kW for Day2, an improvement could be achieved compared to the Simulink model, which approximates the results with a mean absolute deviation of 2.45kW. For Day3, the mean absolute deviation could even be reduced from 8.60kW in the Simulink model to 2.97kW. More detailed information about the absolute and relative deviations can be found in Table 4.2.

The qualitative progression of the shaft power curves could also be improved for both Day2 and Day3 compared to the Simulink model. See Figure 4.4 and Figure 4.6.

Due to the low mean relative deviation of the turbine shaft power for all three days, the turbine model is considered validated.

		DYMOLA			SIMULINK		
		DAY1	DAY2	DAY3	DAY1	DAY2	DAY3
t_1	[s]	200	482	415	901	482	1382
t_n	[s]	15560	14400	13070	15300	13501	13070
$\bar{\epsilon}_{abs}$	[kW]	3.07	1.16	2.97	3.97	2.45	8.60
$\bar{\epsilon}_{rel}$	[%]	3.50	1.15	3.04	4.41	2.42	8.78
$\epsilon_{abs,max}$	[kW]	25.34	5.00	15.01	24.91	9.42	23.77
	[s]	14075	13608	12755	14267	12603	5520
$\epsilon_{rel,max}$	[%]	33.65	4.93	15.73	33.14	9.13	23.43
	[s]	14075	13608	12755	14267	12603	5520

Table 4.2.: Deviations of the turbine shaft power between the Dymola or Simulink turbine model and the experimental data for Day1-3. t_1 refers to the beginning and t_n to the end of the comparison period. For the maximum values of the deviations, the time of occurrence is also specified. The calculation of the deviations was for all days carried out for the filtered curves.

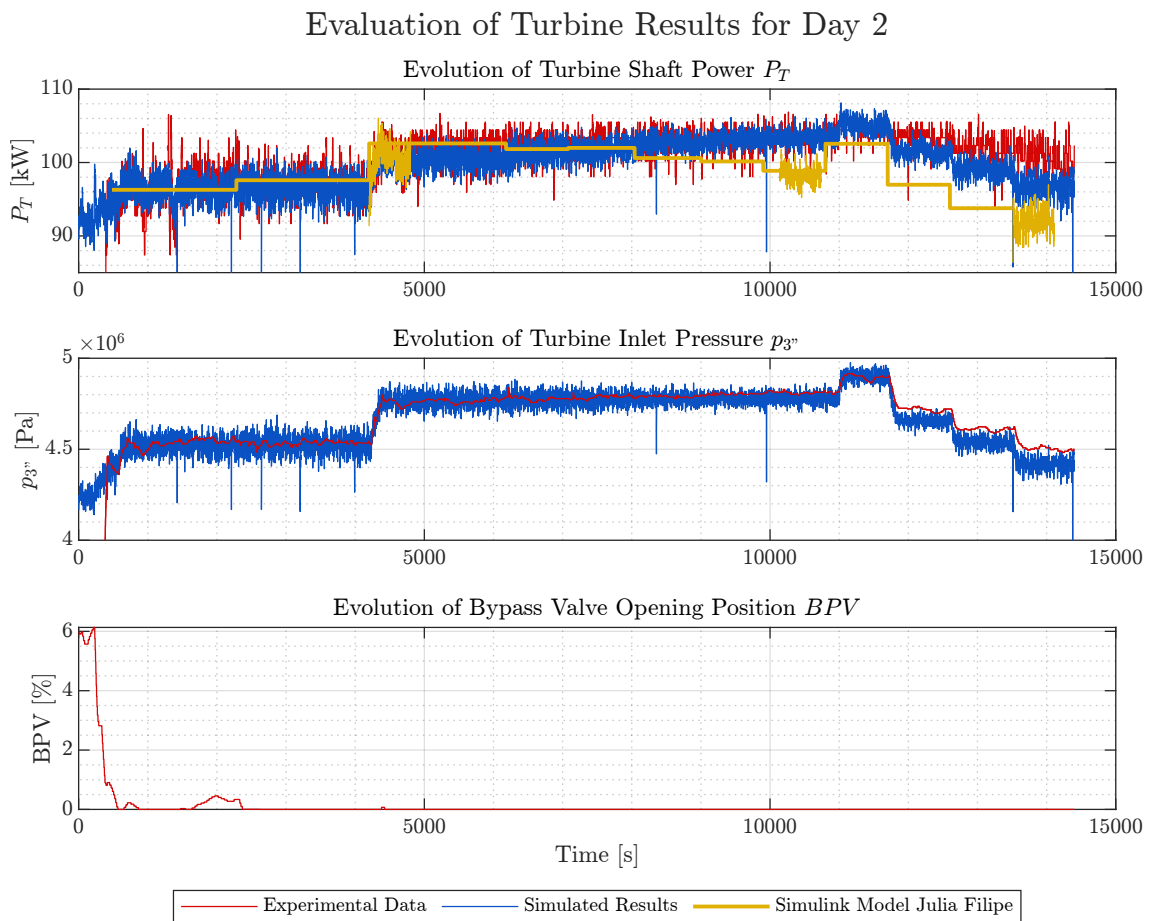


Figure 4.3.: Results of turbine model for Day2. For the turbine shaft power of the Simulink comparison model by Julia Filipe (yellow) both the stationary results and all available transient results are plotted. All plotted data is unfiltered.

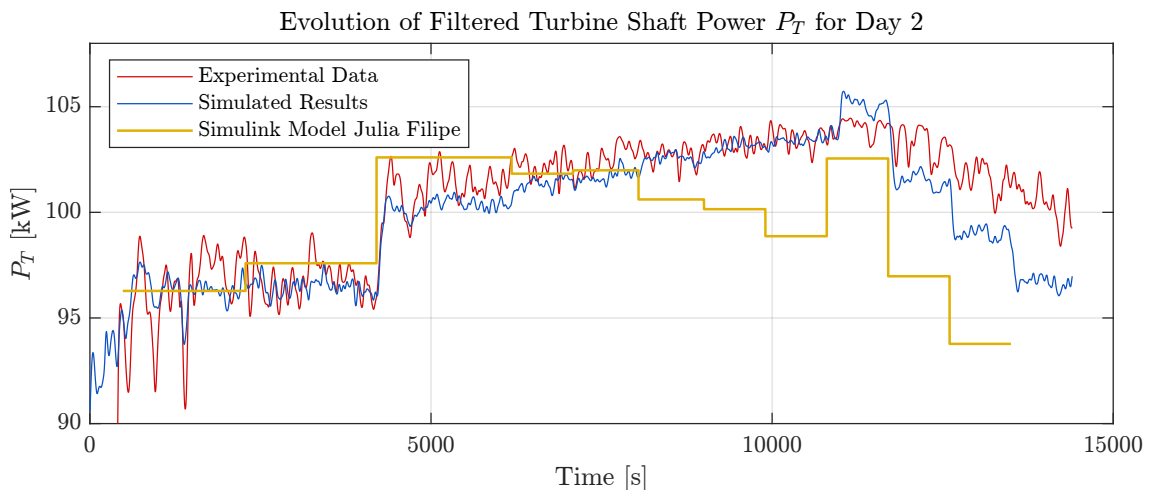


Figure 4.4.: Results of the filtered turbine shaft power for Day2.

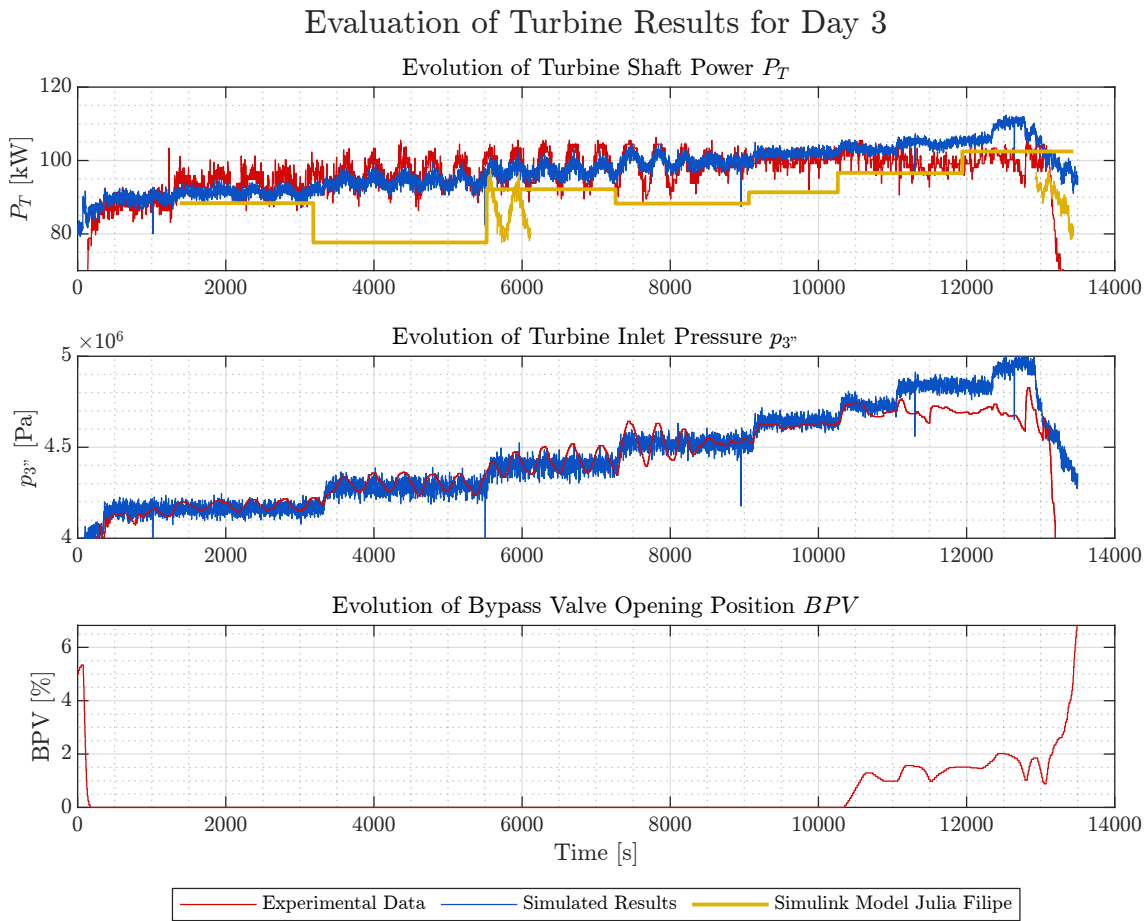


Figure 4.5.: Results of turbine model for Day3. For the turbine shaft power of the Simulink comparison model by Julia Filipe (yellow) both the stationary results and all available transient results are plotted. All plotted data is unfiltered.

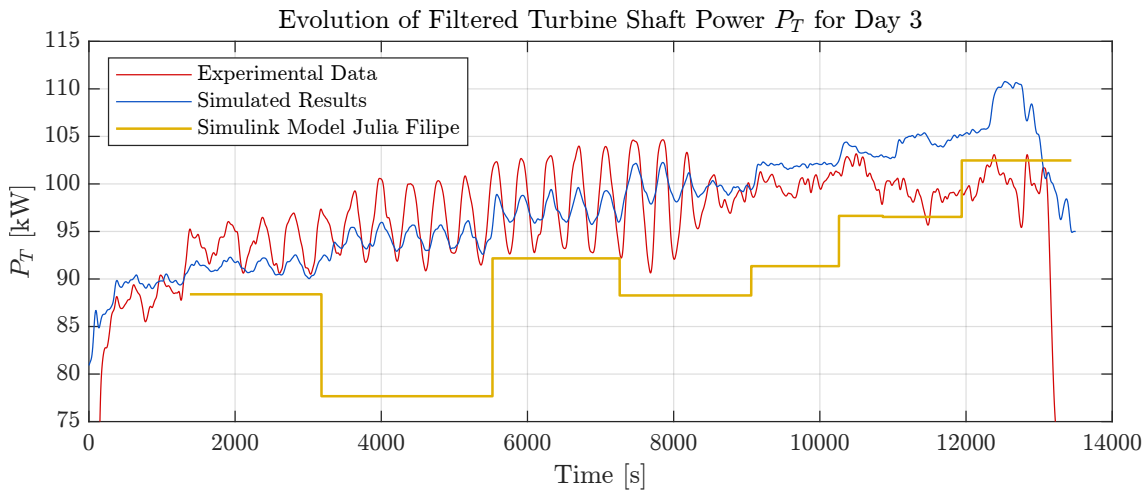


Figure 4.6.: Results of the filtered turbine shaft power for Day3.

4.2. Verification and Validation of the Condenser Model

In order to validate the condenser model, a simulation for Day1-3 is carried out and the results are compared with the experimental data. The outlet enthalpy and outlet temperature of the condenser serve as comparison variables. As noted in Chapter 3.4.3, the condenser model requires a correction factor for the heat transfer correlations to better approximate the experimental data. The correction factor is applied for the correlation of convective heat transfer on ORC side (Shah) and on air side (Haaf). The use of correction factors for the heat transfer correlations is already provided in TIL so that the corresponding factor only has to be entered as a parameter. The factor was determined empirically for Day1. For this data set the model showed good agreement with the experimental data for the correction factors 0.7 and 0.8. Afterwards both factors were tested and validated with the data from Day2 and Day3.

The Dymola models for Day1-3 are summarized in Table 4.3. The results for all simulations are shown in Figures 4.7 to 4.12. A quantification of the deviations from the experimental data for all simulations is summarized in Table 4.4.

MODEL	Day1: C_d1_Nc_1.65 Day2: C_d2_Nc_1.65 Day3: C_d3_Nc_1.65
INPUTS	\dot{m} ; p_1 ; h_4' ; p_{amb} ; T_{amb} ; $rel.hum.$; \dot{V}_{air} ;
RELEVANT OUTPUTS	h_1 ; T_1 ;
CORRELATIONS	Heat Transfer: Shah & Haaf & Schmidt Pressure Loss: Zero-Pressure-Drop & Haaf
NOTE	The Dymola models listed above contain the same condenser model and differ only in the input data. For all models a correction factor for the heat transfer correlations of 0.7 and 0.8 are tested. The input data is filtered and resampled as explained in Chapter 3.4.2.1. The condenser model is discretized with 20 cells in flow direction.

Table 4.3.: Dymola models used for the validation of the condenser model.

In the figures for the temperature curves (Figures 4.8, 4.10, 4.12), the calculated inlet temperature is also shown (purple). This is determined by the model from the inlet enthalpy given as input and the pressure at the condenser inlet. Since the condenser uses a zero-pressure-drop model and the inlet pressure is therefore underestimated, the inlet temperature determined from this is also slightly below the measured values. Overall, however, there is a reasonable qualitative and quantitative approximation of the inlet temperature for all three days.

As can be seen from the figures, the output variables for the selected correction factors are also well approximated. This applies in both qualitative and quantitative terms. The simulations with the correction factor 0.7 deliver somewhat better results. The mean relative deviation for the outlet enthalpy for this factor is $\leq 1.11\%$ for all days. The maximum relative deviation has an outlier at $t = 1419s$ for Day2 but is otherwise below 2.8% for all simulations. More detailed information on the deviations is given in Table 4.4. The summary of the deviations given in table shows that the experimental data are represented somewhat better for a correction factor of 0.7 than for the factor 0.8, which is why the factor 0.7 is used for the coupled model.

As can be seen from the graphs for the enthalpy (Figures 4.7, 4.9, 4.11), the outlet enthalpy for the simulations with the correction factor 0.7 is slightly overestimated for Day1, for Day2 it is very aptly approximated and for Day3 it is slightly underestimated. A possible explanation for this behavior could be a increasing nitrogen concentration in the propane for each new test run. The data situation does not allow a clear conclusion, but this possibility should be kept in mind for further tests with the MoNiKa system.

Comparing the qualitative course of the outlet variables of all days, one observes that Day3 stands out. Here the outlet enthalpy (and outlet temperature) are initially underestimated and from $t \approx 7000$ s the curves converge towards the curves for the experimental data. For the correction factor 0.7, the outlet variables are even slightly overestimated for $t > 9500$ s. In contrast to Day1 and Day2, Day3 does therefore not show a similarly good qualitative representation of the results. A more detailed analysis shows that the course of the measured ambient temperature looks unusual for Day3 and behaves very differently from the courses of Day1 and Day2. Since it did not rain on any of the days and these are consecutive days, this problem is being investigated more closely.

		CORRECTION 0.7			CORRECTION 0.8		
		DAY1	DAY2	DAY3	DAY1	DAY2	DAY3
t_1	[s]	400	500	500	400	500	500
t_n	[s]	15660	14400	13500	15660	14400	13500
$\bar{\epsilon}_{abs}$	[kJ/kg]	2.79	1.36	1.79	2.49	4.30	3.38
$\bar{\epsilon}_{rel}$	[%]	1.11	0.55	0.77	0.99	1.74	1.45
$\epsilon_{abs,max}$	[kJ/kg]	6.89	16.26	3.61	6.36	18.35	5.14
	[s]	731	1419	2894	3170	1419	2894
$\epsilon_{rel,max}$	[%]	2.71	6.36	1.55	2.47	7.17	2.20
	[s]	731	1419	2894	3170	1419	2894

Table 4.4.: Deviations of the condenser outlet enthalpy between the experimental data and the Dymola condenser model with a correction factor of 0.7 and 0.8. t_1 refers to the beginning and t_n to the end of the comparison period. For the maximum values of the deviations, the time of occurrence is also specified.

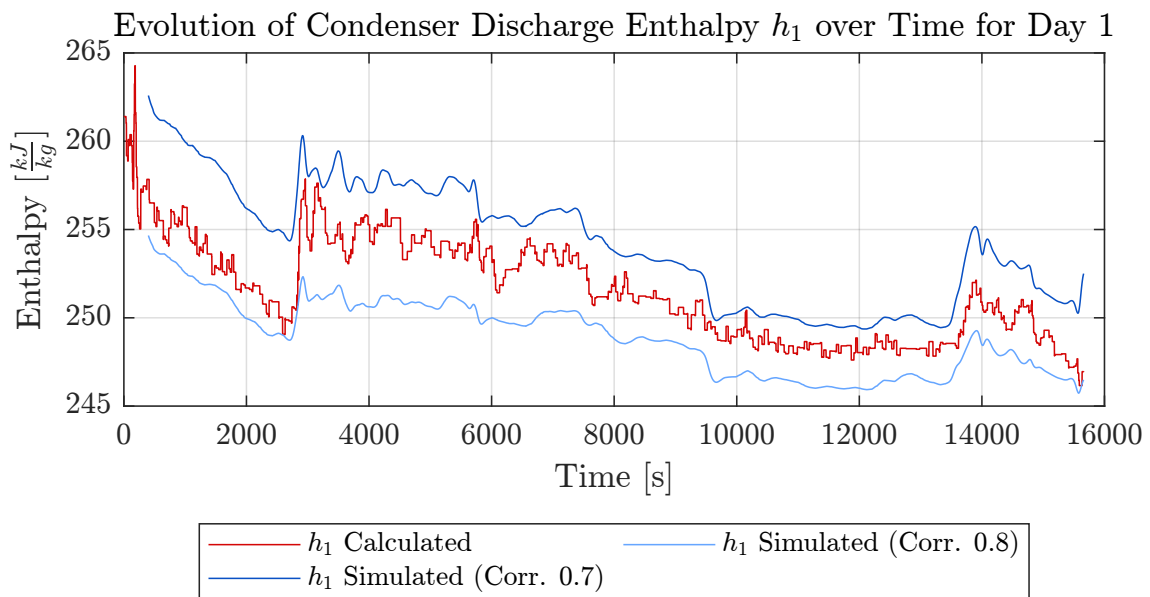


Figure 4.7.: Evolution of Condenser Outlet Enthalpy for Day1.

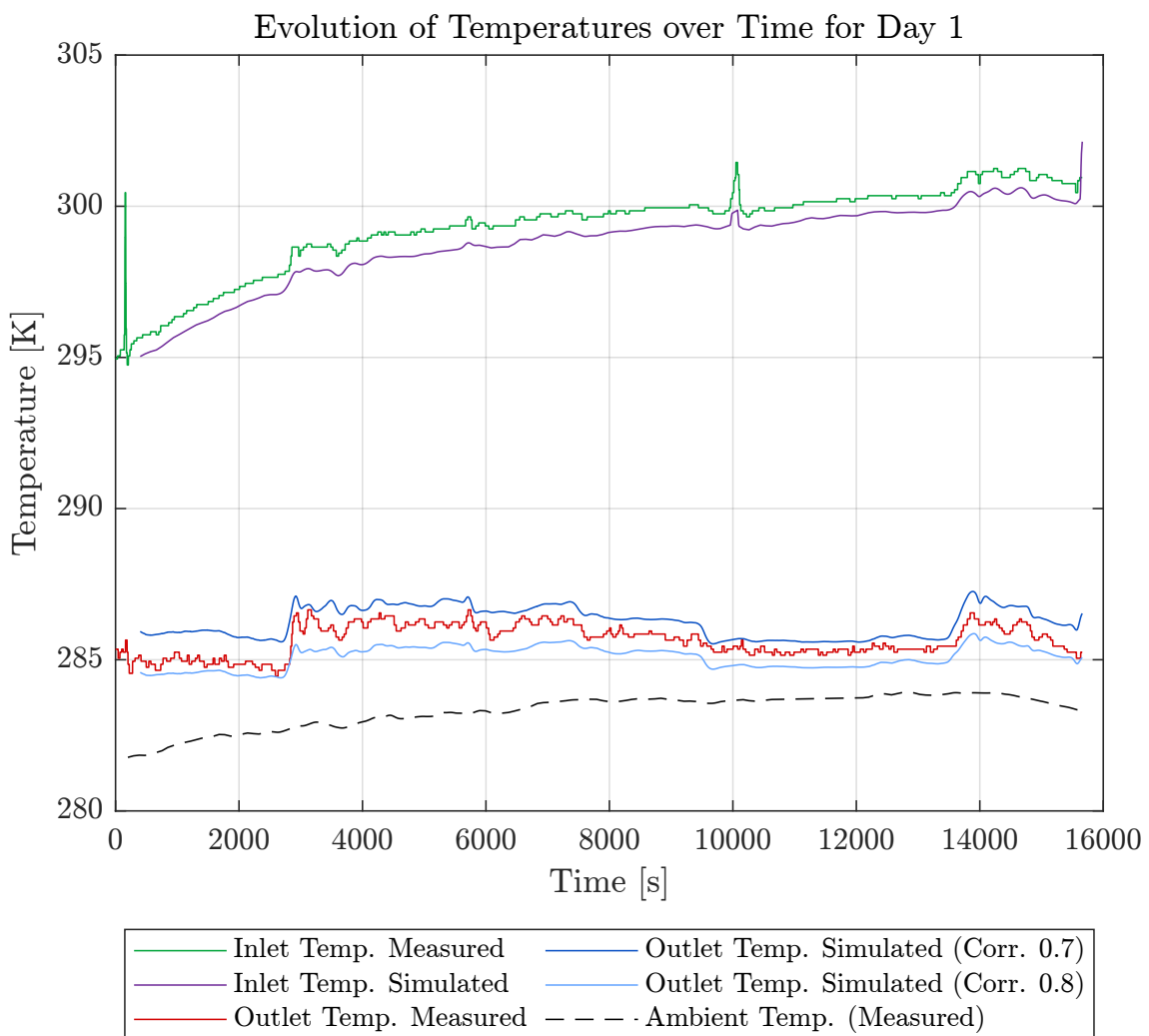


Figure 4.8.: Evolution of Condenser Outlet Temperature for Day1.

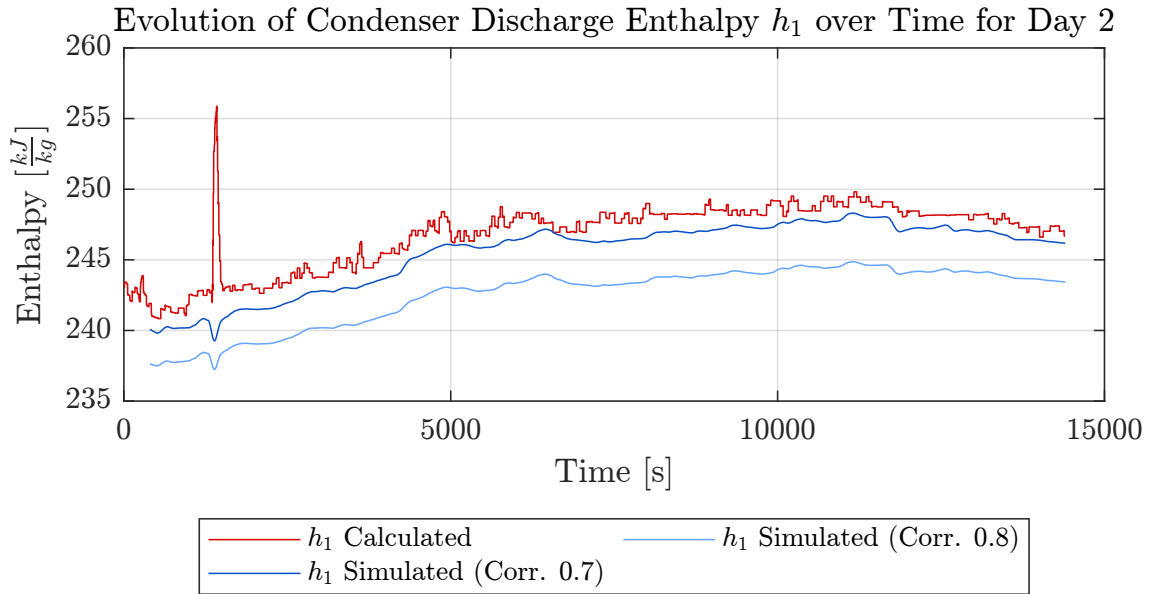


Figure 4.9.: Evolution of Condenser Outlet Enthalpy for Day2.

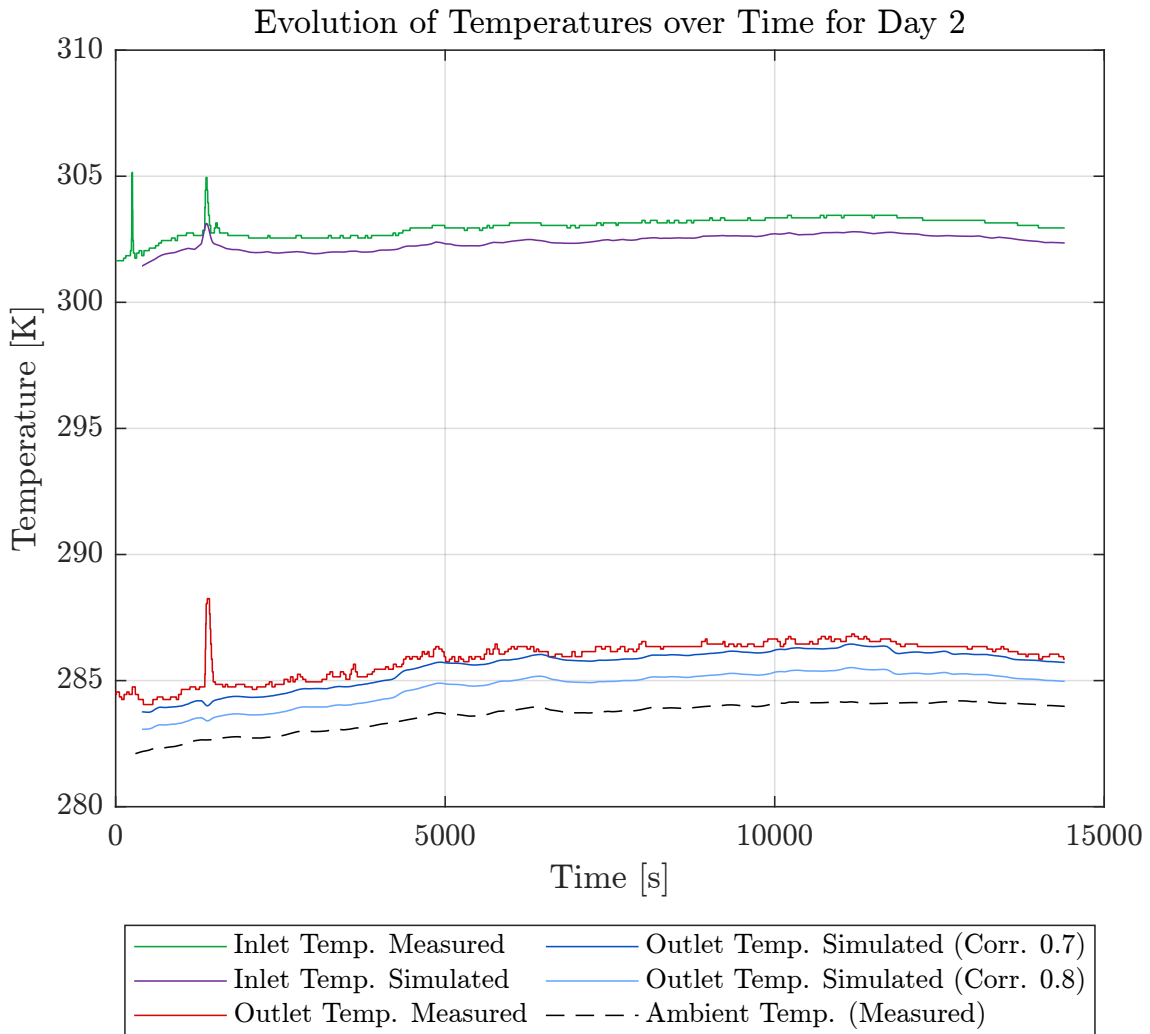


Figure 4.10.: Evolution of Condenser Outlet Temperature for Day2.

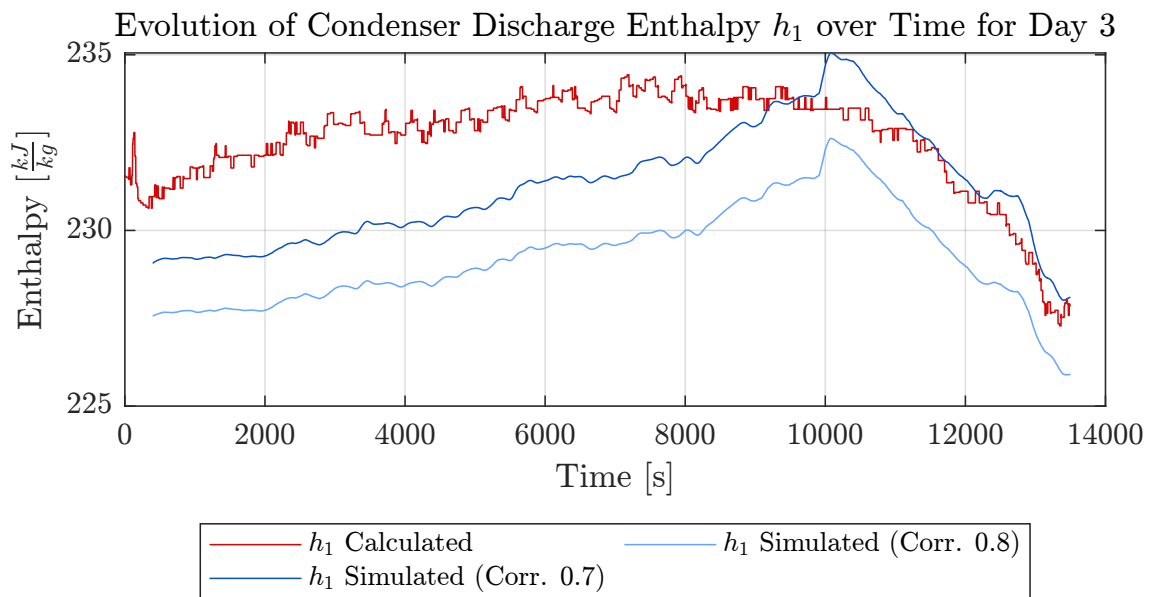


Figure 4.11.: Evolution of Condenser Outlet Enthalpy for Day3.

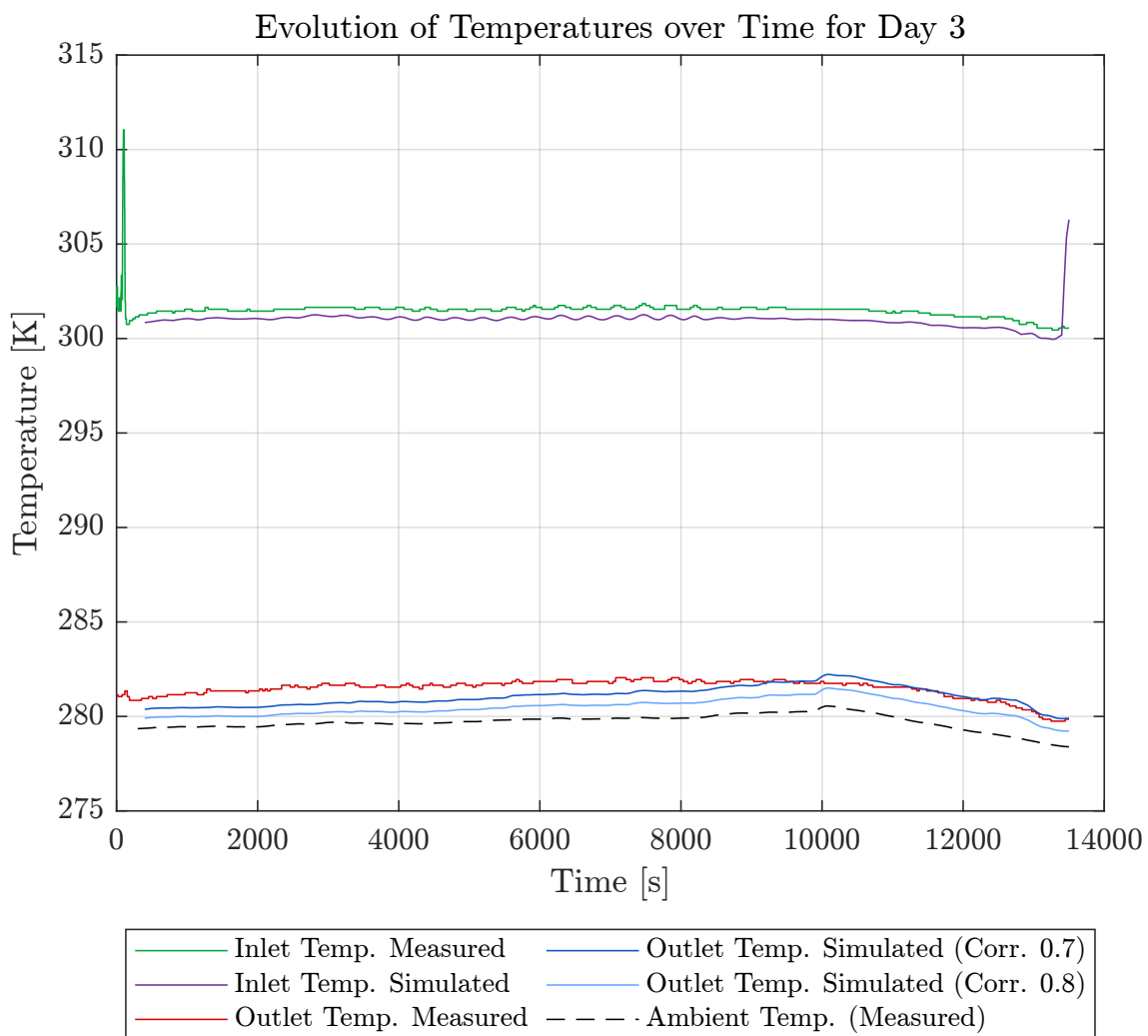


Figure 4.12.: Evolution of Condenser Outlet Temperature for Day3.

Since the course of the ambient temperature for Day3 looks unusual, the measured value is compared with measured data from the weather mast at KIT Campus North². A comparison is shown in Figure 4.13 for the relevant time period of all 3 days. Since the temperature measurement takes place at different locations, it is not to be expected that the measured values will match exactly. However, since it did not rain on any of the days, it can be expected that the qualitative curves of the two measuring devices will be similar. For Day1, Day2 and the first half of the graphic for Day3, the qualitative curves are similar, with the measurement at the MoNiKa system being slightly below the measured value of the Campus North weather mast. For the second half of the period relevant for Day3, however, the curves show a very different behavior, with the measurement at the MoNiKa system even exceeding that of the weather mast.

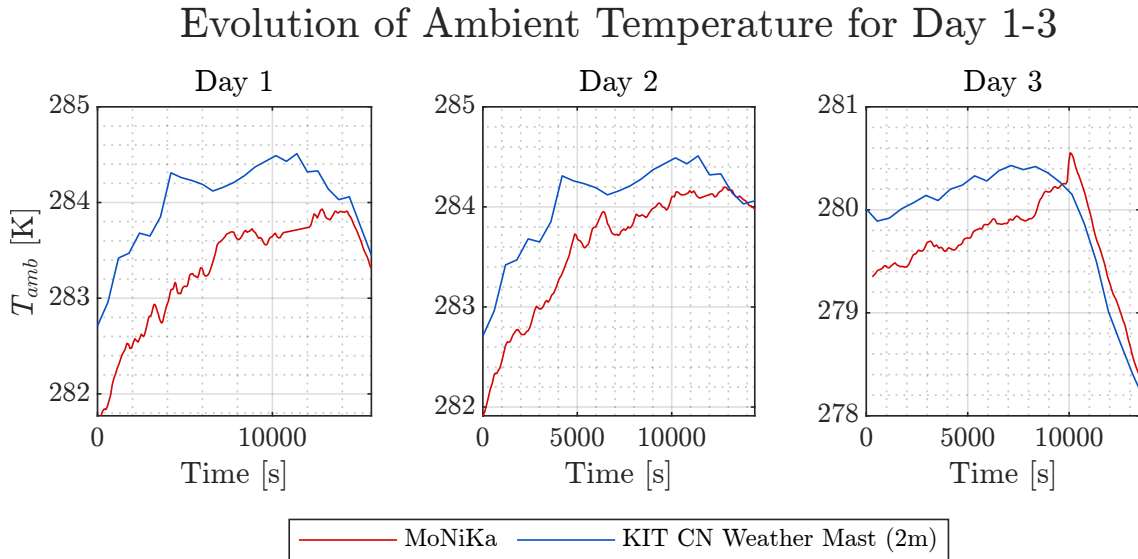


Figure 4.13.: Evolution of Ambient Temperatures of Day 1-3 as measured at the MoNiKa plant (red) and according to the KIT Campus North weather mast at a height of 2m (blue).

To check whether the deviations of the condenser outlet variables for Day3 could be explained by shortcomings in the ambient temperature measurement, the simulation model is executed again, this time using as input the ambient temperature measurement from the weather mast. It is then evaluated whether the qualitative course of the results agrees better with the experimental data.

The results of this simulation are shown in Figure 4.14. As can be seen, the qualitative curve of the outlet temperature (blue dashed line) now agrees significantly better with the experimental data. In quantitative terms, no statement can be made because the measured values from the weather mast were usually higher than those from the MoNiKa systems. However, since the qualitative agreement could be significantly improved, the conclusion must be considered that problems with the MoNiKa sensor for the ambient temperature can occur. One possible explanation for an incorrect temperature measurement could be the ingress of small amounts of liquid into the sensor. A precise analysis is not possible within the scope of this thesis. However, for future MoNiKa test runs this should be kept in mind and the measured value for the ambient temperature should be constantly monitored and validated with comparative measurements.

²The measurement took place at a height of 2m.

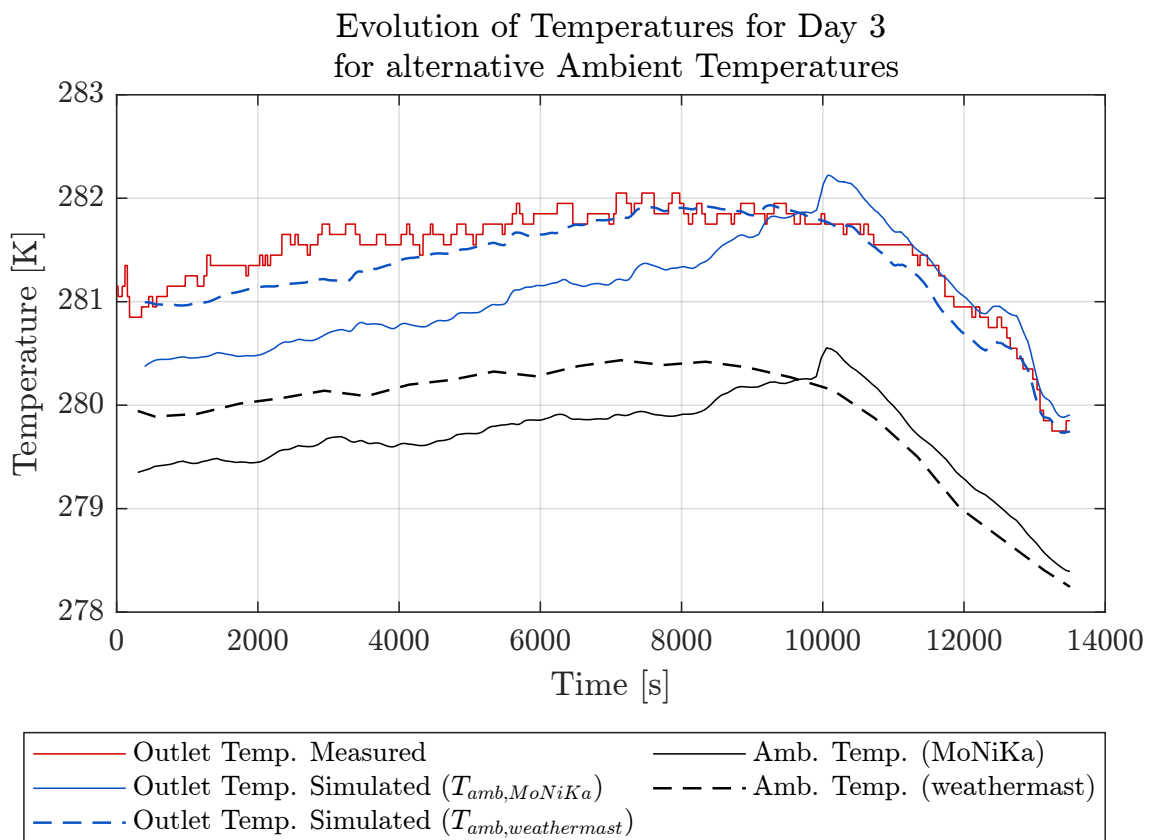


Figure 4.14.: Evolution of condenser outlet temperature for Day 3 with alternative measurement data for the ambient temperature. As a correction factor for the heat transfer correlations 0.7 was used.

4.3. Validation of the Coupled Model

As for the subsystems before, a simulation is carried out for the coupled system for each of the three days and the results are then compared with the experimental data. The models are summarized in Table 4.5. The input data is filtered and resampled as explained in Chapter 3.4.2.1. As in the validation of the turbine model, the experimental data for the turbine shaft power was filtered with a 2nd order Butterworth filter with a cut-off frequency of 0.01 Hz for better comparability. The Matlab-Function used for the filtering is attached in Appendix B.3.

A quantification of the deviations for the turbine shaft power and the condenser outlet enthalpy are shown in Table 4.6.

The Figures 4.15 to 4.20 show the results for turbine shaft power, pressure curves and temperature curves for all three days. The individual variables and their agreement with the experimental data are explained in more detail below.

MODEL	Day1: S_d1_Nc_1_65 Day2: S_d2_Nc_1_65 Day3: S_d3_Nc_1_65
INPUTS	\dot{m} ; \dot{m}_T ; $h_{3''}$; p_1 ; p_{amb} ; T_{amb} ; φ ; \dot{V}_{air} ;
RELEVANT OUTPUTS	P_T ; h_1
CORRELATIONS	Turbine: Efficiency Correlation & Stodola Equation Heat Transfer: Shah & Haaf & Schmidt Pressure Loss: Zero-Pressure-Drop & Haaf
NOTE	The Dymola models listed above contain the same turbine and condenser models and differ only in the input data. All models contain a correction factor of 0.7 for the heat transfer correlations Shah & Haaf. The input data is filtered and resampled as explained in Chapter 3.4.2.1. The condenser model is discretized with 20 cells in flow direction.

Table 4.5.: Dymola models for the validation of the coupled system.

Turbine Shaft Power P_T :

The turbine shaft power for the coupled model gives similar results as the turbine model itself, with the mean deviations being slightly higher. The curves for the experimental turbine power (subplot 1 of Figures 4.15, 4.17 and 4.19) were filtered with a 2nd order Butterworth low-pass filter in order to reduce measurement fluctuations and thus improve clarity. The cutoff frequency of the filter was 0.01 Hz. Since, in contrast to the turbine model, the mass flow input for the coupled model was already filtered, the calculated shaft power did not have to be filtered again. The mean relative deviation is less than 3.7% for all three simulations (see Table 4.6). As for the turbine model, the turbine shaft power of the coupled model shows good agreement with the experimental data whenever the inlet pressure is well approximated. A visible improvement in quality and quantity compared to the existing Simulink turbine model of Julia Filipe [9] could be achieved. A more detailed comparison between the results of the Simulink and Dymola turbine model was given in Table 4.2 in Chapter 4.1.

Turbine Inlet Pressure $p_{3''}$:

The turbine inlet pressure determined using the Stodola equation shows overall good agreement with the measured values, but deviates in operating states with high system pressures

and the bypass valve being open at the same time. See Chapter 4.1 for a more detailed analysis.

Turbine Outlet Pressure p_4 :

The outlet pressure of the turbine, which is determined via the hydraulic resistance with a constant pressure loss coefficient, shows excellent agreement with the experimental data for all simulations. A quantification was already carried out in Chapter 3.5.

Turbine Inlet Temperature $T_{3''}$:

The temperature at the turbine inlet is determined from the enthalpy and the pressure at the inlet and therefore represents the experimental data well if these two variables are well approximated.

Turbine Outlet Temperature T_4 :

The temperature at the turbine outlet shows excellent agreement with the measurements from sensor TI 10-04 for all simulations. The nitrogen content in the MoNiKa cycle was estimated by Prof. Dr. Schulenberg by comparing the pressure and temperature at the turbine outlet. Since the outlet pressure p_4 of the turbine is well approximated, the outlet temperature should inevitably also be well represented. Since this is the case, it can be assumed that the fluid mixture has been implemented correctly.

Condenser Outlet Temperature T_1 :

The temperature at the condenser outlet behaves in a similar way to that explained in Chapter 4.2. For Day1, the calculated temperature is slightly above the measured value, but shows good qualitative agreement. For Day2, the temperature is well represented in qualitative and quantitative terms and for Day3, the temperature is rather underestimated, but the two curves intersect. The qualitative progression for Day3 also agrees less well with the experimental data than it was the case for the previous days. As explained in Chapter 4.2, this could be due to a faulty measurement of the ambient temperature. The ambient temperature measurement as a potential error source should therefore be kept in mind for future analysis.

Condenser Outlet Enthalpy h_1 :

The outlet enthalpy of the condenser behaves in a similar way to the experimental data as the outlet temperature and shows similar curves as already shown in Chapter 4.2. It is therefore not represented graphically again. A quantification of agreement with the experimental data is shown in Table 4.6.

		TURBINE POWER			OUTLET ENTHALPY		
		DAY1	DAY2	DAY3	DAY1	DAY2	DAY3
t_1	[s]	500	500	500	500	500	500
t_n	[s]	15260	14000	13100	15260	14000	13100
$\bar{\epsilon}_{abs}$	[kW] [kJ/kg]	3.22	1.11	2.96	4.73	0.53	1.71
$\bar{\epsilon}_{rel}$	[%]	3.69	1.10	3.03	1.88	0.22	0.74
$\epsilon_{abs,max}$	[kW] [kJ/kg]	25.75	4.98	14.16	10.45	15.57	3.07
	[s]	14075	13922	12747	730	1418	2894
$\epsilon_{rel,max}$	[%]	34.20	4.88	14.82	4.11	6.08	1.32
	[s]	14075	13922	12748	730	1418	2894

Table 4.6.: Deviations of the turbine power or condenser outlet enthalpy between the experimental data and the coupled Dymola model with a correction factor of 0.7 for the condenser. t_1 refers to the beginning and t_n to the end of the comparison period. For the maximum values of the deviations, the time of occurrence is also specified.

Comparison of Turbine Shaft Power and Pressures for Day 1

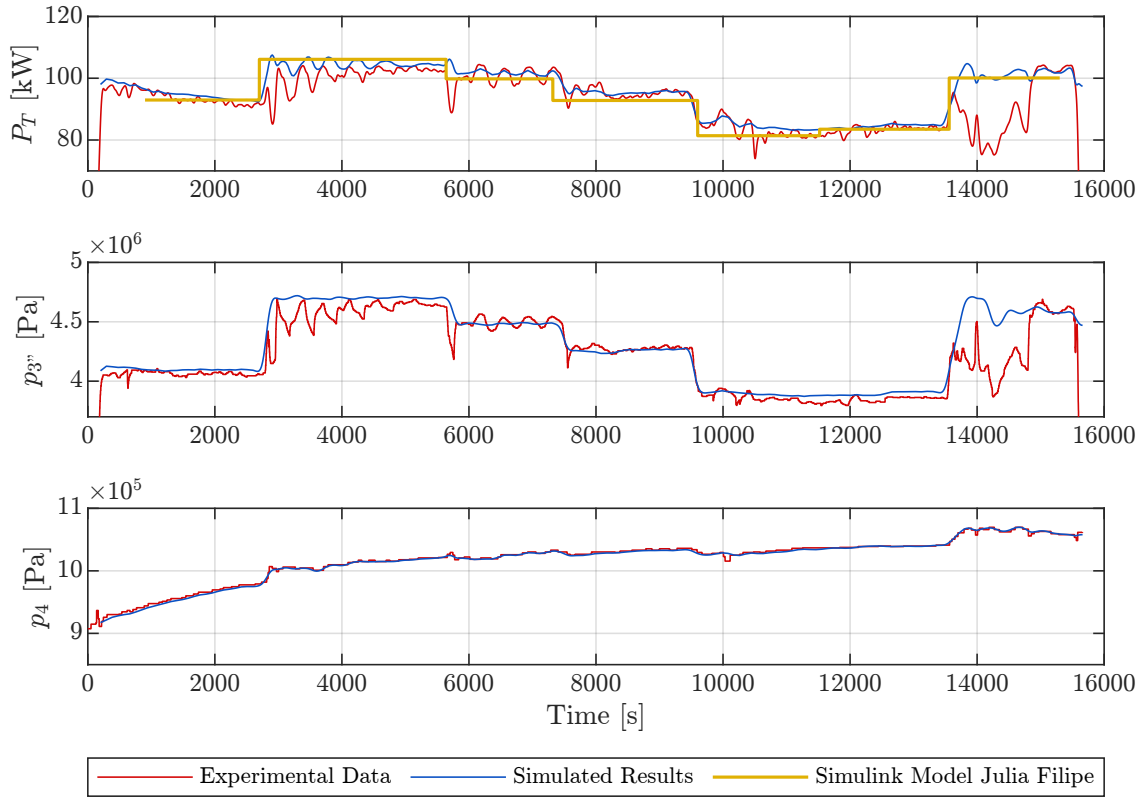


Figure 4.15.: Evolution of turbine shaft power and pressures for the coupled system for Day1.

Comparison of Temperatures for Day 1

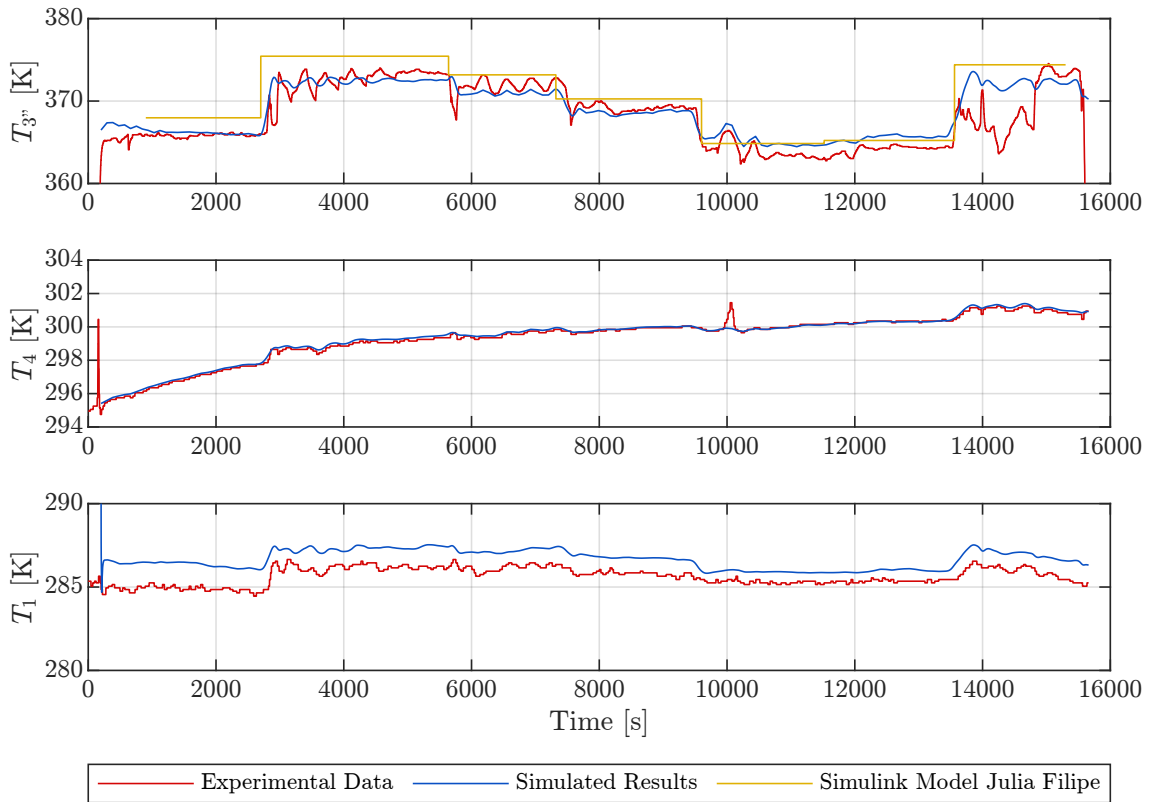


Figure 4.16.: Evolution of temperatures of the coupled system for Day1.

Comparison of Turbine Shaft Power and Pressures for Day 2

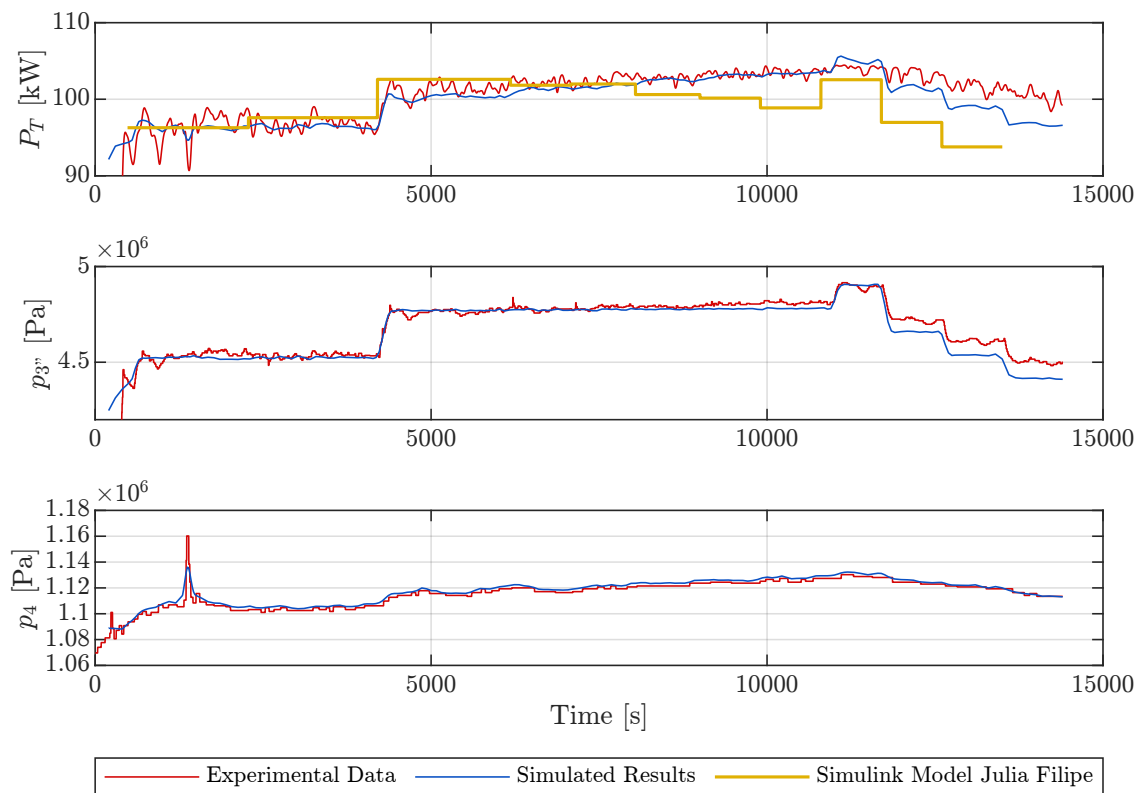


Figure 4.17.: Evolution of turbine shaft power and pressures for the coupled system for Day2.

Comparison of Temperatures for Day 2

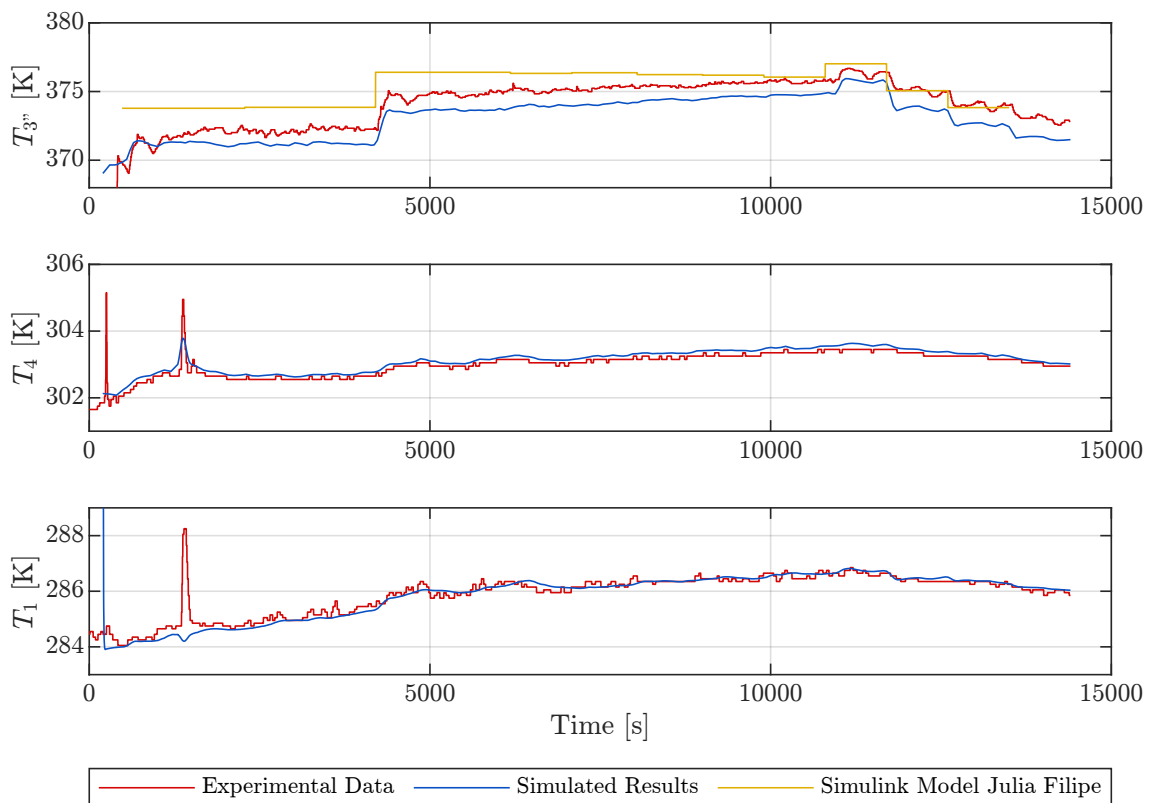


Figure 4.18.: Evolution of temperatures of the coupled system for Day2.

Comparison of Turbine Shaft Power and Pressures for Day 3

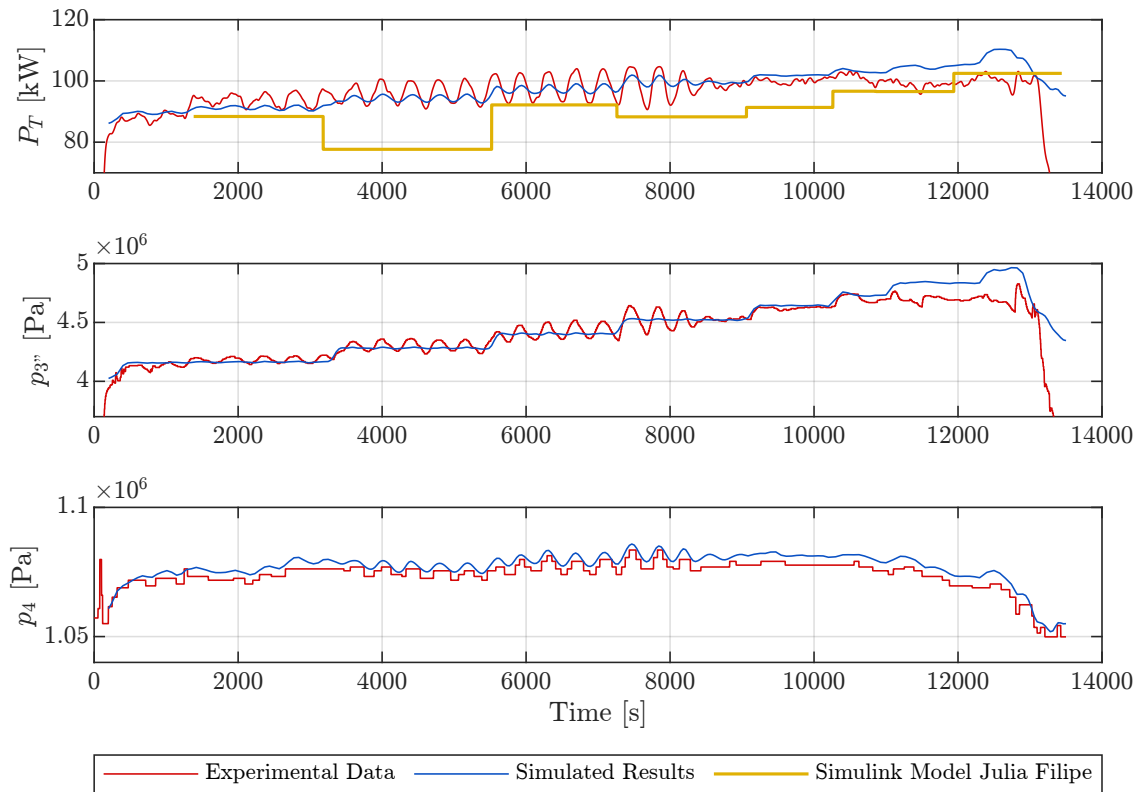


Figure 4.19.: Evolution of turbine shaft power and pressures for the coupled system for Day3.

Comparison of Temperatures for Day 3

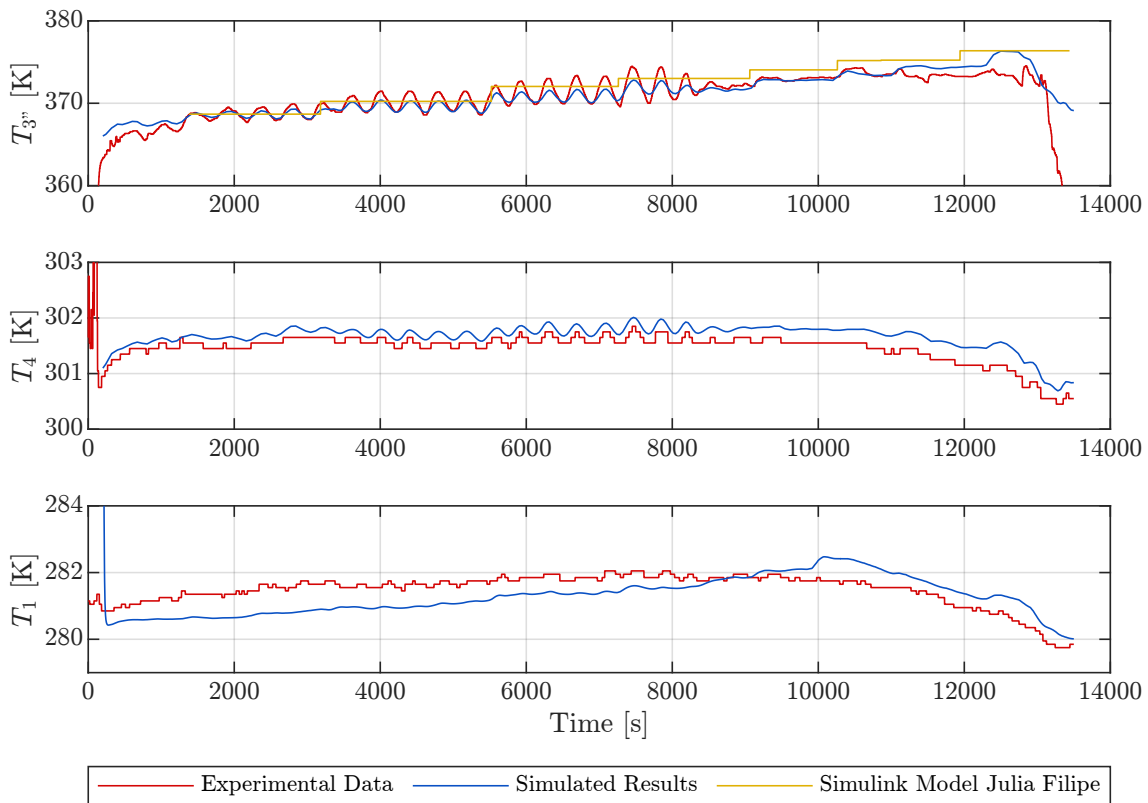


Figure 4.20.: Evolution of temperatures of the coupled system for Day3.

4.4. Sensitivity Study

To evaluate how sensitive the relevant output variables of the coupled system behave to changes in the input parameters, a sensitivity analysis is carried out. For this purpose, the input parameters of the model are systematically varied one after the other and then observed how the turbine shaft power and the outlet enthalpy of the condenser change. The aim of the analysis is to identify critical input parameters which in the future can be used to prioritize data collection efforts (e.g. which sensors should be closely monitored). Furthermore, in combination with Table 2.2, which gives an overview of the measurement accuracy of the individual sensors, the sensitivity study can help to quantify the uncertainties in the output variables due to measurement inaccuracies. This can then be used to identify areas in which additional sensors or sensors with higher accuracy may be needed.

The most obvious choice of a stationary operating point as the basis for the sensitivity analysis would be the design point of the MoNiKa plant. However, since the system never operates at the nominal operating point due to design problems, another operating point must be selected. For this purpose, the stationary operating point of Day2 between 11100s and 11650s after the start of the facility is selected. Several arguments speak in favor of this choice: on the one hand, both the turbine power and the condenser outlet enthalpy for Day2 are well approximated by the model. The selected operating state (11100s < t < 11650s) also has a high ORC mass flow and high turbine power, resulting in an operating point that is relatively close to the design point. Furthermore, for this operating state, the bypass valve is fully closed while the control valve is fully open. Consequently, no additional uncertainties arise due to the not fully known characteristics of the valves. The input parameters for the analysis are then the mean value of the measured parameters in the selected period. Those are summarized in Table 4.7.

Table 4.7.: Selected stationary operating point for the sensitivity analysis.

PARAMETER	SYMBOL	VALUE ¹	RANGE OF VARIATION
ORC Mass Flow	\dot{m}	$2.702 \frac{kg}{s}$	$\pm 5\%$
Turbine Inlet Enthalpy	$h_{3'}$	$607.929 \frac{kJ}{kg}$	$\pm 5\%$
Ambient Temperature	T_{amb}	$284.129K$	$\pm 5\%$
Ambient Pressure	p_{amb}	$1.015bar$	$\pm 5\%$
Relative humidity	φ	52.768%	$\pm 5\%$
Condenser Outlet Pressure	p_1	$11.081bar$	$\pm 5\%$
Volume Flow Cooling Air	\dot{V}_{air}	$146.667 \frac{m^3}{s}$	$\pm 5\%$

¹ Mean value in the selected range (11100s < t < 11650s) for Day2.

The sensitivity analysis is performed by first providing the model with the inputs specified in Table 4.7. The inputs are initially kept constant until the model reaches a steady operating state. The stationary turbine shaft power and condenser outlet enthalpy are now determined to later dedimensionalize the results. During stationary operation, the turbine shaft power of the model was 105.14kW and the condenser output enthalpy was $248.15 \frac{kJ}{kg}$.

Next, the first parameter is reduced by 5% while the others are held constant. The inputs are then kept constant until a new stationary state is established. Then the actual

sensitivity analysis begins, in which the reduced parameter is now slowly varied linearly from -5% to +5% of its stationary value. The parameter is then reset to its initial value and the procedure is repeated for the next parameter.

Since the tubes in the condenser have a heat capacity and the VLE-Fluid cells take compressibility into account, it is important not to vary the individual parameters too quickly. The variation from -5% to +5% of the stationary parameter value is realized over a simulation period of one hour. The simulation is then repeated with a variation period of 2 hours. The results of both simulations are then compared to check if the variation took place slowly enough. The maximum relative deviation between the two simulations was 0.21% for the outlet enthalpy of the condenser when the ambient temperature varied. The maximum relative deviation for all other varied parameters was significantly lower ($\leq 0.0067\%$) for both turbine power and condenser outlet enthalpy. From this it can be concluded that the variation of the parameters took place sufficiently slowly.

The results of the sensitivity study are shown in Figure 4.21. The variation of the turbine power (δ_{P_T}) and the variation of the condenser outlet enthalpy (δ_{h_1}) were plotted against the variation of the input parameters (δ_{Input}). The results are discussed below.

Sensitivity Study for Coupled Model

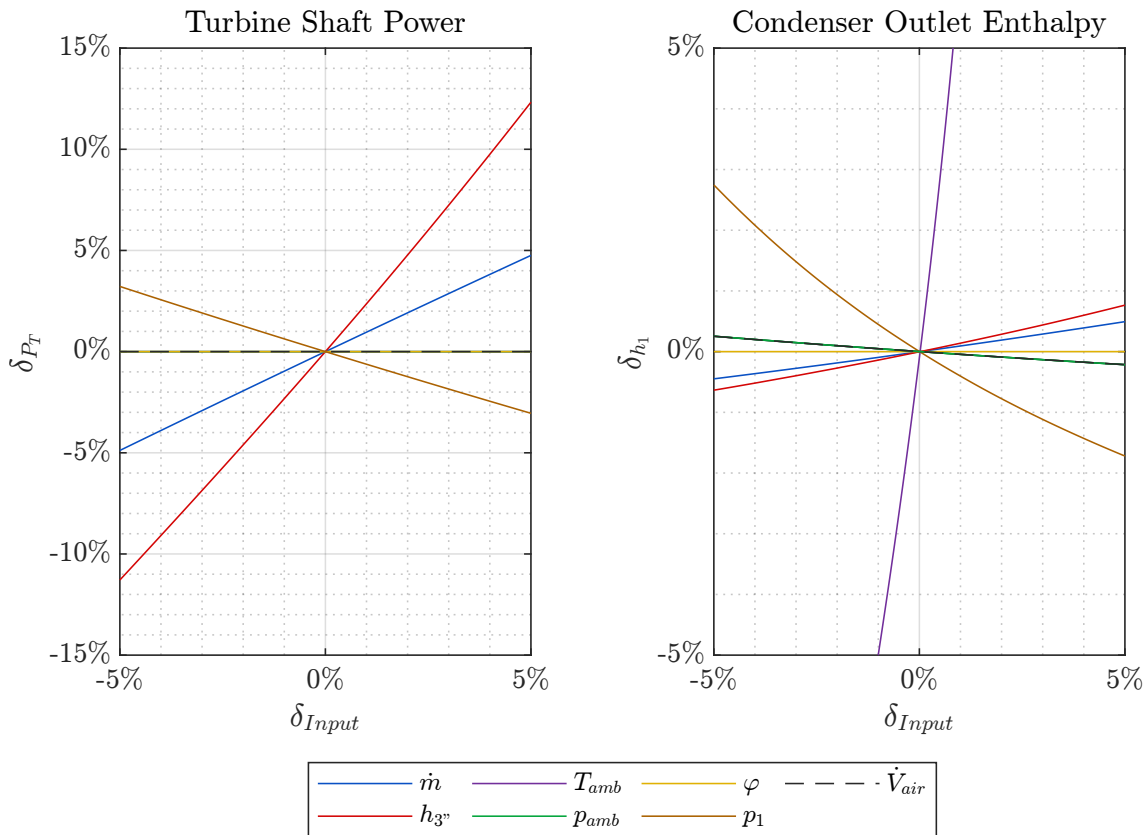


Figure 4.21.: Sensitivity Study for the coupled system. The variation of the individual input parameters is plotted on the x-axis. The resulting variation of the output variables is plotted on the y-axis. All parameters and variables were dedimensionalized for better comparability with their stationary value.

Turbine Shaft Power:

A variation of the input enthalpy $h_{3''}$ had the strongest influence on the turbine shaft power. This is not surprising since higher inlet enthalpy increases the enthalpy drop across the turbine, resulting in increased turbine power. A variation in mass flow resulted in an approximately proportional variation in turbine power, which was also to be expected. An

increase in the condenser pressure led to a reduction in the turbine output, which can be attributed to a reduction in the enthalpy drop in the turbine.

The variation of all other parameters had no influence on the turbine power. It must be pointed out here that the sensitivity analysis is based on the Dymola model and not on the real MoNiKa system. In the real system, for example, it would be expected that an increased flow of cooling air would lead to a reduction in the condenser temperature and thus to a reduction in the condenser pressure. This in turn would then lead to an increased turbine power. The reason why this behavior is not observed in the Dymola model is that the condenser pressure is a parameter of the model and so far does not result from the condensation temperature as in the real system. This property could not be implemented in the software used within the time frame of the thesis.

Condenser Outlet Enthalpy:

A very strong influence of the ambient temperature was found for the outlet enthalpy of the condenser. Here the problem of the condenser pressure specified as input becomes clear again: In the real system it is to be expected that an increase in the ambient temperature leads to an increase in the condenser temperature. This in turn then results in an increased condenser pressure. However, since the pressure is specified in the model, the state point shifts on this isobar when the temperature increases. This then results in a strong increase in enthalpy. Since temperature and pressure in the two-phase region are generally not independent of one another, this problem also occurs when the condenser pressure is varied.

A variation of the mass flow and the turbine inlet enthalpy each led to a slight increase in the outlet enthalpy. An increase in the cooling air flow and the ambient pressure each led to a slight reduction of the outlet enthalpy. The two curves are very close together in the diagram. To improve the visibility the curve for the volume flow of the cooling air is therefore plotted as a dashed line.

A variation in relative humidity resulted in only a negligible variation in the condenser outlet enthalpy. The material properties of moist air change only very slightly with a 5% variation in air humidity. For the operating conditions of the sensitivity study neither condensation nor evaporation of water on the fins occurred and thus, the variation in humidity has no significant effect. However, the MoNiKa condenser can optionally be operated with an additional water injection onto the heat exchanger fins. In this case, the relative humidity would be decisive, since evaporation would be accelerated for drier air, which would then lead to a higher heat flow being dissipated due to the evaporative cooling.

Finally, it can be stated that for the current Dymola model, the measured value for the ambient temperature in particular has a critical influence on the condenser outlet enthalpy. In the case of the turbine, it is primarily the inlet enthalpy $h_{3''}$ that has a strong influence on the shaft power.

It should be noted that in the sensitivity study all input parameters were varied by 5%. In the case of the mass flow, this corresponds to a variation of $0.135 \frac{kg}{s}$. Such a variation can be far exceeded in normal MoNiKa operation. For the ambient temperature, on the other hand, a 5% variation corresponds to 14.206 Kelvin, which is a much less likely event and does not occur within a short period of time during normal operation. Such considerations should be taken into account when reading the graphs.

5. Summary and Conclusion

The aim of this thesis was the development of a coupled MoNiKa turbine-condenser model in Dymola, the comparison with previous Simulink models ([11],[9]) and the subsequent validation of the model using experimental data.

The developed model is capable of providing close approximations of turbine shaft power and condenser output variables over a wide operating range of the MoNiKa plant. The main findings of the study, a brief interpretation of the results, the limitations of the model and potential improvements are briefly discussed below.

Achievements and main findings of the study

Within the scope of this thesis, a new empirical efficiency correlation of the MoNiKa turbine was developed and implemented into the turbine model. It takes into account current knowledge about the nitrogen content in the MoNiKa ORC fluid and is capable of accurately predicting the turbine shaft power over a wide range of operating conditions. The developed turbine model is capable of providing accurate approximations of the shaft power for stationary and quickly changing operating conditions and furthermore allows a continuous simulation over long test periods, which was previously only possible for significantly smaller time periods.

The condenser model now allows the use of fluid mixtures and enables a transient simulation over long test periods. In addition, compared to the previous model, the model no longer requires as input the measured outlet temperature of the cooling air, which is unknown in advance. With a grid study, the required number of cells for the discretization of the condenser in flow direction could be determined to 20. The expected discretization error for this number of cells was estimated to be $\leq 0.8\%$ using the Grid Convergence Index.

A significant increase in computation time by an order of magnitude was observed when using fluid mixtures instead of pure substances as ORC working medium. By filtering and resampling the measured data, the simulation time could be significantly reduced and thus the applicability of the models improved. In addition, the influence of different pressure loss models on the condenser output variables and computing time was examined. The evaluation of the results showed that the use of complex, computationally intensive pressure drop models in the MoNiKa condenser had only a marginal influence on the heat transfer and not necessarily provided an improved approximation of the pressure loss compared to much simpler models.

It could be observed that the sensor for the ambient temperature showed an unusual behavior during some time periods. The measured ambient temperature should therefore be closely monitored in the future and constantly validated with reference measurements.

An improvement compared to the previous Simulink models is the possibility of coupling the turbine and condenser model. For this purpose, the pressure loss occurring between the turbine and condenser was also modeled. The coupled turbine-condenser model enables a simulation over long test periods with a reasonable simulation runtime and showed good agreement with the experimental data.

The influence of individual input parameters on the output variables of the coupled model could be determined by means of a sensitivity study. This showed that the measured ambient temperature in particular had a major influence on the condenser output enthalpy while the turbine power was most sensitive to the turbine inlet enthalpy.

Interpretation of the results

The experimental data was reliably approximated by the coupled turbine-condenser model for all three investigated MoNiKa test runs.

For the first examined MoNiKa test run, which was carried out at 08.11.2021 over a operation period of 4h, the turbine power was reproduced by the Dymola turbine model with an average relative deviation of 3.50% (compared to 4.41% in the previous Simulink model). For the second 4h test run from 09.11.2021, the average relative deviation was 1.15% (2.42% for the previous Simulink model) and for the third test run (4h operation from 10.11.2021), the average relative deviation of the turbine power could be improved from 8.78% in the previous Simulink model to 3.04%. The qualitative progression of the curves also showed an improved agreement with the experimental data compared to the previous Simulink model.

For the condenser model, no data from comparative models are available for the three MoNiKa test runs mentioned. The specific condenser discharge enthalpy could be reproduced with an average relative deviation from the experimental data of 1.11% (first test run), 0.55% (second test run) and 0.77% (third test run). The condenser model includes a constant correction factor of 0.7 for the heat transfer correlations on the ORC and air side.

The coupled turbine-condenser model showed a similarly good approximation of the turbine power and condenser discharge enthalpy as the single turbine or condenser model.

Limitations of the model and further improvement potentials

The turbine shaft power showed good agreement with the experimental data whenever the input pressure was well approximated. This is determined by the turbine model via a modified Stodola approach. The determination of the inlet pressure showed weaknesses during bypass operation for high system pressures. It is assumed that this is due to deviations in the determination of the bypass mass flow. A possible solution to the problem is to model the bypass and control valve, which can then be integrated into the overall model. However, this requires a complex validation because no measurement data is available for the turbine and bypass mass flow due to a defective mass flow sensor. Therefore, the validation must be carried out via the resulting turbine inlet pressure.

The turbine model is based on fitted empirical correlations and is not in itself a transient model since it has neither a finite volume approach nor a heat capacity. Compressibility and thermal inertia are therefore not considered, which makes the model unsuitable for transient simulation during high-frequency changes in operating conditions.

The condenser model developed so far uses the full-load cooling air flow and was modeled without additional water injection. These conditions were applicable for all test runs investigated, but must be supplemented for a more generally applicable condenser model. Furthermore, the condenser model uses a correction factor for the heat transfer correlations. The validity of the factor should be tested for varying cooling air flows.

Like the previous Simulink condenser model, the Dymola condenser model requires the measured outlet pressure as an input parameter. However, in a real system, the condenser pressure results from the condensation temperature and is therefore not known beforehand.

The models were developed using a propane-nitrogen mixture with 1.65 mass% nitrogen as the working fluid. With the current nitrogen-sealed turbine, it can be assumed that the nitrogen content in the ORC fluid will increase in the long term. This possibility should be considered for future investigations. It may then be necessary to adjust correlations or correction factors.

Outlook on possible future research

Within the scope of the master thesis, a first step towards modeling the MoNiKa plant in Dymola could be made. First knowledge in Dymola and TIL could be gained which can facilitate the further extension of the cycle during future theses.

Next steps could be the modeling of the cooling air fans with the help of the fan performance curve, as well as an extension of the condenser model to include water injection. Furthermore, bypass and control valves could be added to the coupled overall model.

In further developments, the circuit could then be closed by adding a feed pump, heat exchanger and tank, which would then allow simulations for the entire MoNiKa system. As the number of components increases, further considerations for reducing the computing time will likely become necessary.

Bibliography

- [1] Hans Dieter Baehr and Stephan Kabelac. *Thermodynamik*. Springer Berlin Heidelberg, Berlin, Heidelberg, 2016. ISBN 978-3-662-49567-4. doi: 10.1007/978-3-662-49568-1.
- [2] Hans Dieter Baehr and Karl Stephan. *Wärme- und Stoffübertragung*. Springer Berlin Heidelberg, Berlin, Heidelberg, 10. auflage 2019 edition, 2019. ISBN 978-3-662-58441-5.
- [3] BP p.l.c. bp Statistical Review of World Energy 2022: 71st edition. Accessed on 14.11.2022, Available at:. URL <https://www.bp.com/en/global/corporate/energy-economics/statistical-review-of-world-energy.html>.
- [4] Dag Brück, Hilding Elmqvist, Sven Erik Mattsson, and Hans Olsson, editors. *Dymola for Multi-Engineering Modeling and Simulation*, 2002. Accessed on 06.01.2023, Available at:. URL https://modelica.org/events/Conference2002/papers/p07_Brueck.pdf.
- [5] Allan P. Colburn. A method of correlating forced convection heat-transfer data and a comparison with fluid friction. *International Journal of Heat and Mass Transfer*, 7 (12):1359–1384, 1964. ISSN 00179310. doi: 10.1016/0017-9310(64)90125-5.
- [6] Dynasim AB. Dymola - User Manual: Volume 2, 2010.
- [7] Dynasim AB. Dymola - User Manual: Volume 1, 2010.
- [8] Joel H. Ferziger and Milovan Peric. *Numerische Strömungsmechanik*. Springer Berlin Heidelberg, Berlin, Heidelberg, 2008. ISBN 978-3-540-67586-0. doi: 10.1007/978-3-540-68228-8.
- [9] Julia Filipe. Design of a MONIKA-ORC-turbine model in Simulink and comparison with experimental results: Master Thesis, 2022.
- [10] Felix Flohr. D4.1 Thermophysikalische Stoffwerte gebräuchlicher Kältemittel. In Peter Stephan, Stephan Kabelac, Matthias Kind, Dieter Mewes, Karlheinz Schaber, and Thomas Wetzel, editors, *VDI-Wärmeatlas*, Springer Reference Technik, pages 511–530. Springer Berlin Heidelberg, Berlin, Heidelberg, 2019. ISBN 978-3-662-52988-1. doi: 10.1007/978-3-662-52989-8_22.
- [11] Mariano Fossati. Transient Simulation and Validation of a Condenser for a Supercritical Organic Rankine Cycle: Master Thesis, 2020.
- [12] Lutz Friedel. Druckabfall bei der Strömung von Gas/Dampf-Flüssigkeits-Gemischen in Rohren. *Chemie Ingenieur Technik*, 50(3):167–180, 1978. ISSN 0009286X. doi: 10.1002/cite.330500304.

- [13] Lutz Friedel. Improved friction pressure drop correlation for horizontal and vertical two-phase pipe flow. *Proc. of European Two-Phase Flow Group Meet., Ispra, Italy, 1979*, 1979.
- [14] Peter Fritzson. *Principles of object-oriented modeling and simulation with Modelica 2*. IEEE Press, Piscataway, N.J., 2004. ISBN 9780470545669.
- [15] Volker Gnielinski. Neue Gleichungen für den Wärme- und den Stoffübergang in turbulent durchströmten Rohren und Kanälen. *Forschung im Ingenieurwesen*, 41(1):8–16, 1975. ISSN 0015-7899. doi: 10.1007/BF02559682.
- [16] Ernst Huenges, editor. *Geothermal Energy Systems: Exploration, Development, and Utilization*. Wiley-VCH, Weinheim, 1., auflage edition, 2011. ISBN 9783527630479.
- [17] International Energy Agency. Technology Roadmap: Geothermal Heat and Power, 2011. Accessed on 15.12.2022, Available at: URL <https://www.iea.org/reports/technology-roadmap-geothermal-heat-and-power>.
- [18] International Energy Agency. Net Zero by 2050: A Roadmap for the Global Energy Sector: Revised version, October 2021 (4th revision), 2021. Accessed on 10.12.2022, Available at: URL <https://www.iea.org/reports/net-zero-by-2050>.
- [19] International Energy Agency. World Energy Outlook 2022, 2022. Accessed on 08.12.2022, Available at: URL <https://www.iea.org/reports/world-energy-outlook-2022>.
- [20] Ronald W. James and Terry C. Welch. Refrigeration and Heat-Pump Systems. In Roger Legg, editor, *Air Conditioning System Design*, pages 167–189. Elsevier, 2017. ISBN 9780081011232. doi: 10.1016/B978-0-08-101123-2.00009-1.
- [21] Martin Kaltschmitt, Wolfgang Streicher, and Andreas Wiese. *Erneuerbare Energien: Systemtechnik · Wirtschaftlichkeit · Umweltaspekte*. Springer Berlin / Heidelberg, Berlin, Heidelberg, 6th ed. edition, 2021. ISBN 978-3-662-61190-6.
- [22] J. Kestin. Ein Beitrag zu Stodolas Kegelgesetz. *Wärme- und Stoffübertragung*, 16(1): 53–55, 1982. ISSN 0042-9929. doi: 10.1007/BF01322806.
- [23] Matthias Kind. A2 Dimensionslose Kenngrößen für die Berechnung von Wärmeübertragern und wärmetechnischen Apparaten. In Peter Stephan, Stephan Kabelac, Matthias Kind, Dieter Mewes, Karlheinz Schaber, and Thomas Wetzels, editors, *VDI-Wärmeatlas*, Springer Reference Technik, pages 11–14. Springer Berlin Heidelberg, Berlin, Heidelberg, 2019. ISBN 978-3-662-52988-1. doi: 10.1007/978-3-662-52989-8_2.
- [24] P. Konakov. Eine neue Formel für den Reibungskoeffizienten glatter Rohre. *Berichte der Akademie der Wissenschaften der UDSSR*, 7:503–506, 1946.
- [25] KTK Kühlturm Technologie GmbH. MoNiKa Condenser: Verfahrens- und Anlagenbeschreibung, 2015.
- [26] Roger Legg, editor. *Air Conditioning System Design*. Elsevier, 1st edition edition, 2017. ISBN 9780081011232.
- [27] Eric Lemmon, Ian H. Bell, Marcia L. Huber, and Mark O. McLinden. NIST Standard Reference Database 23: Reference Fluid Thermodynamic and Transport Properties-REFPROP, Version 10.0, National Institute of Standards and Technology, 2018. URL <https://www.nist.gov/srd/refprop>.

- [28] Joaquín Mardon Pérez. Experimental examination of the MONIKA-ORC-Turbine and comparison of the results with thermodynamical calculation: Master Thesis, 2022.
- [29] MATLAB. Butterworth filter design - MATLAB butter, R2022a. Accessed on 03.01.2023, Available at: URL <https://www.mathworks.com/help/signal/ref/butter.html>.
- [30] M+M Turbinen-Technik. Turbine datasheet - Betriebshandbuch: Turbinenanlage Propanexpander (Projekt 1 15 3514 0).
- [31] nasa.gov. Examining Spatial (Grid) Convergence. Accessed on 17.11.2022, Available at: URL <https://www.grc.nasa.gov/WWW/wind/valid/tutorial/spatconv.html>.
- [32] Hermann Nirschl. L1.2 Druckverlust in durchströmten Rohren. In Peter Stephan, Stephan Kabelac, Matthias Kind, Dieter Mewes, Karlheinz Schaber, and Thomas Wetzel, editors, *VDI-Wärmeatlas*, Springer Reference Technik, pages 1355–1361. Springer Berlin Heidelberg, Berlin, Heidelberg, 2019. ISBN 978-3-662-52988-1. doi: 10.1007/978-3-662-52989-8_75.
- [33] Hermann Nirschl. L1.1 Druckverlust in einphasigen Strömungen. In Peter Stephan, Stephan Kabelac, Matthias Kind, Dieter Mewes, Karlheinz Schaber, and Thomas Wetzel, editors, *VDI-Wärmeatlas*, Springer Reference Technik, pages 1353–1354. Springer Berlin Heidelberg, Berlin, Heidelberg, 2019. ISBN 978-3-662-52988-1. doi: 10.1007/978-3-662-52989-8_74.
- [34] OpenModelica User’s Guide. Solving Modelica Models: Integration Methods. Accessed on 11.02.2023, Available at: URL <https://openmodelica.org/doc/OpenModelicaUsersGuide/latest/solving.html>.
- [35] Martin Otter and Hilding Elmqvist. Modelica: Language, Libraries, Tools, Workshop and EU-Project RealSim, 2001. Accessed on 15.02.2023, Available at: URL <https://modelica.org/documents/ModelicaOverview14.pdf>.
- [36] L. R. Petzold, editor. *Description of DASSL: a differential/algebraic system solver*, 1982.
- [37] Henry N. Pollack, Suzanne J. Hurter, and Jeffrey R. Johnson. Heat flow from the Earth’s interior: Analysis of the global data set. *Reviews of Geophysics*, 31(3):267, 1993. ISSN 8755-1209. doi: 10.1029/93RG01249.
- [38] Lewis Fry Richardson. IX. the approximate arithmetical solution by finite differences of physical problems involving differential equations, with an application to the stresses in a masonry dam. *Philosophical Transactions of the Royal Society of London. Series A, Containing Papers of a Mathematical or Physical Character*, 210(459-470):307–357, 1911. ISSN 0264-3952. doi: 10.1098/rsta.1911.0009.
- [39] Christoph Richter. *Proposal of New Object-Oriented Equation-Based Model Libraries for Thermodynamic Systems*. PhD thesis, Universitätsbibliothek Braunschweig, 2008.
- [40] Patrick J. Roache. *Verification and validation in computational science and engineering*. Hermosa, Albuquerque, N.M., 1998. ISBN 978-0913478080.
- [41] Wilfried Roetzel and Bernhard Spang. C1 Wärmeträger: Berechnungsmethoden. In Peter Stephan, Stephan Kabelac, Matthias Kind, Dieter Mewes, Karlheinz Schaber, and Thomas Wetzel, editors, *VDI-Wärmeatlas*, Springer Reference Technik, pages 39–78. Springer Berlin Heidelberg, Berlin, Heidelberg, 2019. ISBN 978-3-662-52988-1. doi: 10.1007/978-3-662-52989-8_5.

- [42] T. E. Schmidt. Heat transfer calculations for extended surfaces. *Refrigerating Engineering*, 57(4):351–357, 1949.
- [43] M. M. Shah. A general correlation for heat transfer during film condensation inside pipes. *International Journal of Heat and Mass Transfer*, 22(4):547–556, 1979. ISSN 00179310. doi: 10.1016/0017-9310(79)90058-9.
- [44] M. M. Shah. An Improved and Extended General Correlation for Heat Transfer During Condensation in Plain Tubes. *HVAC&R Research*, 15(5):889–913, 2009. ISSN 1078-9669. doi: 10.1080/10789669.2009.10390871.
- [45] M. M. Shah. General correlation for heat transfer during condensation in plain tubes: further development and verification. *ASHRAE Transactions*, 119, no. 2:3+, 2013.
- [46] Herbert Sigloch. *Strömungsmaschinen: Grundlagen und Anwendungen*. Hanser eLibrary. Hanser, München, 5. auflage edition, 2013. ISBN 978-3-446-43658-9.
- [47] Roland Span. D2.3 Thermophysikalische Stoffwerte von Stickstoff. In Peter Stephan, Stephan Kabelac, Matthias Kind, Dieter Mewes, Karlheinz Schaber, and Thomas Wetzel, editors, *VDI-Wärmeatlas*, Springer Reference Technik, pages 239–257. Springer Berlin Heidelberg, Berlin, Heidelberg, 2019. ISBN 978-3-662-52988-1. doi: 10.1007/978-3-662-52989-8_14.
- [48] Joseph H. Spurk and Nuri Aksel. *Fluid Mechanics*. Springer, Cham, Switzerland, third edition edition, 2020. ISBN 978-3-030-30259-7.
- [49] Fritz Steimle. *Handbuch der Kältetechnik*. Springer, Berlin, softcover reprint of the hardcover 1st edition 1988 edition, 1988. ISBN 9783642825231.
- [50] Peter Stephan. B2 Grundlagen der Berechnungsmethoden für Wärmeleitung, konvektiven Wärmeübergang und Wärmestrahlung. In Peter Stephan, Stephan Kabelac, Matthias Kind, Dieter Mewes, Karlheinz Schaber, and Thomas Wetzel, editors, *VDI-Wärmeatlas*, Springer Reference Technik, pages 23–36. Springer Berlin Heidelberg, Berlin, Heidelberg, 2019. ISBN 978-3-662-52988-1. doi: 10.1007/978-3-662-52989-8_4.
- [51] Peter Stephan, Karlheinz Schaber, Karl Stephan, and Franz Mayinger. *Thermodynamik: Grundlagen und technische Anwendungen; Band 1: Einstoffsysteme*. SpringerLink Bücher. Springer, Berlin and Heidelberg, [online-ausg. der] 18. [gedr.] aufl. edition, 2008. ISBN 9783540928959. doi: 10.1007/978-3-540-92895-9.
- [52] Peter Stephan, Stephan Kabelac, Matthias Kind, Dieter Mewes, Karlheinz Schaber, and Thomas Wetzel, editors. *VDI-Wärmeatlas: Fachlicher Träger VDI-Gesellschaft Verfahrenstechnik und Chemieingenieurwesen*. Springer Reference Technik. Springer Berlin Heidelberg, Berlin, Heidelberg, 2019. ISBN 978-3-662-52988-1. doi: 10.1007/978-3-662-52989-8.
- [53] Peter Stephan, Stephan Kabelac, Matthias Kind, Dieter Mewes, Karlheinz Schaber, and Thomas Wetzel, editors. *VDI-Wärmeatlas: Fachlicher Träger VDI-Gesellschaft Verfahrenstechnik und Chemieingenieurwesen*. Springer Reference Technik VDI Springer Reference. Springer Vieweg, Berlin, 12. auflage edition, 2019. ISBN 9783662529898.
- [54] Ingrid Stober and Kurt Bucher. *Geothermie*. Lehrbuch. Springer Spektrum, Berlin and Heidelberg, 2., [überarb. und aktualisierte] aufl. edition, 2014. ISBN 3642417620. doi: 10.1007/978-3-642-41763-4.

- [55] A. Stodola. *Dampf- und Gasturbinen*. Springer Berlin Heidelberg, Berlin, Heidelberg, 1924. ISBN 978-3-642-50544-7. doi: 10.1007/978-3-642-50854-7.
- [56] Karl Strauß. *Kraftwerkstechnik: Zur Nutzung fossiler, nuklearer und regenerativer Energiequellen*. VDI. Springer, Berlin and Heidelberg, 6., aktualisierte aufl. edition, 2013. ISBN 978-3-642-01431-4.
- [57] Dawid Taler and Jan Taler. Simple heat transfer correlations for turbulent tube flow. *E3S Web of Conferences*, 13:02008, 2017. doi: 10.1051/e3sconf/20171302008.
- [58] André Thess and Robert Kaiser. F1 Wärmeübertragung bei freier Konvektion: Grundlagen. In Peter Stephan, Stephan Kabelac, Matthias Kind, Dieter Mewes, Karlheinz Schaber, and Thomas Wetzel, editors, *VDI-Wärmeatlas*, Springer Reference Technik, pages 759–762. Springer Berlin Heidelberg, Berlin, Heidelberg, 2019. ISBN 978-3-662-52988-1. doi: 10.1007/978-3-662-52989-8_37.
- [59] TLK-Thermo GmbH. TIL User Manual: Version TIL 3.12.1, as of 03.2023.
- [60] Walter Traupel. *Thermische Turbomaschinen: Geänderte Betriebsbedingungen, Regelung, Mechanische Probleme, Temperaturprobleme*. Springer Berlin Heidelberg, Berlin, Heidelberg, 2001. ISBN 978-3-642-62103-1. doi: 10.1007/978-3-642-17465-0.
- [61] Walter Traupel. *Thermische Turbomaschinen: Thermodynamisch-strömungstechnische Berechnung*. Springer Berlin Heidelberg, Berlin, Heidelberg, 2001. ISBN 978-3-642-62102-4. doi: 10.1007/978-3-642-17469-8.
- [62] Fredy Vélez, José J. Segovia, M. Carmen Martín, Gregorio Antolín, Farid Chejne, and Ana Quijano. A technical, economical and market review of organic Rankine cycles for the conversion of low-grade heat for power generation. *Renewable and Sustainable Energy Reviews*, 16(6):4175–4189, 2012. ISSN 13640321. doi: 10.1016/j.rser.2012.03.022.
- [63] Christian Vetter. Thermodynamische Auslegung und transiente Simulation eines überkritischen Organic Rankine Cycles für einen leistungsoptimierten Betrieb: Zugl.: Karlsruhe, KIT, Diss., 2014. URL <http://nbn-resolving.de/urn:nbn:de:0072-414504>.

Appendix

A. Additional Information for the Condenser Model

PARAMETER	VALUE	UNIT
Tube inner diameter	11	mm
Tube wall thickness	0.5	mm
Parallel hydraulic flows	4 · 69	-
Finned tube length	5	m
Number serial tubes	4	-
Serial tube distance	32	mm
Number parallel tubes	4 · 69	-
Parallel tube distance	27.71	mm
Fin thickness	0.15	mm
Fin pitch	2.5	mm

Table A.1.: Geometry parameters of the heat exchanger as implemented in the Condenser model. The condenser model contains all four heat exchangers used in MoNiKa.

B. Matlab Codes

B.1. Matlab Function for the Quantification of the Agreement of Results

In this subsection the Matlab Function *CalcDeviations.m* for the quantification of the agreement of results is presented.

```
function res = CalcDeviations(vector1, time1, vector2, time2,
    startTime, endTime)
% calculates deviations between 2 data sets. Vector 1 should
    always be Measurement
% Data and Vector 2 the simulation results.

% define number of time steps of new time vector
dt = 1; % time step size
```

```

n = (endTime-startTime)/dt;

% define new universal time vector
t = linspace(startTime, endTime, n)';

% remove non-unique values from time vector
[time1 unique_indeces] = unique(time1);
vector1 = vector1(unique_indeces);
[time2 unique_indeces] = unique(time2);
vector2 = vector2(unique_indeces);

% interpolate Results on new time Vector
interV1 = interp1(time1, vector1, t);
interV2 = interp1(time2, vector2, t);

% initialize result vectors
e_abs = zeros(size(t)); e_rel = e_abs;

% calculate absolute and relative Deviations for each time
step
for i = 1:length(t)
e_abs(i) = interV2(i)-interV1(i);
e_rel(i) = e_abs(i)/interV1(i);
end

% calculate mean and maximal values of the absolute value
function of the deviation
e_abs_mean = mean(abs(e_abs));
[e_abs_max, index] = max(abs(e_abs));
t_e_abs_max = t(index);

e_rel_mean = mean(abs(e_rel));
[e_rel_max, index] = max(abs(e_rel));
t_e_rel_max = t(index);

% write everything in one structure array and return the
result
res.t = t;

res.e_abs = e_abs;
res.e_abs_mean = e_abs_mean;
res.e_abs_max = e_abs_max;
res.t_e_abs_max = t_e_abs_max;

res.e_rel = e_rel;
res.e_rel_mean = e_rel_mean;
res.e_rel_max = e_rel_max;
res.t_e_rel_max = t_e_rel_max;

```

B.2. Matlab Codes for Filtering and Resampling of Measurement Data

In this subsection the Matlab code *dataPreparationDay0.m* for the data preparation (filtering and resampling) for the input data of Day0 is presented. The codes and procedure for Day1-3 are equal but differ in the filter parameters and intervals chosen.

```
% filters and resambles Condenser input data for day 0: mass-
    flow, inlet enthalpy, outlet Pressure, ambient temperature,
    ambient pressure, humidity

clear all
close all

% set Latex as default interpreter language
set(groot, 'defaultAxesTickLabelInterpreter', 'latex');
set(groot, 'defaultLegendInterpreter', 'latex');
set(groot, 'defaultTextInterpreter', 'latex');

%% load data
load('C:\Users\local\Documents\1 Masterarbeit\16 Measurement
    Data\v11_Day1EfficiencyJoaquinAdded.mat', 'day0')

% load calculated Enthalpies
load('C:\Users\local\Documents\1 Masterarbeit\18 Matlab\
    Stoffdatenberechnung Kondensator\
    Enthalpies_2ndTransitionSmoothened.mat')

% store data in new variable with SI-unit
T_amb = day0.ambient.T_amb+273.15;
t = day0.time.t;
m = day0.m.FI10_01;
p_out = day0.p.PS10_05_bar*100000;
p_amb = day0.ambient.p_amb*100000;
hum = day0.ambient.rel_humid_amb;

%% apply filter

n_order = 2;           % filter order
fs = length(t)/ t(end); % sampling frequency

% cutoff frequencies [Hz]
fc_Tamb = 0.001;
fc_m = 0.005;
fc_h = 0.003;
fc_p_out = 0.001;
fc_p_amb = 0.001;
fc_hum = 0.0005;

% ambient Temperature
[b,a] = butter(n_order,fc_Tamb/(fs/2)); % create filter
    coefficients
T_amb_filtered = filtfilt(b,a,T_amb); % apply filter
```

```

% mass flow
[b,a] = butter(n_order,fc_m/(fs/2)); % create filter
coefficients
m_filtered = filtfilt(b,a,m); % apply filter

% inlet Enthalpy
[b,a] = butter(n_order,fc_h/(fs/2)); % create filter
coefficients
h_in_filtered = filtfilt(b,a,h_in); % apply filter

% outlet pressure
[b,a] = butter(n_order,fc_p_out/(fs/2)); % create filter
coefficients
p_out_filtered = filtfilt(b,a,p_out); % apply filter

% ambient pressure
[b,a] = butter(n_order,fc_p_amb/(fs/2)); % create filter
coefficients
p_amb_filtered = filtfilt(b,a,p_amb); % apply filter

% humidity
[b,a] = butter(n_order,fc_hum/(fs/2)); % create filter
coefficients
hum_filtered = filtfilt(b,a,hum); % apply filter
%% Resampling

% define number of total time steps
steps = 200;

% define intervals
interval_breaks = [2500 5000, 29400, 32000, 50700, 54560,
    58000, 69850];

% define interval refinement
interval_Refinement = [1 2 1 20 1 0.5 20 1 1 1];

% create new time vector
t_resampled = createResampledTimeVector(t,steps,
    interval_breaks, interval_Refinement);

% resample data to new time vector by linear interpolation of
    filtered data
T_amb_resampled = interp1(t,T_amb_filtered,t_resampled);
m_resampled = interp1(t,m_filtered,t_resampled);
h_in_resampled = interp1(t,h_in_filtered,t_resampled);
p_out_resampled = interp1(t,p_out_filtered,t_resampled);
p_amb_resampled = interp1(t,p_amb_filtered,t_resampled);
hum_resampled = interp1(t,hum_filtered,t_resampled);

%% plots to check weather filtered and resampled curves have
    good agreement with original data

```

```

figure
plot(t,T_amb)
hold on
plot(t,T_amb_filtered,'Color',[1 0 0],'LineWidth',1)
plot(t_resampled,T_amb_resampled,'--')
arrayfun(@xline,interval_breaks); % plot vertical lines for
    intervals

figure
plot(t,m)
hold on
plot(t,m_filtered,'Color',[1 0 0],'LineWidth',1)
plot(t_resampled,m_resampled,'--','LineWidth',1)
arrayfun(@xline,interval_breaks); % plot vertical lines for
    intervals

exampleInletEnthalpy = figure;
plot(t,h_in/1000)
hold on
plot(t,h_in_filtered/1000,'Color',[1 0 0],'LineWidth',1)
plot(t_resampled,h_in_resampled/1000,'.','Color',[64, 184,
    66]/256,'LineWidth',1)
arrayfun(@xline,interval_breaks); % plot vertical lines for
    intervals
grid on
legend('Original Data', 'Filtered Data', 'Resampled Data')
set(legend, 'NumColumns', 3)
legend('Location', 'southoutside')
xlabel('Time [s]')
ylabel('Enthalpy [ $\frac{\text{kJ}}{\text{kg}}$ ]')
title('Evolution of Condenser Inlet Enthalpy over Time for
    Day0')
% add text for points
db = 1200;
h = 2.2e5/1000+20;
text(interval_breaks(1)/2-db,h, '\textcircled{1}')
text(mean([interval_breaks(2),interval_breaks(1)]-db),h, '\
    textcircled{2}')
text(mean([interval_breaks(3),interval_breaks(2)]-db),h, '\
    textcircled{3}')
text(mean([interval_breaks(4),interval_breaks(3)]-db),h, '\
    textcircled{4}')
text(mean([interval_breaks(5),interval_breaks(4)]-db),h, '\
    textcircled{5}')
text(mean([interval_breaks(6),interval_breaks(5)]-db),h, '\
    textcircled{6}')
text(mean([interval_breaks(7),interval_breaks(6)]-db),h, '\
    textcircled{7}')
text(mean([interval_breaks(8),interval_breaks(7)]-db),h, '\
    textcircled{8}')

```

```

text(mean([interval_breaks(8),t(end)]-db+800),h, '\textcircled
{9} ')

set(exampleInletEnthalpy, 'Position', [500 300 550 260])

figure;
plot(t,p_out)
hold on
plot(t,p_out_filtered, 'Color', [1 0 0], 'LineWidth', 1)
plot(t_resampled, p_out_resampled, '--', 'LineWidth', 1)
arrayfun(@xline, interval_breaks); % plot vertical lines for
intervals

exampleAmbPressure=figure;
plot(t,p_amb)
hold on
plot(t,p_amb_filtered, 'Color', [1 0 0], 'LineWidth', 1)
% plot(t_resampled, p_amb_resampled, '--', 'LineWidth', 1)
% arrayfun(@xline, interval_breaks); % plot vertical lines for
intervals
grid on
legend('Original Data', 'Filtered Data')
xlabel('Time [s]')
ylabel('Pressure [Pa]')
title('Evolution of Ambient Pressure over Time for Day0')

set(exampleAmbPressure, 'Position', [500 300 550 200])

figure
plot(t,hum)
hold on
plot(t,hum_filtered, 'Color', [1 0 0], 'LineWidth', 1)
plot(t_resampled, hum_resampled, '--', 'LineWidth', 1)
arrayfun(@xline, interval_breaks); % plot vertical lines for
intervals

%% Prepare Dymola Export: combine everything in one array

export = [t_resampled; m_resampled; h_in_resampled;
p_out_resampled; T_amb_resampled; p_amb_resampled;
hum_resampled]';

%% safe example plots for written version of thesis
% exportgraphics(exampleAmbPressure, 'Example_filter.pdf', '
Resolution', 300)
% exportgraphics(exampleInletEnthalpy, 'Example_resampled.pdf
', 'Resolution', 300)

```

```

function t_resampled = createResampledTimeVector(t,steps,
    interval_breaks, interval_Refinement)
% creates a new time vector with the same start and end time
    and a given
% number of intervals

% t = old time step
% steps = number of total steps for new time vector
% interval_breaks = time at which intervals begin; eg. [1000,
    1500, 2300]
% -> in this case there would be 4 intervals and therefore 3
    interval breaks
% interval_Refinement = density of timesteps for each interval
    ; e.g. [1 2 3
% 1] --> in this case there are 4 intervals where in the
    second interval
% the density of steps is twice as high as in the first
    interval, ...

% extract number of intervals and time at which each interval
    starts and ends
n_Interval = length(interval_breaks) + 1;
interval_Times(1) = t(1);
interval_Times(2:1+length(interval_breaks)) = interval_breaks;
interval_Times(end+1) = t(end);

% calculate total area of weight-time function
for i = 1:n_Interval
dt(i) = interval_Times(i+1)-interval_Times(i);
area(i) = interval_Refinement(i)*dt(i);
end
total_area = sum(area);

% calculate how many steps are in each interval
for i = 1:n_Interval
n(i) = round(area(i)/total_area * steps);
end

% if there are more or less total time steps than specified (
    due to rounding in the number for each interval) -> take or
    give
% the difference to the interval with the most steps
dn=sum(n)-steps-length(interval_breaks);
[Max,Index] = max(n);
n(Index) = Max-dn;

% create new time vector
for i = 1:n_Interval
t_linspace{i} = linspace(interval_Times(i),interval_Times(i+1)

```

```

        ,n(i));
end

t_resampled = t_linspace{1};
for i = 2:n_Interval
t_resampled = [t_resampled(1:end-1), t_linspace{i}];
end

```

B.3. Matlab Function for Filtering of Turbine Shaft Power

```

function filteredData = filterData(unfilteredData,timeVector,
    cutoffFrequency)
% filters given data and returns it

n_order = 2;           % filter order
fs = length(timeVector)/ timeVector(end); % sampling frequency

% Filter
[b,a] = butter(n_order,cutoffFrequency/(fs/2)); % create
    filter coefficients
filteredData = filtfilt(b,a,unfilteredData); % apply filter

% make plot to show effect and check if filter parameter is
    adequate
figure
plot(timeVector,unfilteredData,'r')
hold on
plot(timeVector,filteredData,'--b','LineWidth',1.5)
grid on
title('filtered and unfiltered Data')

```